CHALMERS
UNIVERSITY OF TECHNOLOGY

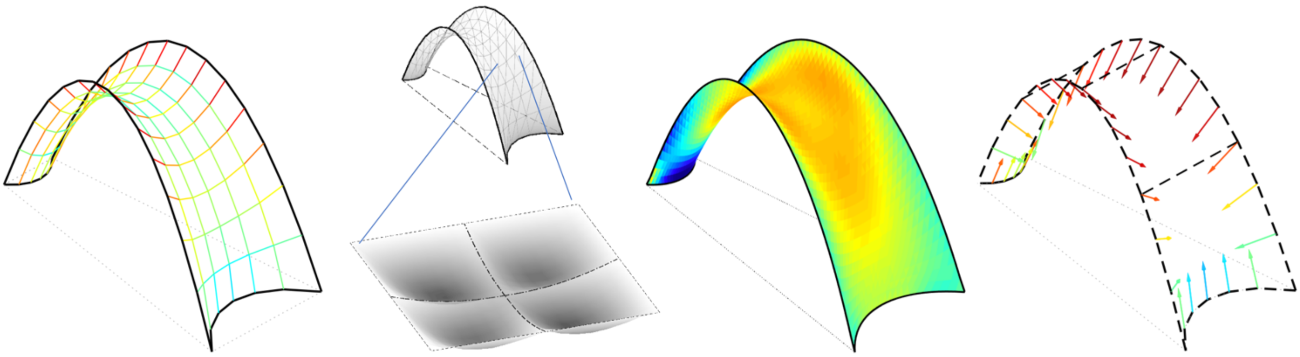

Flexible formwork for concrete shells

Development of a computational framework for design, optimization and construction of prestressed cable and membrane structures

Master's thesis in Structural Engineering and Building Technology

JOHAN ÖRNBORG

Department of Architecture and Civil Engineering
CHALMERS UNIVERSITY OF TECHNOLOGY
Gothenburg, Sweden 2019

REPORT NO. ACEX30-19-68

Flexible formwork for concrete shells

Development of a computational framework for design, optimization and construction of prestressed cable and membrane structures

JOHAN ÖRNBORG

Department of Architecture and Civil Engineering
Research Group for Architecture and Engineering
CHALMERS UNIVERSITY OF TECHNOLOGY
Gothenburg, Sweden 2019

Flexible formwork for concrete shells
Development of a computational framework for design, optimization and construction of prestressed cable and membrane structures
JOHAN ÖRNBORG

Technical report no ACEX30-19-68
Department of Architecture and Civil Engineering
Chalmers University of Technology
SE-412 96 Göteborg
Sweden
Telephone + 46 (0)31-772 1000

Cover:
Illustrations of the main subjects of the concept, created as part of the case study in chapter 4.

[Chalmers Reproservice]
Gothenburg, Sweden 2019

Flexible formwork for concrete shells
Development of a computational framework for design, optimization and construction of prestressed cable and membrane structures
JOHAN ÖRNBORG
Department of Architecture and Civil Engineering
Chalmers University of Technology

Abstract

One of the complications with shell construction in any material today is the complexity of the building process, especially to construct and build the formwork and/or guide work. This often leads to unsatisfactory building time followed by increased cost. In a quest to rationalize this process, a concept based on flexible formwork has been explored for construction of freeform concrete structures.

A computational framework has been developed, with functions for form finding and analysis of cables, membranes and shells. The theoretical predictions has been evaluated in a case study, with the construction of a full scale concrete pavilion. The predictions were found to be reliable and accurate with a mean deviation in formwork geometry of just 0.5 %. There were also indications that the cost of formwork for concrete shells can be reduced with as much as 32% - 66% through the use of a flexible formwork concept, compared to a traditional timber formwork.

Keywords: flexible formwork, fabric formwork, form finding, architectural geometry, FEM, cables, membranes, shells, computational framework, DKT

Preface

The work in this master's thesis has grown out of love for spectacular architecture, but also out of love for rational buildings where well formulated architectural programs can result in efficient construction and use from economic and environmental perspectives. With the rapid development of computational power and automated manufacturing techniques, alternative building methods should be explored in order to guarantee the most economic and materially efficient execution. Many examples can be pointed out ([1], [2] & [3]) where spectacular architecture and new thinking is both as rational as it is esthetically pleasing. My hope is that the conclusions in this thesis may further strengthen this belief and encourage further exploration of diverse architectural and structural visions with, to quote Bjarke Ingels [4], the motto 'Yes is more'.

Acknowledgements

I would like to extend my sincere gratitude to Dr. Mats Ander who through his endless enthusiasm and vast knowledge has guided me through this thesis work. Your contribution extends far beyond my expectation, and your personal dedication and interest made the study a success. I would like to further acknowledge the contribution from my opponents Gabriel Borg and Albin Johnsson, who through blood, sweat and tears helped out passionately with the case study, contributing with ideas that I am grateful for. During the thesis work, I also got the chance to visit Block Research Group at ETH Zürich who has given me great inspiration and motivation to conduct this study. Special thanks goes to Dr. Tom Van Mele, Dr. Tomás Méndez Echenagucia and Dr. Mariana Popescu who provided me with their valuable knowledge and experience in the construction of flexible formwork. I would also like to thank Erica Hörteborn at ACE Research Group, Chalmers, who helped out with the case study in person through tailoring skills and knowledge about membranes. In addition, Adj. Professor Ingemar Löfgren, Head of R&D at Thomas Concrete Group, was kind enough to provide us with valuable knowledge and sponsoring of fiber reinforced concrete for the case study. Last but not least, I would like to thank Niklas Johansson at Ramboll for his early feedback and Annika Adler Örnborg for her help with illustrations.

Thank you all, any mistakes or misunderstandings are completely my own,

Johan Örnborg, June 2019

Contents

1 Introduction

By geometrically optimizing concrete structures, it is possible to reduce the amount of material with as much as 40% to achieve equivalent strength of a standard prismatic section. Considering that concrete as a building material stands for a whopping 3% (2008) of total CO_2 emissions alone (reported to have grown to 5.2 % in 2014 [5]), there is incitement to investigate how such an impact can be reduced [6]. Naturally, this will also have positive implications on building cost.

1.1 Background

One of the complications with shell construction in any material today is the complexity of the building process, especially to construct and build the formwork or guide work. This often leads to unsatisfactory building time and increased cost [7]. Unfortunately, this tend to outweigh the benefits in material saving and structural efficiency that a shell can provide. With a lightweight and re-usable formwork based on cables and/or membranes, there is great potential to rationalize the building process of concrete shells and to make it a more attractive alternative to the more traditional building alternatives. It is also relevant from an environmental perspective to be able to reuse the formwork in other construction. With a rationalized building process, the use of shells could become a more competitive alternative to standard building methods and structural systems.

Figure 1. *Concrete shell constructed with a flexible formwork concept by Block Research Group. The shell in the picture ([8]* © M. Lyrenmann, 2017) *was used as verification for upcoming NEST/Hilo project in 2019 [9].*

Shell structures has previously had an up rise in the mid 20th century, mainly due to cheap labor at the time [10]. How can the interest for these structures be revived? With growing importance of environmental and life cycle aspects with more efficient material use, the timing might be right for the return of these intriguing forms and architectural masterpieces.

Figure 2. *Left: Flexible formwork by Block Research Group, ETH Zurich. Right: Close-up on cable-net node connection. Pictures from [9]* © N. Iljazovic, 2017.

1.2 Aim

The concept of flexible formwork for reinforced concrete shells will be explored. Main focus is to develop a computational framework for analysis and form finding of combined cable-net and membrane structures. The framework should also contain functions for analysis of doubly curved shells with the Finite Element Method (FEM), such that results can be used in an iterative process to optimize and refine all stages of the design process with full control of the outcome.

The work is intended to be a platform for further development and functionality in the design of flexible formwork, but also cable-, membrane- and shell structures in general.

1.2.1 Research questions

1) Can the use of prestressed flexible formwork provide a rational building process compared to current standard methods?
2) How well can the final geometry and forces in the formwork and shell be predicted with help of the developed computational functions? How large deviations can be accepted?
3) How does the formwork influence the cost of concrete shell construction?
4) Is the formwork beneficial from an environmental perspective?
5) What are the limitations with this type of formwork method?

1.2.2 Relevance within the field of research

This thesis investigates methods for analysis and form finding of cables, membranes, shells and perimeter systems for flexible formwork, which as a subject is not yet well covered within the science community. The developed functions will handle all those aspects within the same computational framework.

Flexible formwork has shown great potential in earlier studies but has yet to reach true commercial interest. More work on the subject could expand the knowledge and understanding of such structures in order to justify its place on the market.

1.3 Method

The thesis work is divided into the following stages:

- Literature study
- Development of a computational framework
- Empirical pre-studies of the concept
- Case study and verification
- Evaluation and conclusion

Different stages of the thesis work is discussed briefly in the bullet points below:

1. Literature study; form-finding techniques and shell analysis are investigated, as well as a study and economic comparison between traditional formwork/falsework and a cable-net supported one, where the majority of the formwork can be reused.

2. Computational framework; A set of computational functions is developed as basis for the form-finding and analysis of the flexible formwork. A shell analysis tool, using FEM and Kirchhoff shell theory, is programmed within the same context. The code is written in MATLAB due to the initial focus on mathematical formulations and algorithms rather than User Interface (UI). The main reason for the development of a computational framework from scratch is to be able to analyze all parts of the design process within the same software, with minimum limitations, and where the iteration process between form-finding and shell analysis can be optimized and used to inform the design on all levels and stages. A version in Python might be written in a later stage, to open up for use and collaboration with other open source frameworks.

3. Empirical studies are performed to explore different practical aspects of a flexible formwork. This will give valuable knowledge prior to the case study setup. Main subjects concern choice of fabric, cable network setup and working with concrete in high slopes.

4. Case study; the verified computational framework is applied in a case study, with the design and construction of a concrete shell pavilion in full scale, using the formwork concept. The prototype is used to evaluate the accuracy of results (deflections, stresses) from analysis.

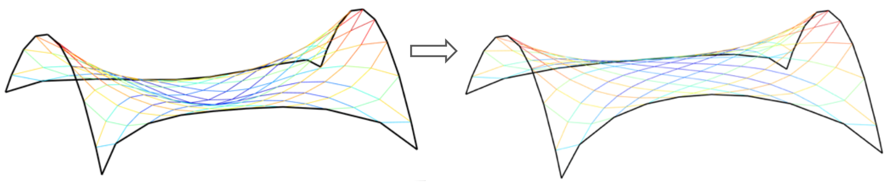

Figure 3. *Example of optimization process with Force Density Method programmed in MATLAB. From left to right, element lengths are adjusted to better carry the imposed concrete load. As a result, the thickness of concrete can be reduced, which in turn, reduces the load.*

1.4 Limitations

Environmental impact is evaluated from a material use/waste perspective with some predictions on impact from reuse of formwork. Full investigation of carbon footprint in a life cycle perspective will remain outside the scoop of this early stage exploration of the concept.

Comparison of cost in relation to traditional formwork is based on available literature on traditional methods which are compared to empirical results and documentation of material cost and labor of the studied concept. A complete statistical validation is thus not possible within the given time frame and budget, as it requires repeated experiments with conclusive outcome. Further studies will need to be conducted to verify results.

Material properties are only briefly discussed. The thesis aim presents no intention to investigate, evaluate or compare performance of different types of reinforcement or concrete itself. However, such unintentional observations and learnings are reported.

User interface (UI) is not prioritized in development. Primary focus is on creating robust and efficient solvers written such that a UI extension can be developed at a later stage.

However, the functions should produce good visual feedback on results in complement to the numbers.

Only central functions of the computational framework (form finding and FE analysis functions) are presented and supported by relevant background theory. Support functions for generating mesh, topology and visual feedback are not elaborated as these are vast subjects of their own, unfortunately outside the time frame for this thesis.

1.5 Thesis structure

In order to describe and verify all subjects that one will come across when discussing a flexible formwork, the report structure deviates somewhat from a traditional structure. Theory is presented continuously, with verifications and conclusions for each subject. The overall concept will also be evaluated from a holistic perspective, with more general conclusions. To guide the reader further, there is clear subdivision in chapters where the first is an overview and introduction of the flexible formwork concept. This is followed by a chapter about the computational framework that is needed to analyze such a concept, including functions that covers analysis of concrete shells. With those two cornerstones, a case study has been made in order to evaluate both the computational framework, but first and foremost the concept itself. Results and conclusions from all previous chapters will then be summed up in general views on performance of the concept as a whole, being the final chapter of the report.

Naturally, there are key terms and necessary background knowledge that are common to all the subjects. Such ideas and terminology will be presented in the overview of the concept or with references to more information in Appendix.

2 Concept overview

This section serves as an introduction to the formwork concept. The main parts of a flexible formwork are identified. Core definitions in the field of architectural geometry is established by introducing terminology from differential geometry, shell theory, and form finding that is used frequently in this thesis. The historical context and economic implications are briefly discussed.

2.1 The shell in a nutshell

A common definition of shells is something that is very thin in relation to its other expansive directions [11]. A shell is also commonly mentioned as a surface structure (although this is a wider term also including pure tensile structures), referring to the same geometrical properties. In order for a thin object to have any structural integrity in compression, the surface needs to be curved [10]. With a properly selected curvature (in one or several directions), shell structures retrieves significant (transversal) load bearing capacity in relation to the used amount of material. Such structures often look gravity defying and is by some considered to be the holy grail of structures and an amusement in architecture. Not unexpectedly, this comes at a cost since analysis of such structures are usually complex. The next few sections will briefly discuss some of the key aspects as this is fundamental knowledge in the discussion of a flexible formwork. The reader is referred to books like [10], [11] or [12] for more detailed information on the subject.

2.1.1 Curvature

Gaussian curvature can be used to describe the properties of a doubly curved surface. Typically, one can arrange such surfaces in three different categories where the surface has positive, negative or zero Gaussian curvature [10]. The mathematical formulation is

$$\kappa = \frac{1}{R_1}\frac{1}{R_2} \tag{1}$$

where κ denotes the Gaussian curvature and $1/R_1$ and $1/R_2$ the principal curvatures respectively. This thesis will focus on surfaces with negative curvature (anticlastic) as exemplified in **Figure 5** since this type of geometry is suitable for prestressing which is often needed in a flexible formwork.

Figure 4 - **Figure 6** exemplifies the three different categories of curvature and are intended to serve as a crash course introduction to shells and what is a more or less suitable shape in the context of flexible formwork.

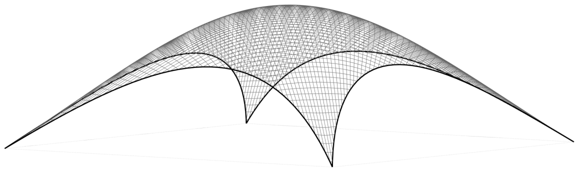

Figure 4. *Synclastic surface, illustrating positive Gaussian curvature.*

Figure 5. *Anticlastic surface, negative Gaussian curvature. This type of surface is suitable in the application of a prestressed cable-based formwork since all nodes are resistant against loading from any arbitrary direction [10].*

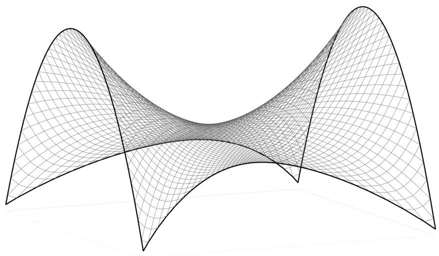

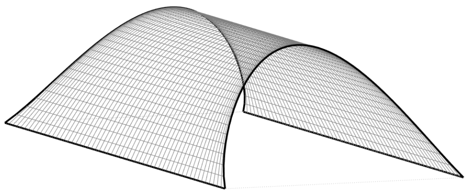

Figure 6. *Barrel vault with zero Gaussian curvature; the curvature is zero along one of the principal directions.*

2.1.2 Form finding

The concept of form finding, also known as shape finding, is to search for a structural geometry and topology that remains in equilibrium with respect to one or several constraints. A suitable form can be found through mathematical methods, physical methods or graphical methods. The basic idea is often to let forces shape the structure in order to not only rely on material stiffness, but to derive suitable geometry for the applied loading. Structures with the same qualities are often found in nature, such as sea shells [11].

2.1.3 Concrete shells in history

Concrete shells became frequently built from the end of World War I and a few decades forward, with a prime time between 1920-1960 when tens of thousands of various sizes supposedly has been built [7]. Frequently mentioned pioneers in the design of such structures are Félix Candela and Heinz Isler with slightly different approaches to the subject. Candela designed mostly ruled surfaces, with the benefit of being able to produce the formwork with only straight laths (**Figure 7**). Hyperbolic paraboloids have this quality and can be formulated with simple mathematical equations, thus easily deriving geometry for construction. Recognizing that Félix Candela did his work without any help from computer analysis, this seems to be a rather sober approach.

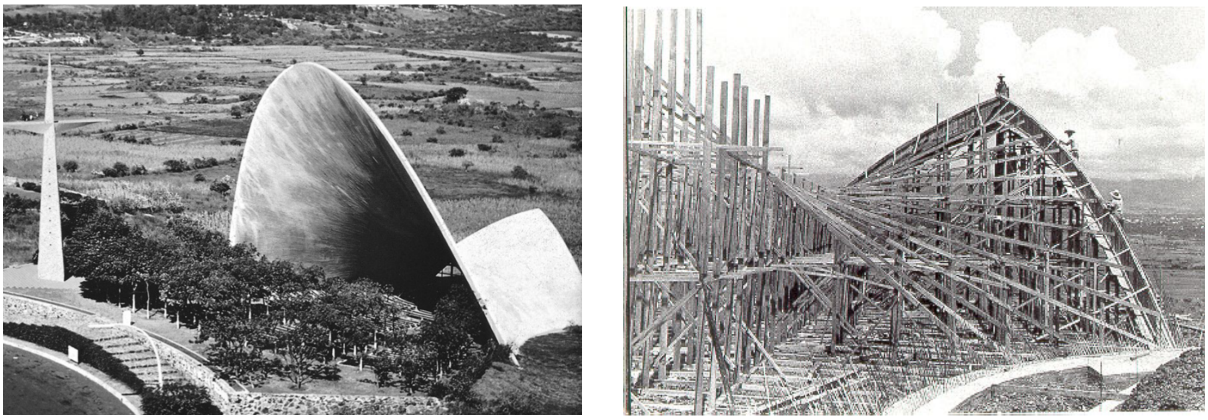

Figure 7. *Left: Picture of chapel Lomas de Cuernavaca, Morelos, Mexico, by Felix Candela. [13] Right: Formwork for the same shell [14].*

Heinz Isler on the other hand, designed shells relying on physical form finding and he is known for his hanging cloth models that give an inverted optimized form in compression, with examples of shell and form finding in **Figure 8.** This method provides endless alternatives to mathematical shapes, but with a practical challenge in discretization and scaling up geometry.

Figure 8. *Left: Concrete shell designed by Heinz Isler* [15]. *Right: Physical form finding by hanging fabrics* [16].

Since the 1960s and forward, there has been a demise of shell construction and such structures are rarely produced today. Although there is a fascination of shells among engineers and architects, it has yet to regain commercial interest and appreciation. Multiple reasons for this decline has been suggested or identified (quoted from [17]):

- Shapes has fallen out of fashion
- Shells does not comply well with building physics demands
- Shells are difficult to generate and analyze
- Shells are expensive

2.1.4 Economic aspects of shell construction

Shell structures are complex structures in need of complex analysis which will implicate the production process. When following up different studies, the formwork is a common denominator in what is holding a significant part of the cost of shell construction [7].

The construction of traditional formwork (scaffolding and temporary timberwork) is labor intensive. It is estimated to constitute 30-60% of total cost, and also produces a substantial amount of material waste [18]. As the prices of labor versus material cost has shifted over the course of the last century, this is mentioned as a factor in the decline of shell construction in recent time. Labor cost has a reported increase by 8-11 times on the US market between 1958-2002 [17].

2.2 The use of flexible formwork

The idea of using a textile or any other flexible material as formwork in the construction process is nothing new. Already in Roman times, there is documentation of Vitruvius using a flexible mould methodology to stack layers of clay vertically in the construction of a retaining wall [19]. Similar methods becomes more frequently reported during the 18th and 19th century, with applications within the field of civil engineering [6].

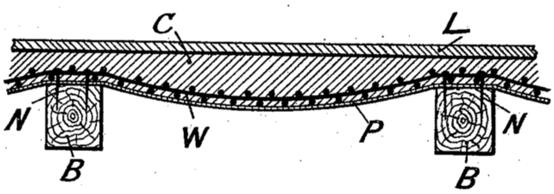

Figure 9. *Floor system proposed by Gustav Lilienthal. Figure borrowed from the filed patent in Feb. 21, 1899 [20].*

Gustav Lilienthal applied for a patent in 1899, concerning his invention of a floor system produced with flexible formwork. In all simplicity, a piece of fabric is spread out over parallel beams and used as mould for concrete (**Figure 9**). Quite interestingly, this method was reported to reduce concrete use by as much as 20% due to the sagging effect, which is effectively following the bending moment curve, with greater thicknesses in the middle of spans. A similar concept has been investigated more recently, with a patent in 1971 [19].

Another rather well known concept is the Ctesiphon system, invented by James Waller. A series of arches is erected parallel to each other. The arches are then covered with a sagging fabric, essentially forming a corrugated barrel roof shell. The depth of the corrugation is determined through the amount of prestressing/excess of material. Several buildings of this type were erected in the 1940s and forward. Today, there is still one standing in Nicosia, Cyprus. Waller patented his system in 1955 which consisted of fabrics suspended between truss arches, spanning up to 150 m [21]. Waller applied for several other patents, including a column cast in fabric formwork [5], which has later been further investigated and developed by Mark West [21].

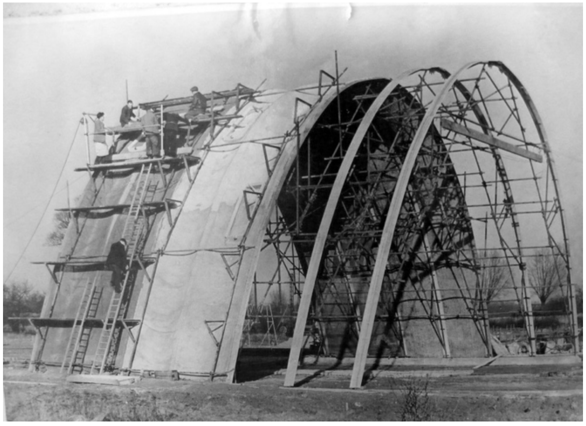

Figure 10. *Ctesiphon formwork system [21].*

Current research on the fabric formwork subject seems to only be increasing and in 2008, the first international conference on fabric formwork was held. Among the known contributions in modern time, many are made by the research team at the Centre for Architectural Structures and Technology (C.A.S.T), led by Mark West, who has also written a book on the subject in 2017 [21].

Block Research Group at ETH Zürich has an ongoing research project since 2011 called HiLo, which is a research and innovation unit for NEST. NEST is a research and demonstration platform were concepts can be studied under real conditions under extended periods of time. With HiLo, a concept based on cable supported fabric formwork will be used in the construction (planned construction start in summer, 2019) of an isolated shell with a built in radiation unit (**Figure 11**), it will also have photovoltaic cells on the roof surface [22]. In summary, this building system is intended to be a zero emission concept during operation and represents an extension of the concept that is studied in this thesis.

Figure 11. *Insulated concrete shell, constructed with a flexible formwork.*

To the left in **Figure 11**, different layers of the cross section are shown. To the right, the finished concrete (inside) surface is visible. The steel connectors are left from the construction process which was temporarily attached to the cable net nodes. The cast-in steel rods act as shear connectors between the structural layers [23].

2.3 Design flowchart and considerations

Necessary parts in analysis of a flexible formwork concept are identified (see **Figure 12**). Depending on which parameters are most important for the desired design, these subjects may be connected in different ways to optimize the formwork and permanent shell structure. Such considerations will be further discussed in chapter 3.

Cable analysis (section 3.2)
The network will have two form found equilibrium states. Prestressed state (for construction) and loaded state (concrete self-weight), which will give the final geometry.

Membrane analysis (section 3.3)
The two main parts of the membrane related analysis is to predict how much sagging will take place, and how to pattern and flatten the membrane to properly mount it with desired fit and possible prestressing.

Shell analysis (section 3.4)
FE analysis of the shell is made in design. The chosen shell geometry (i.e. thickness) affects the load in form finding of the cable net, but also amount of sagging of the membrane. Thin shells are often governed by buckling [24]. Therefore this is also an important part of analysis.

Perimeter system (section 3.5)
A temporary frame is used to prestress the cable net, to obtain global equilibrium. FE analysis is needed in design.

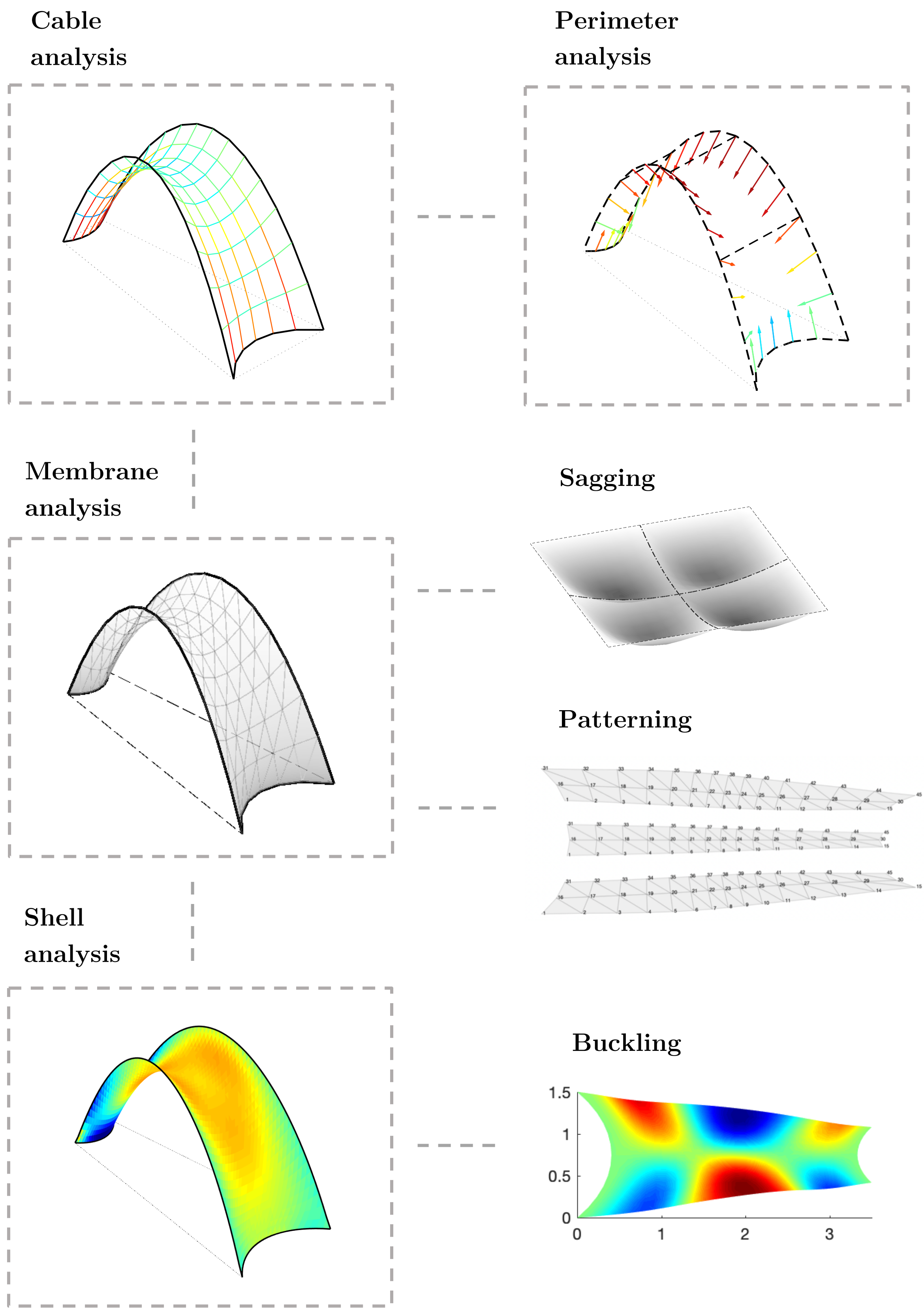

Figure 12. *Concept overview. Main components in design.*

3 Computational framework

A framework for analysis of flexible formworks has been developed. This chapter covers the theoretical basis that is fundamental to describe the behavior of tensile structures and shells that will govern the formwork design. Since this thesis cover a wide range of subjects to describe and develop a flexible formwork, the theory is presented in a development and design context which has been clearly divided into four main subjects. Benchmarking, empirical studies and analytical reference solutions are used as verification.

The subchapters in development of computational functions are:

1) Cable network analysis
2) Membrane analysis
3) Shell analysis
4) Perimeter system analysis

3.1 Framework overview

Functions are written on a general form (MATLAB) such that all developed functions (form finding and FE analysis) can be used independently or together to solve an arbitrary problem statement. During the course of development, several support functions has also been written which are not described or elaborated further in this text since their formulation felt somewhat restricted to the current problem statement. In **Figure 13**, an overview is presented of how functions were set up and connected for the case study (section 4.2).

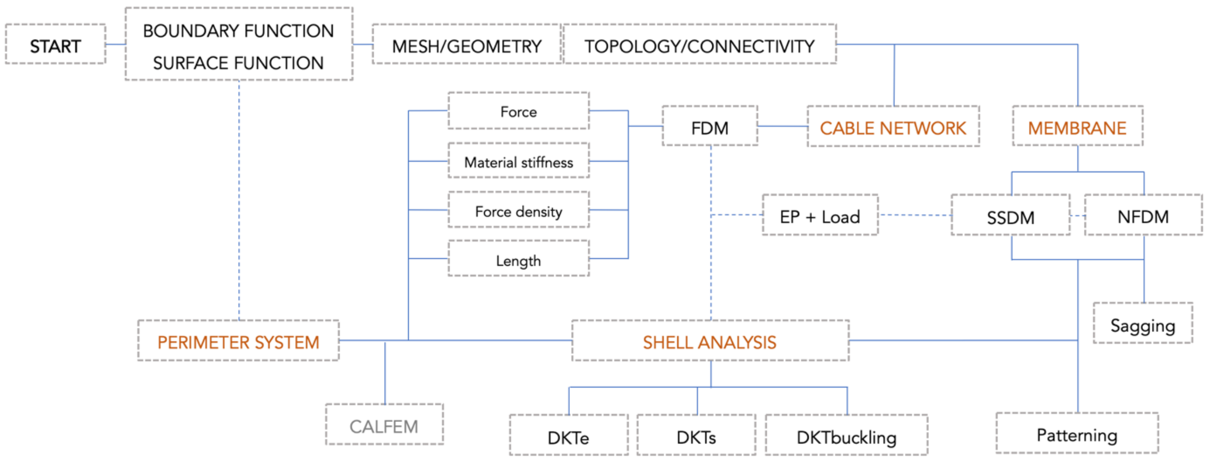

Figure 13. *Overview of how the developed functions were set up and connected to perform analysis in the case study, chapter 4.*

A summary and description of all main functions of the computational framework are listed below. Support functions such as mesh and topology generation, 3D-plot tools and other functions to handle and transfer data between base functions has been left out (see limitations in section 1.4).

Cable analysis

fdm3lin	linear form finding with the Force Density Method (FDM).
fdm3u	non-linear form finding (FDM) with respect to known unstrained element lengths and material properties, i.e. material stiffness.
fdm3f	non-linear form finding (FDM) with respect to target element forces.
fdm3l	non-linear form finding (FDM) with respect to target element lengths.

Membrane analysis

ssdm3	non-linear form finding with help of the Surface Stress Density Method (SSDM) for minimum surface area solutions.
nfdm3lin	linear form finding with Natural Force Density Method (NFDM) of membranes, equivalent to fdm3lin for cables.
nfdm3u	non-linear form finding (based on NFDM) of membranes with respect to known unstrained element side lengths and material properties, i.e. material stiffness.

Shell analysis

dkt3e	calculating element stiffness matrix and body forces for a shell element in 3D.
dkt3s	calculating shell element forces, including principal stresses and moments.
dkt3b	calculates the geometrical stiffness matrix for DKT elements to solve a linear buckling problem.

Perimeter system analysis

fdm3reactions	automatic force generator - reaction forces from the cable network analysis.
bar3e	calculating element stiffness matrix (existing function from CALFEM library [25]).
bar3s	calculating element forces (existing function from CALFEM library [25]).
beam3e	calculating element stiffness matrix (existing function from CALFEM library [25]).
beam3s	calculating element forces (existing function from CALFEM library [25]).

3.2 Cable network analysis

The main part of the flexible formwork consists of a prestressed cable network. This chapter describe the basic characteristics of a cable, how its behavior can be formulated in a mathematical model and how it can be discretized into elements and combined into a network. Material properties and practical aspects are briefly discussed.

A few design prerequisites has been assumed early in the design stage. The cable network is expected to fulfil several requirements in addition to structural efficiency. Buildability and versatility has to be considered with equal importance to be able to develop a cost effective and reusable formwork. To let all three main criteria influence the design from an early stage, a list of priorities will guide the development:

1) The mesh layout should be based on quadrilateral geometry.
2) Equality of element lengths should be considered in form finding, with target of 0.20 - 0.25 meters.
3) Angles in cable crossings should be in the range of $60 - 120°$ to limit demands on cable connections.
4) Cable orientation should be guided by principal curvature, but the buildability aspect is allowed to induce deviations.
5) Discretization should be sufficiently smooth to achieve efficient force paths and simple connections (allow for continuous load paths).

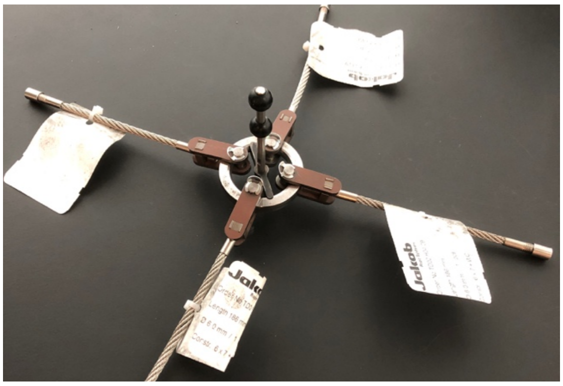

Figure 14. *Engineered cable net node connection developed by Block Research Group. The transversal pin is used to verify geometry with photogrammetry and is mounted downwards.*

An important aspect of the cable mesh is also that its layout should simplify the mounting of the membrane. A plane fabric that is placed on a doubly curved surface will need to be subject to a patterning and flattening procedure (section 3.3.5). Geodesics (for definition, see [26]) can be used as efficient guidelines for patterning, but in context of a flexible formwork concept, it is also rational to use existent cable lines for such a procedure, given that there is a reasonable correlation with the cables and geodesic lines [27].

3.2.1 Cable characteristics

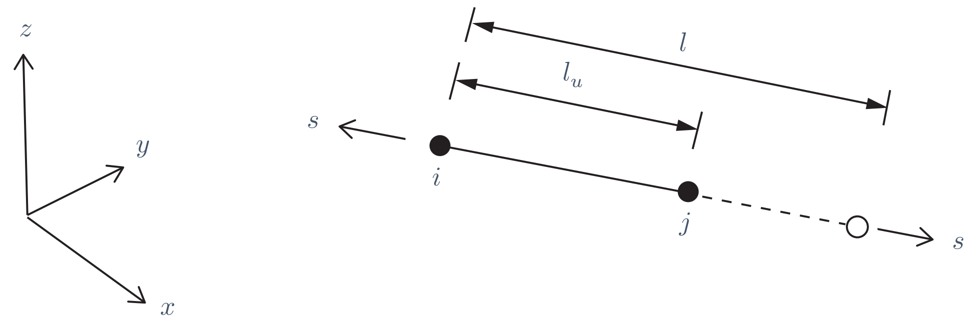

Figure 15. *Cable element between nodes i and j with unstrained length l_u is subjected to a normal force s.*

The main characteristic of a cable element is that it can only carry tensile forces. This fundamental property also implies that a larger network of cables is in need of prestressing to maintain as a stable structure in equilibrium under various loads. A cable element or network does in general not resist shear forces [28]. Furthermore, the flexural rigidity of cable elements may be neglected, which results in freely hanging elements automatically adopting to the most efficient shape under a given load, only carrying loads in tension. If such elements are properly implemented in a structural system, it becomes a materially efficient structural member, and can carry forces over vast distances, as exemplified in suspension bridges.

3.2.2 Form finding of cable networks

The cable net will need to have two known equilibrium shapes in the context of a flexible formwork. The first equilibrium shape is the unloaded but prestressed cable net that is used to verify the physical realization prior to the cast of concrete. The correct prestressing forces and geometry of the unloaded net needs to be known and verified in the construction process, otherwise, it is not possible to confirm the shape used in analysis, and the finalized shell structure will not have the designed properties. The unloaded, prestressed shape is also used to mount the membrane.

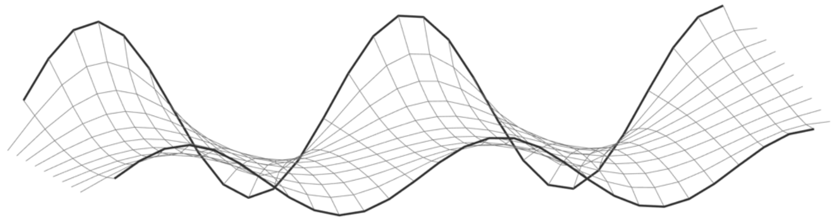

Figure 16. *Prestressed cable net design that has been form found with constant force densities using the linear formulation of FDM.*

The second equilibrium shape is the loaded cable net, subject to weight from the wet concrete. This is also the final shape that is offset (due to shell thickness) and used in FE analysis of the concrete shell in a later stage.

3.2.2.1 Choice of form finding method

Force Density Method is applied mainly due to the following reasons:

1) It is a materially independent method, without the need to predefine element properties before such data is of any practical use [29].
2) It is a linear method in its fundamental formulation, which makes it fast, direct and reliable. Especially suited for early design with preserved accuracy [30].
3) The derivation is rather straight forward, and a variety of non-linear constraints are easily implemented by slightly manipulating the Jacobian and residual function.
4) Force densities are suitable parameters for describing a net, and any stated force density corresponds to a unique shape [30].

3.2.2.2 Introduction to the Force Density Method

The Force Density Method (FDM) is known as a geometric stiffness method [31]. No information on material properties is necessary to find an initial geometry in equilibrium. In its fundamental form, the method is also linear, which is a great advantage in the early design process. The method has its origin in the early 70s. Tensile structures at the time had been designed using experimental form finding techniques based on physical models, and the geometry was mainly verified through photogrammetry techniques and physical measurements, as described in [10] and [11]. On the work on the Olympic Stadium in Munich, due to the complexity, a more mathematical approach was investigated. Photogrammetry on the small scale physical model where not providing enough accuracy to produce satisfactory building documentation. Therefore, in 1971, Linkwitz and Scheck published the first formulation of the Force Density Method (FDM) which was also applied in design of the same Stadium [10].

The linear and fundamental version of FDM produces arbitrary shapes by stating force densities (example in **Figure 16**) and an external force vector to derive a shape in equilibrium [30]. However, in many applications, the design intention is also to optimize the structure with regard to one or several parameters. Such constraints could be equal force distribution in the net or equal lengths of the elements, to name a few possibilities in a cable net context. For such known constraints, a minimization problem (non-linear) can be formulated [7].

Newton-Raphson's Method and Modified Newton's Method are used to solve the minimization problem in this thesis. Newton-Raphson has a quadratic convergence rate and modified Newton uses a semi-quadratic principle, with the difference how often the Jacobian is updated. The most suitable choice will mainly depend on the number of elements and degree of non-linearity [7].

The next few sections describe the fundamental features of the method, both linear and non-linear formulations. Extensions of the method will be used in the form finding of membranes, see section 3.3.2.1.

3.2.2.3 Discretization and Topology

Assume that there exists a set of free nodes with Cartesian coordinates $\boldsymbol{x} = [x_1\ x_2\ \cdots x_n]^T$, $\boldsymbol{y} = [y_1\ y_2\ \cdots y_n]^T$, $\boldsymbol{z} = [z_1\ z_2\ \cdots z_n]^T$ and a set of fixed nodes $\boldsymbol{x}_f = [x_{f,1}\ x_{f,2}\ \cdots x_{f,n}]^T$, $\boldsymbol{y}_f = [y_{f,1}\ y_{f,2}\ \cdots y_{f,n}]^T$, $\boldsymbol{z}_f = [z_{f,1}\ z_{f,2}\ \cdots z_{f,n}]^T$. All nodes are connected by one or several branches, together forming an arbitrary network. The topology of the network can be described by introducing a connectivity matrix $\boldsymbol{C}$, also mentioned as the branch-node matrix in some literature ([11], [30], [32]) such that contained elements assume

$$c_{k,i:j} = \begin{cases} +1 \text{ for branch } k \text{ connecting to node } i \\ -1 \text{ for branch } k \text{ connecting to node } j \\ \ 0 \text{ otherwise} \end{cases} \tag{2}$$

This can be exemplified in a small network to demonstrate the principle:

$$\boldsymbol{C} = \left[\begin{array}{ccc|ccc} \multicolumn{3}{c|}{\overbrace{\qquad\qquad}^{\boldsymbol{C}_N}} & \multicolumn{3}{c}{\overbrace{\qquad\qquad}^{\boldsymbol{C}_F}} \\ 1 & -1 & 0 & 0 & 0 & 0 \\ 0 & 1 & -1 & 0 & 0 & 0 \\ 1 & 0 & -1 & 0 & 0 & 0 \\ 1 & 0 & 0 & -1 & 0 & 0 \\ 0 & 1 & 0 & 0 & -1 & 0 \\ 0 & 0 & 1 & 0 & 0 & -1 \end{array}\right]$$

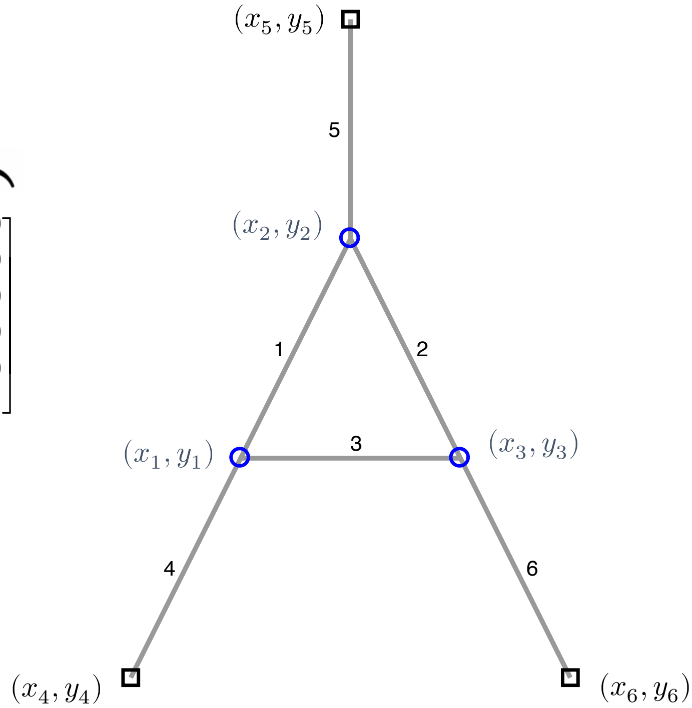

Figure 17. *Arbitrary network. Rectangular nodes are fixed coordinates and circles denote free coordinates. The branch-node matrix C is structured with nodes along columns with one row for each element's connectivity.*

$\boldsymbol{C} = [\boldsymbol{C}_N \quad \boldsymbol{C}_F]$ with $\boldsymbol{C}_N$ containing all free nodes of the topology and $\boldsymbol{C}_F$ all fixed nodes. This block matrix structure is practical in the formulation of equilibrium equations.

3.2.2.4 Equilibrium equations

Equilibrium of an arbitrary node within a cable network can be written as

$$s_{a,x} \cos(\alpha_{a,x}) + s_{b,x} \cos(\alpha_{b,x}) + \ \cdots + \ s_n \cos(\alpha_{n,x}) + p_x = 0 \tag{3}$$

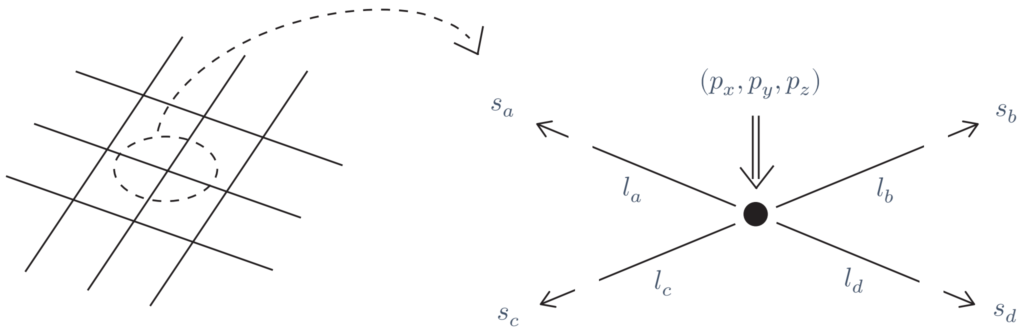

Figure 18. *Node equilibrium between internal and external forces in an arbitrary network of cables.*

with similar expressions for y and z respectively [33]. If the direction cosines are implemented as coordinate differences divided by the distance in space [11], the expression becomes

$$\frac{x_1 - x_0}{l_a} s_a + \frac{x_2 - x_0}{l_b} s_b + \cdots + \frac{x_m - x_0}{l_n} s_n + p_x = 0 \tag{4}$$

The force density for cable i is introduced as force over length [30]:

$$q_i = \frac{s_i}{l_i} \tag{5}$$

The equilibrium equation can thus be rewritten as

$$(x_1 - x_0)q_a + (x_2 - x_0)q_b + \cdots + (x_m - x_0)q_n + p_x = 0 \tag{6}$$

All equilibrium equations for the entire network can conveniently be stated together on matrix form. By defining the node coordinate differences as $\boldsymbol{u} = [x_{\boldsymbol{1}} - x_0 \; x_2 - x_0 \; \cdots x_n - x_0]^T$ with distances in y *and* z corresponding to analogous definitions $\boldsymbol{v}, \boldsymbol{w}$ respectively, and implementing the branch-node matrix $\boldsymbol{C}$**,** it is now possible to write the following equality on matrix form

$$\boldsymbol{u} = \boldsymbol{C}\boldsymbol{x} \tag{7}$$

The branch-node matrix can be subdivided into a free and fixed part $\boldsymbol{C} = [\boldsymbol{C}_N \; \boldsymbol{C}_f]$. With the same subdivision for free and fixed coordinates, the above equality can now be rewritten as (stated explicitly for all components [30]):

$$\begin{aligned} \boldsymbol{u} &= \boldsymbol{C}_N \boldsymbol{x}_N + \boldsymbol{C}_f \boldsymbol{x}_f \\ \boldsymbol{v} &= \boldsymbol{C}_N \boldsymbol{y}_N + \boldsymbol{C}_f \boldsymbol{y}_f \\ \boldsymbol{w} &= \boldsymbol{C}_N \boldsymbol{z}_N + \boldsymbol{C}_f \boldsymbol{z}_f \end{aligned} \tag{8}$$

With these identities, the element lengths can also be conveniently formulated as ([32])

$$\boldsymbol{l} = \sqrt{\boldsymbol{u}^2 + \boldsymbol{v}^2 + \boldsymbol{w}^2} \tag{9}$$

Now, the equilibrium equations are readily formulated on matrix form [11]:

$$\begin{aligned} \boldsymbol{C}^T \boldsymbol{U} \boldsymbol{L}^{-1} \boldsymbol{s} &= \boldsymbol{p}_x \\ \boldsymbol{C}^T \boldsymbol{V} \boldsymbol{L}^{-1} \boldsymbol{s} &= \boldsymbol{p}_y \\ \boldsymbol{C}^T \boldsymbol{W} \boldsymbol{L}^{-1} \boldsymbol{s} &= \boldsymbol{p}_z \end{aligned} \tag{10}$$

Capitalized parameters should be understood as a vector rearranged as a diagonal matrix. By using the definition of the force density, the expressions can be written as

$$\begin{aligned} \boldsymbol{C}^T \boldsymbol{U} \boldsymbol{q} &= \boldsymbol{p}_x \\ \boldsymbol{C}^T \boldsymbol{V} \boldsymbol{q} &= \boldsymbol{p}_y \\ \boldsymbol{C}^T \boldsymbol{W} \boldsymbol{q} &= \boldsymbol{p}_z \end{aligned} \tag{11}$$

With the relations $\boldsymbol{Uq} = \boldsymbol{Qu}$ and $\boldsymbol{u} = \boldsymbol{Cx}$, the equilibrium equations can be expanded to the form

$$\begin{aligned} \boldsymbol{C}^T \boldsymbol{Q} \boldsymbol{C} \boldsymbol{x} + \boldsymbol{C}^T \boldsymbol{Q} \boldsymbol{C}_f \boldsymbol{x}_f &= \boldsymbol{p}_x \\ \boldsymbol{C}^T \boldsymbol{Q} \boldsymbol{C} \boldsymbol{y} + \boldsymbol{C}^T \boldsymbol{Q} \boldsymbol{C}_f \boldsymbol{y}_f &= \boldsymbol{p}_y \\ \boldsymbol{C}^T \boldsymbol{Q} \boldsymbol{C} \boldsymbol{z} + \boldsymbol{C}^T \boldsymbol{Q} \boldsymbol{C}_f \boldsymbol{z}_f &= \boldsymbol{p}_z \end{aligned} \tag{12}$$

By introducing $\boldsymbol{D} = \boldsymbol{C}^T \boldsymbol{Q} \boldsymbol{C}$ and $\boldsymbol{D_f} = \boldsymbol{C}^T \boldsymbol{Q} \boldsymbol{C_f}$, the free node positions can now be expressed as functions of the force density on the linear form:

$$\begin{aligned} \boldsymbol{x} &= \boldsymbol{D}^{-1}(\boldsymbol{p}_x - \boldsymbol{D}_f \boldsymbol{x}_f) \\ \boldsymbol{y} &= \boldsymbol{D}^{-1}(\boldsymbol{p}_y - \boldsymbol{D}_f \boldsymbol{y}_f) \\ \boldsymbol{z} &= \boldsymbol{D}^{-1}(\boldsymbol{p}_z - \boldsymbol{D}_f \boldsymbol{z}_f) \end{aligned} \tag{13}$$

In the article by Scheck from 1974 [30], some important observations and conclusions are presented in this context:

1) The determination of free coordinates are linear equations.
2) The matrix $\boldsymbol{D}$ can be identified as the generalized Gaussian transformation of $\boldsymbol{C}$. The matrix is positive definite for prestressed networks ($\forall q_i > 0$).
3) For a chosen set of external loads acting on the network, any arbitrarily chosen force density vector corresponds to exactly one unique geometry in equilibrium. This makes the force densities suitable to describe cable network geometries.

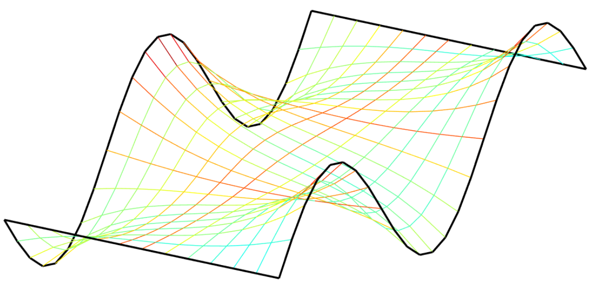

Figure 19. *Cable network form found with constant force density with trigonometric functions to define the boundary. Force distribution is shown with help of a color plot.*

Using linear formulation of FDM is useful in many applications, but also requires one to set force densities in a proper and practical distribution. This can sometimes be tedious but is simplified with methods such as Thrust Network Analysis (TNA) [34], where FDM is combined with Graphic Statics to define force densities in the study of funicular compressive shells [11]. TNA has been successfully applied on flexible formworks, as discussed by T. Van Mele in [35].

3.2.3 Constrained form finding

In many applications, the design intention is to optimize the structure with regard to one or several parameters. Such constraints could be equal force distribution in the net or equal lengths of the elements, to name a few possibilities in a cable net context. Very often however, the number of such linearly independent equations are less than the number of unknowns. With the known constraints, a minimization problem can be formulated [7].

$$\Delta \boldsymbol{q}^t \boldsymbol{q} \ \rightarrow min \tag{14}$$

In this thesis, least square problems are solved using the Newton-Raphson's Method, which has a quadratic convergence rate, and in some rare cases, Modified Newton's Method which uses a semi-quadratic principle, with the difference how often the Jacobian is updated [36]. The most suitable choice will mainly depend on the number of elements, as investigated and shown in [7]. This has to do with the CPU-time to calculate the inverse of the Jacobian, but also the inverse of the tangent stiffness matrix D, in the calculation of nodal coordinates. The required CPU-time has been shown to have exponential growth with the increase in number of elements [31].

3.2.3.1 General formulation

The general consideration for r additional conditions can be expressed as

$$\begin{gathered} g_1(\boldsymbol{x}, \boldsymbol{y}, \boldsymbol{z}, \boldsymbol{q}) = 0 \\ g_2(\boldsymbol{x}, \boldsymbol{y}, \boldsymbol{z}, \boldsymbol{q}) = 0 \\ \vdots \\ g_r(\boldsymbol{x}, \boldsymbol{y}, \boldsymbol{z}, \boldsymbol{q}) = 0 \end{gathered} \tag{15}$$

All constraints can be summed in the r - vector $\boldsymbol{g}(\boldsymbol{x}, \boldsymbol{y}, \boldsymbol{z}, \boldsymbol{q}) = \boldsymbol{0}$ [30]. As stated in the introduction of the method, the nodal coordinates can be expressed as functions of the force densities, and the constraint function can be simplified to $\boldsymbol{g}(\boldsymbol{x}(\boldsymbol{q}), \boldsymbol{y}(\boldsymbol{q}), \boldsymbol{z}(\boldsymbol{q}), \boldsymbol{q}) = \boldsymbol{g}^*(\boldsymbol{q}) = \boldsymbol{0}$. The procedure is to find a value of $\boldsymbol{q}$ such that $\boldsymbol{g}^*(\boldsymbol{q}) \approx \boldsymbol{0}$ within a given tolerance. The iteration step in force density is formulated as $\boldsymbol{q}^{(s+1)} = \boldsymbol{q}^{(s)} + \Delta \boldsymbol{q}$ where a value of $\Delta \boldsymbol{q}$ is sought with the linearized condition

$$\boldsymbol{g}^*(\boldsymbol{q}^{(s)}) + \frac{\partial \boldsymbol{g}^*(\boldsymbol{q}^{(s)})}{\partial \boldsymbol{q}} \Delta \boldsymbol{q} = \boldsymbol{0} \tag{16}$$

with the Jacobian $\frac{\partial g}{\partial q}$ defined as $\boldsymbol{G}^T$ and the residual of the constraint function defined as $\boldsymbol{r} = -\boldsymbol{g}^*(\boldsymbol{q}^{(s)})$, the linear conditions for $\Delta\boldsymbol{q}$ can thus be written on the form [7]

$$\boldsymbol{G}^T \Delta \boldsymbol{q} = \boldsymbol{r} \tag{17}$$

To find a unique solution to an underdetermined system of equations, the least square principle is used where $\Delta\boldsymbol{q}^t\boldsymbol{q} \ \rightarrow min$. To ensure numerical stability, a damped strategy is implemented although it will in general also increase the number of iterations to reach equilibrium. The advantage is that a problem will converge even with a poor first guess in $\boldsymbol{q}^{\boldsymbol{0}}$. With damping, the least squares problem can be expressed as $\Delta\boldsymbol{q}^t\boldsymbol{q} + \boldsymbol{a}^T\boldsymbol{P}\boldsymbol{a} \rightarrow min$ where $\boldsymbol{a}$ is a damping factor and $\boldsymbol{P}$ a diagonal weighting matrix. With a damped approach on the Gaussian transformation of $\boldsymbol{G}$, the Lagrange factor $\boldsymbol{k}$ are obtained by solving the obtained square $(\boldsymbol{r}, \boldsymbol{r})$ system

$$\boldsymbol{k} = \boldsymbol{T}^{-1}\boldsymbol{r} \tag{18}$$

The matrix $\boldsymbol{T}$ holds the defined matrices $\boldsymbol{T} = \boldsymbol{G}^T\boldsymbol{G} + \delta\boldsymbol{I}$, where δ is a damping factor and $\boldsymbol{I}$ is the identity matrix. This leads to the final definition of $\Delta\boldsymbol{q}$ as

$$\Delta\boldsymbol{q} = \boldsymbol{G}\boldsymbol{k} \tag{19}$$

The step in force density is repeated until the residual has vanished or is sufficiently small with regard to the tolerance [30]. This damped approach is also known as the Levenberg-Marquardt algorithm [35].

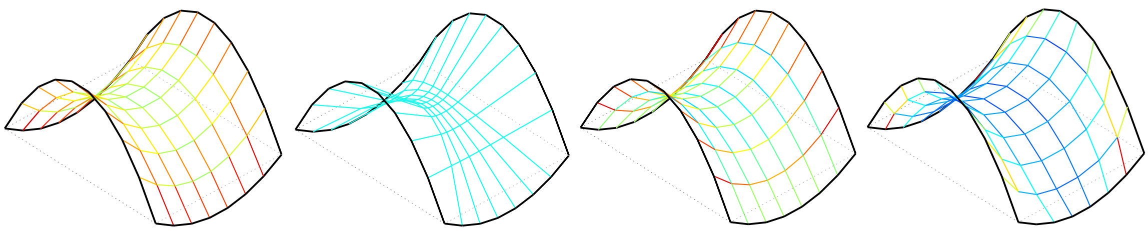

Figure 20. *Geometry and force distribution induced by the constraints (from left) constant force densities, constant forces, initial lengths/material stiffness, and target element lengths. All shapes have a residual smaller than 10^{-4} except for constant lengths (furthest to the right), where the applied constraint could only be fulfilled with norm of residuals stopping at approximately 10^{-2} for the given condition and boundary.*

3.2.3.2 Constraints based on material stiffness

Since FDM is a geometric stiffness method, it does not include material properties in its fundamental form. However, elastic properties is easily implemented through a constraint based on Hooke's law and is derived by Scheck [30] on the form:

$$\boldsymbol{l}_u = \frac{\boldsymbol{h}}{\boldsymbol{h}+\boldsymbol{s}}\boldsymbol{l} \tag{20}$$

$\boldsymbol{l}_u$ is the unstrained element lengths, $\boldsymbol{h} = \boldsymbol{EA}$ is the stiffness, and $\boldsymbol{s}$ denotes the element forces. The function subject to minimization can therefore be written

$$\boldsymbol{g}^*(\boldsymbol{q}) = \frac{\boldsymbol{h}}{\boldsymbol{h}+\boldsymbol{s}(\boldsymbol{q})}\boldsymbol{l}(\boldsymbol{q}) - \boldsymbol{l}_u \tag{21}$$

The formulation of the Jacobian $\boldsymbol{G}^T$ can be derived using the chain rule

$$\boldsymbol{G}^T = \frac{\partial \boldsymbol{g}^*}{\partial \boldsymbol{q}} = \frac{\partial \boldsymbol{g}}{\partial \boldsymbol{x}}\frac{\partial \boldsymbol{x}}{\partial \boldsymbol{q}} + \frac{\partial \boldsymbol{g}}{\partial \boldsymbol{y}}\frac{\partial \boldsymbol{y}}{\partial \boldsymbol{q}} + \frac{\partial \boldsymbol{g}}{\partial \boldsymbol{z}}\frac{\partial \boldsymbol{z}}{\partial \boldsymbol{q}} + \frac{\partial \boldsymbol{g}}{\partial \boldsymbol{q}} \tag{22}$$

By evaluating the partials using implicit derivatives, the Jacobian matrix can be formulated. With $\frac{\partial \boldsymbol{g}}{\partial \boldsymbol{q}} = \boldsymbol{L}$, $\frac{\partial \boldsymbol{g}}{\partial \boldsymbol{x}} = \boldsymbol{Q}\frac{\partial \boldsymbol{l}}{\partial \boldsymbol{x}}$, $\frac{\partial \boldsymbol{x}}{\partial \boldsymbol{q}} = -\boldsymbol{D}^{-1}\boldsymbol{C}^T\boldsymbol{U}$ **,** and equivalent formulations in $\boldsymbol{y}$ and $\boldsymbol{z}$, The Jacobian for length conditions becomes

$$\boldsymbol{G}_u^T = -\boldsymbol{L}_u^2\boldsymbol{H}^{-1} - \boldsymbol{L}_u^2\boldsymbol{L}^3(\boldsymbol{UCD}^{-1}\boldsymbol{C}^T\boldsymbol{U} + \boldsymbol{VCD}^{-1}\boldsymbol{C}^T\boldsymbol{V} + \boldsymbol{WCD}^{-1}\boldsymbol{C}^T\boldsymbol{W}) \tag{23}$$

This constraint is necessary for any structure where the cable element lengths are stated or known prior to the form finding process. The constraint is also useful if the initial but unloaded prestressed form is of interest. When the cable net (and membrane cover) is loaded with the wet concrete, this constraint will predict the deformed shape during the concrete drying stage and will also inform the user of the final shape of the shell under its own self-weight. Since it is not practically possible to load the net evenly with concrete at once, this constraint can also help to point out temporary but critical deformations during the cast process, where the designer can follow the change in deformation over the entire cast time line. However, the accuracy in such a time dependent prediction is yet to be verified.

If this constraint is <u>not</u> used in form finding, the unstrained lengths can instead be derived directly from equation (20) based on the form found values of force and strained element lengths.

There's some suggestions in [30] how to set the damping factor δ. These recommendations where evaluated but ultimately replaced by the author with the following suggestion for constraints based on unstrained length conditions

$$\delta_u = k_u \left(\frac{1}{n} \sum_{i=1}^{n} E_i A_i \right)^{-2} \tag{24}$$

which was systematically tested and derived from a machine learning inspired approach, involving the parameters p, EA and a reduction factor h that is added on the stiffness for elements with temporary negative force densities. The constant in the expression was mostly set to $k_u = 2500$, which in general gave the least amount of iterations.

3.2.3.3 Constraints based on force conditions

In situations where the force distribution in the net needs to be controlled or partly prescribed, the following constraint function can be used

$$\boldsymbol{g}^*(\boldsymbol{q}) = \boldsymbol{Q}\boldsymbol{l} - \boldsymbol{s}_f \tag{25}$$

$\boldsymbol{s}_f$ denotes the prescribed force distribution in the net that is desired, with $\boldsymbol{Q}$ and $\boldsymbol{l}$ being the force density matrix and element length vector respectively. In the same manner as described in 3.2.3.2, the Jacobian can be derived and takes the explicit form of

$$\boldsymbol{G}_f^T = \boldsymbol{L} - \boldsymbol{Q}\boldsymbol{L}^{-1}(\boldsymbol{U}\boldsymbol{C}\boldsymbol{D}^{-1}\boldsymbol{C}^T\boldsymbol{U} + \boldsymbol{V}\boldsymbol{C}\boldsymbol{D}^{-1}\boldsymbol{C}^T\boldsymbol{V} + \boldsymbol{W}\boldsymbol{C}\boldsymbol{D}^{-1}\boldsymbol{C}^T\boldsymbol{W}) \tag{26}$$

In the case of force constraints, a damped approach also added robustness for some problems, but in this case, a constant factor was sufficient:

$$\delta = k_v \tag{27}$$

The constant where determined as $k_v = 5.85 \times 10^{-5}$ in a rather heuristic approach. The number of iterations needed with this constraint is usually quite small which allowed for a manually optimized damping factor.

The force constraint is equivalent to conditions of a minimum way net, assuming that an equilibrium state can be found where all branches assume the same force. This remarkable property is proved by Scheck in [30]. Equal force is desirable in the context of flexible formwork with regard to the material usage and introduces suitable lines for fabric patterning through its relation with a geodesic line.

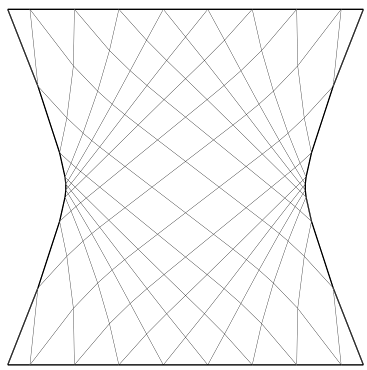

Figure 21 (Left). *Form found minimum surface based on force constraint. Note the increased node density in areas on the sides, resulting in unequal element lengths.*

(Right). *Form finding based on predefined lengths given by 2D quad-mesh mapped on a hyperbola surface. Top and bottom boundaries are fixed.*

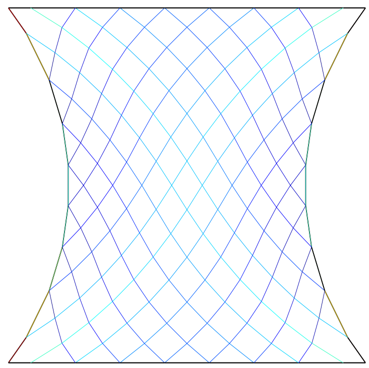

When form finding a minimum way net, some practical aspects arise. As seen in **Figure 21 (Left)**, form finding subject to force constraints usually result in large inequalities in element lengths (note the contrary colormap variations showing force distribution in **Figure 21 (Right)**). This is not convenient in the construction and cable assembling process, thus a balance between equal cable lengths and equal stresses needs to be found. It is possible to form find multiple weighted constraints on target lengths and forces, which was exemplified and used in the construction of Mannheim Multihalle [11].

One should keep in mind that the force constraint is sensitive to the topology and orientation of mesh. For some problems, several nodes tend to implode to the same position, which is of course a natural consequence of minimizing sum of lengths. For such cases, form finding with squared sum of lengths will give more useful results. This is equal to constant force densities instead of constant forces [31].

3.2.3.4 Constraints on node distances

Constraints on node distances can be beneficial in a number of ways. For instance, consider a net that should carry panels with the same size, or situations where the structural elements have very high stiffness and equilibrium for such a network is to be found. The residual for this condition can be formulated as

$$\boldsymbol{g}^*(\boldsymbol{q}) = \boldsymbol{l} - \boldsymbol{l}_v \tag{28}$$

The vector l_v denotes the prescribed distance conditions. Following the same principles in the derivation of the Jacobian as in previous instances, the explicit form can be written as

$$\boldsymbol{G}_d^T = -\boldsymbol{L}^{-1}(\boldsymbol{U}\boldsymbol{C}\boldsymbol{D}^{-1}\boldsymbol{C}^T\boldsymbol{U} + \boldsymbol{V}\boldsymbol{C}\boldsymbol{D}^{-1}\boldsymbol{C}^T\boldsymbol{V} + \boldsymbol{W}\boldsymbol{C}\boldsymbol{D}^{-1}\boldsymbol{C}^T\boldsymbol{W}) \tag{29}$$

This constraint is also useful when searching for a network where the forces are as similar as possible but a practical balance still needs to be achieved with regard to element lengths. Such weighted constraints was ultimately not explored further in this thesis.

3.2.3.5 Constraints on node positions

Constraints on target node positions was never implemented, but is mentioned for completeness as it is useful to approach a target surface and therefore useful in the context of flexible formwork. The interested reader is referred to [7], [11] & [35].

3.2.3.6 Mixed constraints

Since the structure of the matrices $G_d, G_f,$ and G_u are similar, a network can be form found with a combination of constraints. For instance, there might be different demands on a network in different places, such as minimizing force in parts of a structure while connections at the boundary might request more equal node distances. This can be achieved by simply stacking different constraints for different elements and corresponding derivatives, as suggested in [30].

3.2.3.7 Convergence criteria

Residuals are calculated as follows:

1) Force constraint: Equation (25)
2) Length constraint: Equation (28)
3) Material constraint: Equation (20)

Error is defined as

$$e = \|\boldsymbol{g}^*(\boldsymbol{q})\| = \sqrt{g_1^2 + g_2^2 \cdots + g_n^2} \tag{30}$$

With convergence criteria that $e \leq \text{tol}$. A tolerance (tol) of 10^{-5} is used. For the material constraint, the tolerance has been increased as a compromise between accuracy and computational speed, assuming 10^{-3} for this constraint instead. This had a neglectable influence on the result for all tested problems, with neglectable difference in final node positions.

3.2.3.8 Alternative formulations

A slightly different formulation to solve a least squares problem subject to constraints is discussed by K. Linkwitz and D. Veenendaal in [11]. The outcome is essentially the same, but the derivatives are made with regard to node coordinates instead of rewriting them as functions of force densities. Such an approach is suggested to be faster according to [7]. However, with modern computers, this might be of less relevance, especially if the stiffness matrix inversion is done with Cholesky decomposition (method described in [37]). This approach is implemented in section 3.3.2 in the form finding of membranes, and performance with or without Cholesky decomposition has been evaluated. This allows for a comparison and evaluation of the two different approaches.

3.2.4 Load generation

The cable network load model is informed by the concrete shell analysis, where the shell thickness and sagging (3.3.4) will greatly influence the equivalent external forces acting in the network nodes. Each node has a contributary area of which the node force is calculated based on specific weight of concrete (24 kN/m^3). It is of course important to update such loads if the contributing area of each quadrilateral changes significantly during form finding.

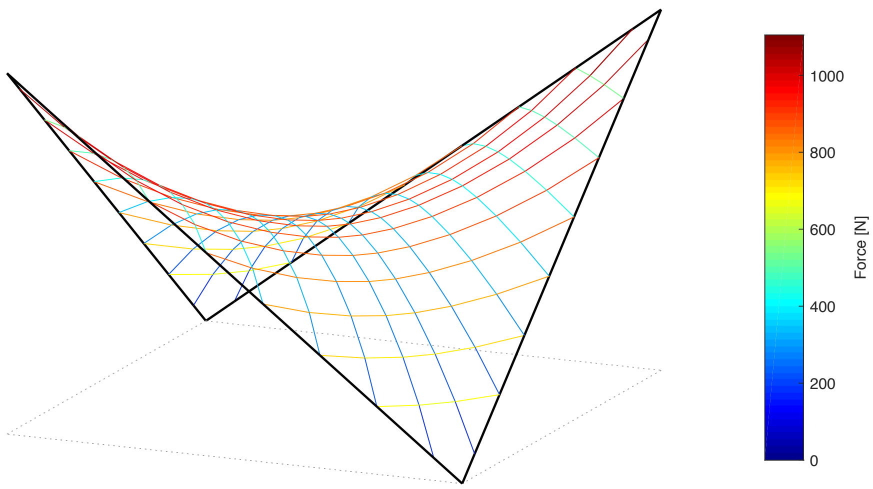

Figure 22. *A 'hypar' cable net, form found in two steps, first with a force constraint to find a prestressed minimum way net, secondly with material stiffness constraints in combination with added external loading to analyze the change in force distribution.*

3.2.5 Verification

FDM is a well-established and verified method in the form finding of cable networks. A basic catenary problem is chosen as benchmarking for the material constraint. The linear method is verified with empirical results from the case study in section 4.4.

3.2.5.1 Catenary

A high element stiffness ($E = 210\ GPa$) and a neglectable vertical load in the nodes of 1 N is chosen such that element deformations does not affect the analytical comparison. Span is 3 m with a total element length of 3.66 m. When comparing strained and unstrained lengths, there is no deviation in the first 6 decimals, confirming the assumption of neglectable deformations. The remaining error presented in **Table 1** is believed to come mainly from the rather coarse discretization.

Table 1. *Comparison of node positions in y-direction [m], with origo in the node to the left. There is a small deviation in y-position, expected from the rather coarse discretization.*

	Node 1	**Node 2**	**Node 3**	**Node 4**	**Node 5**
Numerical	-0.4588	-0.8035	-0.9392	-0.8035	-0.4588
Analytical	-0.4524	-0.7920	-0.9254	-0.7920	-0.4524
Error [%]	1.41	1.45	1.49	1.45	1.41

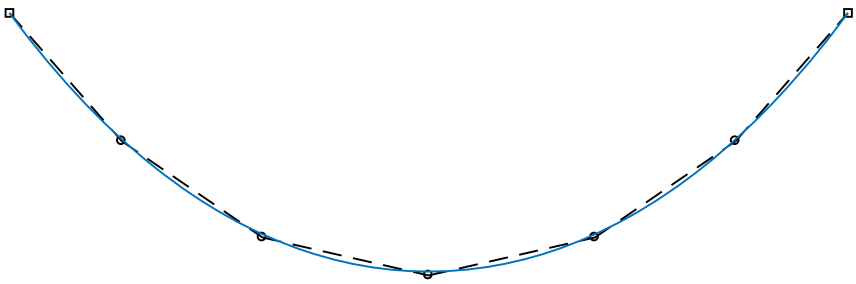

Figure 23. *Verification of cable form finding through a comparison with the analytical solution of the catenary. Circular nodes refer to Node 1 – 5 seen from left to right.*

3.2.5.2 Hypar

A ruled surface is tested to verify that the force constraint induce straight lines when assuming constant force (**Figure 24**). This is equivalent to a minimum way net, and as such, all continuous lines should be straight with this topology.

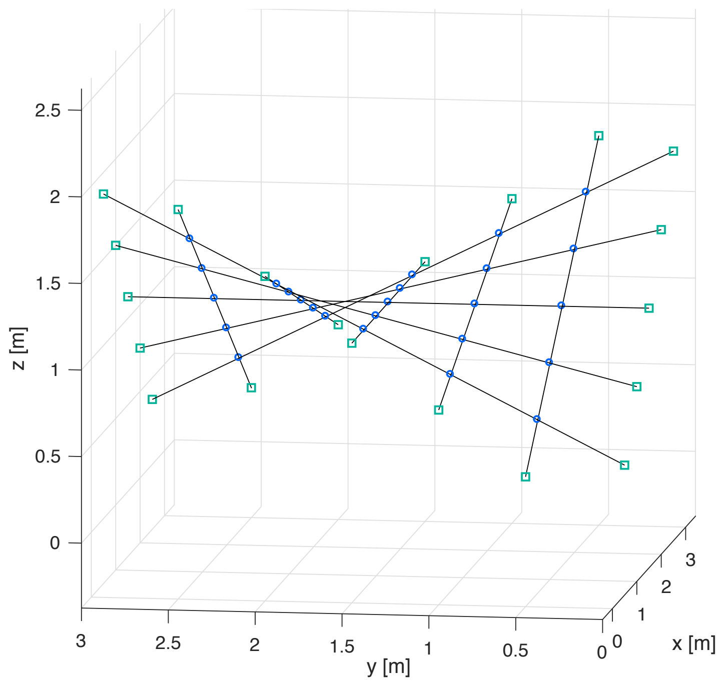

Figure 24. *Ruled surface, known as the hypar. With the given topology, all lines are straight, assuming a constant force is adopted.*

3.2.6 Conclusions

- Linear FDM is a fast and easily implemented method for generating arbitrary geometries in equilibrium. It has the advantage of being independent of material stiffness. It is the only linear form finding method known to the author.

- Form finding with regard to material properties is highly sensitive to the initial guess in force densities. The same strict dependence was not found for the other constraints. In this thesis, that guess was automated and set equally for all elements as

$$q_0 = k \frac{1}{n} \sum_{i=1}^{n} p_{z,i} \tag{31}$$

- In general, form finding with material stiffness converges rather slowly. Thousands of iterations are more rule than exception. Elements with $q < 0$ shows a clear relation to slow convergence rates and has been found key to solving problems fast. The easiest remedy is to increase pre-tension in individual elements or even the entire network. A constant for temporarily reducing the stiffness of members in compression is needed.

- The force constraint has interesting connections to geodesic lines. The constraint corresponds to a minimum way net as proved in [30].

- Constant force densities are equivalent to a minimized squared sum of lengths.

- A damped approach is needed for most non-linear conditions. Especially with increasing number of elements in the network. The damping for constraints on material stiffness was presented in Equation (24), which is based on an average optimum with respect to variations in external force, element stiffness, and reduction of stiffness for members in temporary compression.

- Numerical ill-conditioning is handled by scaling the stiffness matrix once it becomes singular. This has been sufficient in all tested problems. The complete matrix has been scaled so far. Such an approach can most likely be improved by identifying the cause of singularity more locally in the stiffness matrix.

- In the case of cable net form finding, the implemented non-linear constraints are minimized by stepping in force densities, $\Delta\boldsymbol{q}$**.** The main benefit of this is of course that the unknown coordinates are functions of the same parameter, $\boldsymbol{x}(\boldsymbol{q}), \boldsymbol{y}(\boldsymbol{q}), \boldsymbol{z}(\boldsymbol{q})$, which leads to a residual function $\boldsymbol{g}^*(\boldsymbol{q})$ that can be evaluated through single variable calculus. There is only one Jacobian to calculate, and the formulation becomes rather elegant. On the downside, the Jacobian tends to grow rather big, which potentially makes the step computationally expensive. In the case of membranes, it will be demonstrated how to step directly in coordinates instead of force densities, with a residual function $\boldsymbol{g}(\boldsymbol{x}, \boldsymbol{y}, \boldsymbol{z}, \boldsymbol{q})$. In practice, one Jacobian for each unknown coordinate component can be formulated, with smaller computational cost upon inversion for calculation of each of the coordinate steps, but also resulting in more dense coding. Ultimately, there was no time to fully evaluate if any of the formulations is a better approach in general.

- The functions are written on a general form and can be used to find geometry and analyze structures such as the arena cable net roof of Scandinavium, Gothenburg. The computational framework has also been successfully applied on cable truss models. As such, there is no limitation to only formwork applications.

3.3 Membrane analysis

A membrane will be mounted to the cable network to transfer concrete load to the cables in a practical way, acting as a surface to cast against. The membrane is a temporary part of the structure, as the cable network, and will be removed once the concrete has hardened and reached sufficient strength. Strictly membrane based formwork and/or guide work is actually sufficient to act as concepts on their own [21]. The theory in this chapter is presented with that in mind.

Some examples of stay-in-place fabrics exist in the context of other flexible formwork concepts [18]. Such systems are not considered in this thesis but may serve as an interesting alternative to the currently studied concept.

Figure 25. *Concrete shell constructed with a stay-in-place fabric formwork at ETH Zurich.*

3.3.1 Membrane characteristics

The main characteristic of a membrane, much like cables, is that it carries and transfers load in tension. A major difference in comparison with cables is however that it acts bidirectional (two dimensional element) and has an in plane shear stiffness, even if the shear capacity is generally small or neglectable. There is no out of plane rigidity [10]. Therefore, membrane structures are often subject to large deformations (in similarity with cable networks), and geometric stiffness is therefore important. As a natural consequence, this also means that the analysis procedure is commonly non-linear [21]. Prestressing is often necessary to achieve a predictable structural behavior. Due to its structural properties, membranes are rather insensitive to vibrations and seismic loads (even if main connectors might not be) [10].

The most commonly used type of membrane are different types of textiles. Material properties of textiles are usually not uniform, meaning that stiffness varies depending on the load direction. This potentially makes the analysis quite complex. The designer needs to consider the woven texture and structure, which is often organized in what is called warp and weft directions. The weaving pattern is often arranged with threads crossing each other in 90 degrees. One direction has stretched threads (weft) while the other has often threads passing over and under in an interchanging pattern (warp). Naturally, this means that deformations will be larger in the latter. Loading such a pattern in 45° direction will give even larger (shear) deformations [21]. By actively choosing fabric orientation, structural behavior can be accurately predicted, but it needs to be clearly defined in the model.

Keeping the described general behavior in mind, material properties lies outside the scoop of this thesis, and membranes will ultimately be treated as uniform (isotropic) in character for simplicity.

3.3.2 Form finding of membranes

Many extensions for the original formulation of FDM has been proposed for membranes. Some commonly recited work has been made by Pauletti/Pimenta [38], Bletzinger [39], Singer [40], Maurin/Motro [41], Koohestani [42], and most recently, D. Veenendaal [31], who made an extensive overview and comparison of different methods while also laying new ground for hybrid methods.

Most methods are formulated to achieve minimum surface solutions, which are also practical and proven forms for membrane structures [10]. A soap film analogy can be used to achieve such structures empirically [39], as has also been done extensively in the research on lightweight structures by Frei Otto [2]. Heinz Isler has also performed many interesting empirical studies [16]. For instance, he hanged watered sheets freely in different forms (**Figure 26**), left out in the winter cold, to be inverted to compressive ice shells when frozen. Form finding in such a way is a good example of creating shapes based on material stiffness constraints, since the form is induced and deformed by self-weight. Stresses over the frozen fabric are not constant as in the case of the soap bubble. As such, these two experimental studies also demonstrate the most useful constraints in the form finding of membranes. These will be implemented in the developed computational framework.

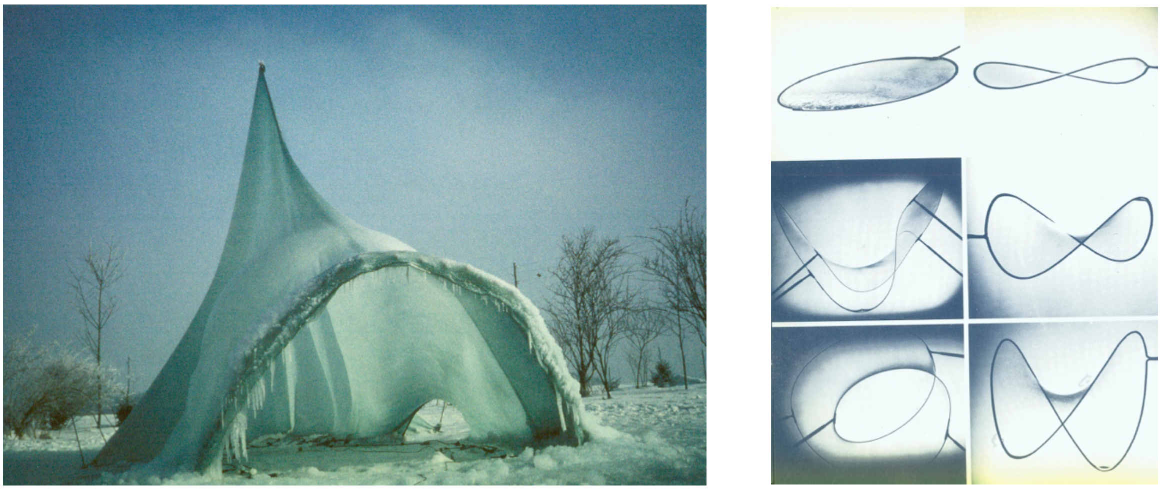

Figure 26. *Left: Ice shell experiment by Heinz Isler [43]. Right: Soap film experiments by Frei Otto [2].*

3.3.2.1 Choice of form finding method

The Surface Stress Density Method (SSDM) will be applied in the finding of minimal surfaces. This choice is motivated by comparison of methods in [7], which suggests that this is one of the fastest methods. SSDM is also sharing much of the original formulation of FDM done by Scheck and Linkwitz [44]. Natural Force Density Method (NFDM) is chosen as basis for the material constraint as this is the only method for membranes that preserves the linear qualities of original FDM [38]. The linear formulation is useful for design and analysis when assigning force densities is sufficient, with the same reasoning as for FDM (section 3.2.2.4). Similar with FDM, the analysis becomes non-linear when adding the material constraint.

3.3.2.2 Discretization and topology

Triangular elements are used for discretization of membranes in this thesis, using the constant strain triangle (CST) element (**Figure 27**). The formulation is relatively straight forward while the accuracy is usually sufficient [7]. The CST element formulation used for form finding is equivalent to the one used in FE analysis of membrane stresses which becomes an advantage in the partly repeated discretization work of shells in section 3.4.1.3. Triangular elements are suitable to discretize doubly curved surfaces as it avoids problems with preserving planarity. Quadrilateral or other elements can also be used but might need to be implemented with a higher order approximation to maintain the same accuracy or better.

Membrane stresses are converted to forces acting along the edges of the triangular element. By doing so, the triangle can be represented by a set of three line elements that can each have a force density defined. The element connectivity matrix can thus be defined in analogy with the line element in section 3.2.2.3. The sides of the triangle are described by three branches connecting three nodes $P_1(x_1, y_1, z_1)$, $P_2(x_2, y_2, z_2)$,

$P_3(x_3, y_3, z_3)$, as shown in **Figure 27**. As recalled from section 3.2.2, the connectivity matrix is established with the following rule [30]:

$$c_{k,i:j} = \begin{cases} +1 \text{ for branch } k \text{ connecting to node } i \\ -1 \text{ for branch } k \text{ connecting to node } j \\ \ \ 0 \text{ otherwise} \end{cases}$$

The set of three branches that form the k'th triangular element can be summed in a local connectivity matrix [42]

$$\boldsymbol{C}_{k,t} = \begin{bmatrix} 0 & -1 & 1 \\ 1 & 0 & -1 \\ -1 & 1 & 0 \end{bmatrix} \tag{32}$$

compared to the line element,

$$\boldsymbol{C}_{k,b} = [-1 \quad 1] \tag{33}$$

The matrices $\boldsymbol{C}_k$ are then assembled in the global branch-node matrix $\boldsymbol{C}$ which can be made in a combination of line and triangular elements. For adjacent triangles sharing two nodes, the assembling process results in two edge elements connecting and joining the two same nodes, which can also be complemented with a cable element simultaneously. Such a scenario would result in three equal rows in $\boldsymbol{C}$**,** corresponding to three different elements. The global connectivity matrix containing triangular and line elements can be written as a block matrix [7]:

$$\boldsymbol{C} = \begin{bmatrix} \boldsymbol{C}_{N,b} & \boldsymbol{C}_{F,b} \\ \boldsymbol{C}_{N,t} & \boldsymbol{C}_{F,t} \end{bmatrix} \tag{34}$$

N and F represents free and fixed nodes. b and t denotes branches and triangles respectively. This block matrix arrangement allows for analysis of structures consisting of combinations of different element types. The same order should be preserved when assembling the force density vector and element lengths [7]:

$$\boldsymbol{q} = [\boldsymbol{q}_b \ \boldsymbol{q}_t]^T \tag{35}$$

$$\boldsymbol{l} = [\boldsymbol{l}_b \ \boldsymbol{l}_t]^T \tag{36}$$

The explicit force densities of triangular elements are presented in separate sections for each constraint respectively as they are not the same. Fundamental definitions are derived in the next section, 3.3.2.3. The length vector corresponding to the edges of triangle element k can be written $\boldsymbol{l}_k = [l_{k,1}\ l_{k,2}\ l_{k,3}]^T$, with the three side lengths $l_{k,i}$. The element surface area can be calculated using Heron's formula ([40] & [45]):

$$A_k = \frac{1}{4}(\boldsymbol{l}_{\boldsymbol{k}}^T \boldsymbol{L}_{\boldsymbol{k}} \boldsymbol{N} \boldsymbol{L}_{\boldsymbol{k}} \boldsymbol{l}_{\boldsymbol{k}})^{\frac{1}{2}}, \qquad \text{with } \boldsymbol{N} = \begin{bmatrix} -1 & 1 & 1 \\ 1 & -1 & 1 \\ 1 & 1 & -1 \end{bmatrix} \tag{37}$$

The element will be defined in local coordinates, and a transformation T: $\mathbb{R}^2 \rightarrow \mathbb{R}^3$ from local to global coordinates (and vice versa) is needed. This mapping is done between a locally defined plane in $(\bar{x}, \bar{y})$, and the global Cartesian coordinates (x, y, z). Formulations of the transformation has been left for section 3.4.1.4, where it is naturally occurring in the derivation of stiffness matrices and element forces on the subject of shell theory. There, the same transformation is combined with a parent domain transformation for shell elements. Therefore, it is more practical to present them together.

3.3.2.3 Equilibrium equations

The equilibrium equations are equivalent with that of cable networks in section 3.2.2.4. However, the definition of the force density vector $\boldsymbol{q}_t$ for triangular elements differs from $\boldsymbol{q}_b$ and is derived below.

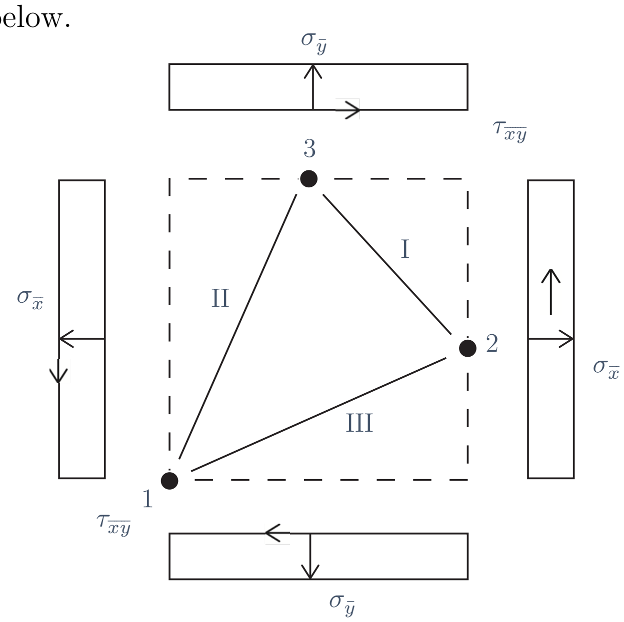

Figure 27. *Constant strain triangle element.*

The in plane stresses for each triangular membrane element k are [42]

$$\boldsymbol{\sigma}_k = [\sigma_{\bar{x}}\ \sigma_{\bar{y}}\ \tau_{\overline{xy}}]^T \tag{38}$$

where σ_i denotes normal stresses and $\tau_{\overline{xy}}$ is the shear stress within the membrane, described in the local plane. The correlation between natural and Cartesian stresses can be expressed with a matrix $\boldsymbol{\psi}$ [7], containing the direction cosines stated in section 3.2.2.4:

$$\boldsymbol{s} = \boldsymbol{\psi}^{-T}\boldsymbol{\sigma} \quad or \quad \boldsymbol{\sigma} = \boldsymbol{\psi}^{\boldsymbol{T}}\boldsymbol{s} \tag{39}$$

$$\boldsymbol{\psi} = \boldsymbol{L}_0^{-2}\boldsymbol{H} = \begin{bmatrix} l_1 & . & . \\ . & l_2 & . \\ . & . & l_3 \end{bmatrix}^{-2} \begin{bmatrix} u_1^2 & v_1^2 & u_1v_1 \\ u_2^2 & v_2^2 & u_2v_2 \\ u_3^2 & v_3^2 & u_3v_3 \end{bmatrix} \tag{40}$$

l_i should be understood as side lengths of the triangle, with u_i and v_i being node distance components, as seen in **Figure 28**. The same matrices is used in the explicit formulation of force densities for triangular elements as the membrane stresses are converted to force densities acting along the triangle sides, defined in local coordinates [42]:

$$\boldsymbol{q}_t = At\boldsymbol{H}^{-T}\boldsymbol{\sigma} \tag{41}$$

$$\boldsymbol{H}^{-T} = \frac{1}{4A^2}\begin{bmatrix} -v_2v_3 & -u_2u_3 & v_2u_3 + u_2v_3 \\ -v_3v_1 & -u_3u_1 & v_3u_1 + u_3v_1 \\ -v_1v_2 & -u_1u_2 & v_1u_2 + u_1v_2 \end{bmatrix} \tag{42}$$

With everything written out explicitly, the expression becomes [7]

$$\begin{bmatrix} Q_1 \\ Q_2 \\ Q_3 \end{bmatrix} = \frac{t}{4A}\begin{bmatrix} -v_2v_3 & -u_2u_3 & v_2u_3 + u_2v_3 \\ -v_3v_1 & -u_3u_1 & v_3u_1 + u_3v_1 \\ -v_1v_2 & -u_1u_2 & v_1u_2 + u_1v_2 \end{bmatrix} \begin{bmatrix} \sigma_{\bar{x}} \\ \sigma_{\bar{y}} \\ \tau_{\overline{xy}} \end{bmatrix} \tag{43}$$

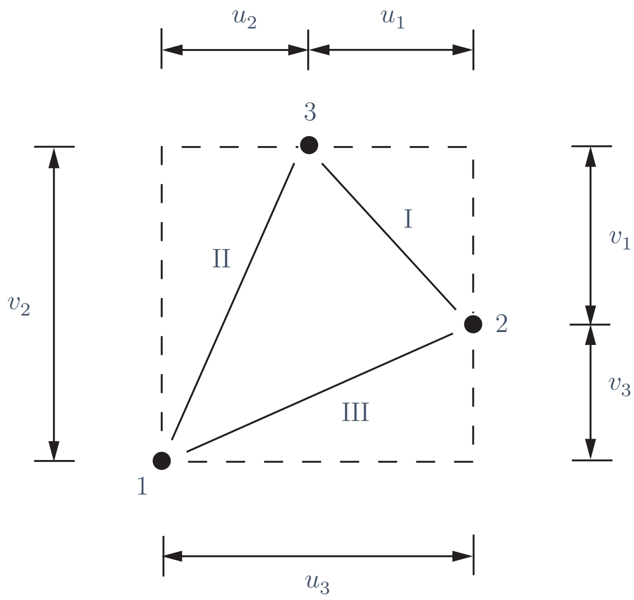

Figure 28. *Definitions of element numbering and node distances of the CST element.*

3.3.3 Constrained form finding

In the context of flexible formwork, material stiffness and minimization of surface area has been identified as useful constraints in membrane form finding. The following sections present both constraints explicitly.

3.3.3.1 Constraints on stresses (minimum surfaces)

Surface stress density method presents an analogue to the force densities [41], called the surface stress density, which is defined as

$$\boldsymbol{Q}_s = \frac{\boldsymbol{\sigma}_o}{A} \tag{44}$$

$\boldsymbol{\sigma}_0$, in the context of minimal surfaces, are a uniform and isotropic stress $\boldsymbol{\sigma}_0 = [\sigma_0 \ \sigma_0 \ 0]^T$, with $\sigma_0 > 0$. Since the surface stresses are constant, this will produce a geometry that is minimized with regard to the sum of element areas [46]. Due to the uniform isotropic stress state, shear stresses becomes zero. For simplicity, if σ_0 and t are chosen as 1, the reduced expression of the force density presented in section 3.3.2.2 becomes ([7])

$$\boldsymbol{q}_{t,s} = \frac{1}{4}\boldsymbol{NLl} \tag{45}$$

$\boldsymbol{L}$ represents the diagonal matrix of $\boldsymbol{l}$. To be clear, $\boldsymbol{l}$ contains three side lengths per element, stacked in one row vector. $\boldsymbol{N}$ has been defined in Equation (37) as part of Heron's formula. As seen from this expression, the force density becomes a function of the squared element side lengths.

With all key elements defined, Newton-Raphson's method can be applied in the search of a solution. In order to solve the non-linear problem, the system of equilibrium equations can be linearized. The residuals with respect to internal and external forces are defined as [11]

$$\begin{aligned} \boldsymbol{g}(\boldsymbol{x}) &= \boldsymbol{C}_N^T\boldsymbol{QCx} - \boldsymbol{p}_x \\ \boldsymbol{g}(\boldsymbol{y}) &= \boldsymbol{C}_N^T\boldsymbol{QCy} - \boldsymbol{p}_y \\ \boldsymbol{g}(\boldsymbol{z}) &= \boldsymbol{C}_N^T\boldsymbol{QCz} - \boldsymbol{p}_z \end{aligned} \tag{46}$$

The linearization can be written (with similar expressions for y and z) [30]:

$$\boldsymbol{g}(\boldsymbol{x}) + \frac{\partial \boldsymbol{g}(\boldsymbol{x})}{\partial \boldsymbol{x}}\Delta\boldsymbol{x} = \boldsymbol{0} \tag{47}$$

In similarity with definitions in section 3.2.3, the step in coordinates has been formulated in a modified damped approach in this thesis (assuming that the number of independent constraints and number of equations are the same). Although it has not been found explicitly on this form in any recited text, it has been numerically verified to hold and behaves convergently for all tried problems:

$$\Delta \boldsymbol{x} = (\boldsymbol{G}_{x,s} + \delta \boldsymbol{I})^{-\mathbf{1}} \boldsymbol{r} \tag{48}$$

The residual is again defined as $\boldsymbol{r} = -\boldsymbol{g}(\boldsymbol{x})$. In the formulation of the geometrical stiffness matrix $\boldsymbol{G}_s$, the force density derivatives with respect to coordinates needs to be derived [7]:

$$\frac{\partial \boldsymbol{q}_{t,s}}{\partial \boldsymbol{x}} = \frac{1}{4} \boldsymbol{N} \frac{\partial \boldsymbol{L} \boldsymbol{l}}{\partial \boldsymbol{x}} = \frac{2}{4} \boldsymbol{N} \boldsymbol{L} \frac{\partial \boldsymbol{l}}{\partial \boldsymbol{x}} = \frac{1}{2} \boldsymbol{N} \boldsymbol{U}^T \boldsymbol{C}_N \tag{49}$$

$$\frac{\partial \boldsymbol{q}_{t,s}}{\partial \boldsymbol{y}} = \frac{1}{2} \boldsymbol{N} \boldsymbol{V}^T \boldsymbol{C}_N \tag{50}$$

$$\frac{\partial \boldsymbol{q}_{t,s}}{\partial \boldsymbol{z}} = \frac{1}{2} \boldsymbol{N} \boldsymbol{W}^T \boldsymbol{C}_N \tag{51}$$

With expressions of the node distances as defined in the general formulation of FDM (section 3.2.2.4), their derivatives with respect to x, y and z becomes [30]:

$$\frac{\partial \boldsymbol{u}}{\partial \boldsymbol{x}} = \frac{\partial \boldsymbol{v}}{\partial \boldsymbol{y}} = \frac{\partial \boldsymbol{w}}{\partial \boldsymbol{z}} = \boldsymbol{C}_N \tag{52}$$

By using the product rule on the residual function $\frac{\partial \boldsymbol{g}(\boldsymbol{x})}{\partial \boldsymbol{x}}$, the geometrical stiffness matrix with respect to $\boldsymbol{x}$ becomes (with equivalent expressions for $\boldsymbol{y}$ and $\boldsymbol{z}$):

$$\boldsymbol{G}_{x,s} = \frac{\partial \boldsymbol{g}(\boldsymbol{x})}{\partial \boldsymbol{x}} = \boldsymbol{C}_N^T \boldsymbol{Q} \frac{\partial \boldsymbol{u}}{\partial \boldsymbol{x}} + \boldsymbol{C}_N^T \boldsymbol{U} \frac{\partial \boldsymbol{q}_{t,s}}{\partial \boldsymbol{x}} \tag{53}$$

With derivates of the force density and node distances inserted in the equation above, the geometrical stiffness explicitly becomes [7]

$$\boldsymbol{G}_{x,s} = \boldsymbol{C}_N^T \boldsymbol{Q} \boldsymbol{C}_N + \frac{1}{2} \boldsymbol{C}_N^T \boldsymbol{U} \boldsymbol{N} \boldsymbol{U}^T \boldsymbol{C}_N \tag{54}$$

With known expressions for residual functions and the geometric stiffness matrix, the node coordinates are updated by applying Newton-Raphson's Method until convergence within acceptable tolerance is reached.

$$\boldsymbol{x}_{i+1} = \boldsymbol{x}_i + \Delta \boldsymbol{x} \tag{55}$$

The damping is chosen constant as $\delta = 10^{-3}$ for SSDM in this thesis, which was enough to provide numerical stability for all investigated problems.

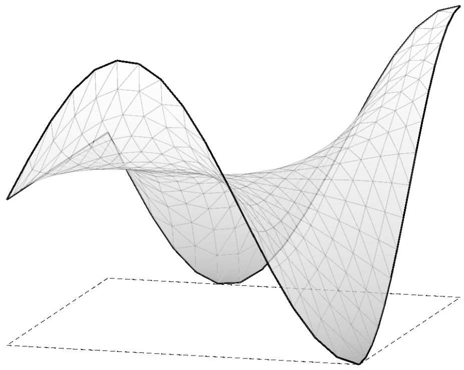

Figure 29. *A minimum surface discretized by triangular elements, form found with SSDM. The boundary lines (thick) are derived from the surface equation* $f(x_f, y_f) = c_1\, sin(c_2 x + \frac{\pi}{2})\, c_3 sin\,(c_4 y - \frac{\pi}{2})$.

3.3.3.2 Constraints on material stiffness

Starting from the Natural Force Density Method (NFDM), the force density is defined as [38]

$$\boldsymbol{q}_t = At\boldsymbol{H}^{-T}\boldsymbol{\sigma} \tag{56}$$

By imposing the constitutive relation $\boldsymbol{\sigma} = \boldsymbol{D}\boldsymbol{\epsilon}$ (Hooke's law) [47], the force density for elastic membranes can instead be written

$$\boldsymbol{q}_{t,u} = At\boldsymbol{H}^{-T}\boldsymbol{D}\boldsymbol{\epsilon} \tag{57}$$

The strains and constitutive matrix for a linear elastic membrane is defined [40]

$$\boldsymbol{\epsilon} = [\epsilon_{\bar{x}} \quad \epsilon_{\bar{y}} \quad \epsilon_{\overline{xy}}]^T \tag{58}$$

$$\boldsymbol{D} = \frac{E}{1-v^2}\begin{bmatrix} 1 & v & 0 \\ v & 1 & 0 \\ 0 & 0 & \dfrac{1-v}{2} \end{bmatrix} \tag{59}$$

Using the matrix $\boldsymbol{\psi}$ from Equation (40), the Cartesian strains can be written as functions of the natural strains [7]:

$$\boldsymbol{\epsilon} = \boldsymbol{\psi}^{-1}\boldsymbol{e} = \frac{1}{2}\boldsymbol{H}^{-1}(\boldsymbol{L}\boldsymbol{l} - \boldsymbol{L}_u\boldsymbol{l}_u) \tag{60}$$

$\boldsymbol{L}$ and $\boldsymbol{l}$ are the current lengths on diagonal matrix form and vector form respectively, and $\boldsymbol{L}_u, \boldsymbol{l}_u$ denotes unstrained lengths in accordance with definitions given in cable network form finding. The force density for membranes can thus be stated as

$$\boldsymbol{q}_{t,u} = \frac{1}{2}At\boldsymbol{H}^{-T}\boldsymbol{D}\boldsymbol{H}^{-1}(\boldsymbol{L}\boldsymbol{l} - \boldsymbol{L}_u\boldsymbol{l}_u) \tag{61}$$

Note that the unit is force/length even though the expression depends on membrane stresses. This is conveniently arranged when analyzing a structure with combined cable and membrane elements. In order to find an elastically deformed shape in equilibrium, a step in coordinate positions need to be defined using Newton-Raphson's Method. The stiffness matrix is established through differentiation of the force density and node distances with respect to global coordinates (again, derivatives with respect to $\boldsymbol{y}$ and $\boldsymbol{z}$ are equivalent) [7]:

$$\frac{\partial \boldsymbol{q}_{t,u}}{\partial \boldsymbol{x}} = \frac{1}{2}At\boldsymbol{H}^{-T}\boldsymbol{H}^{-1}\frac{\partial \boldsymbol{L}\boldsymbol{l} - \boldsymbol{L}_u\boldsymbol{l}_u}{\partial \boldsymbol{x}} = At\boldsymbol{H}^{-T}\boldsymbol{D}\boldsymbol{H}^{-1}\boldsymbol{U}^T\boldsymbol{C}_N \tag{62}$$

The node distance derivatives have already been derived in the previous section (3.3.3.1). Remembering the geometric stiffness matrix definition, the explicit formulation becomes (with respect to $\boldsymbol{x}$):

$$\boldsymbol{G}_{x,u} = \boldsymbol{C}_N^T\boldsymbol{Q}\frac{\partial \boldsymbol{u}}{\partial \boldsymbol{x}} + \boldsymbol{C}_N^T\boldsymbol{U}\frac{\partial \boldsymbol{q}_{t,u}}{\partial \boldsymbol{x}} = \boldsymbol{C}_N^T\boldsymbol{Q}\boldsymbol{C}_N + \; At\boldsymbol{C}_N^T\boldsymbol{U}\boldsymbol{H}^{-T}\boldsymbol{D}\boldsymbol{H}^{-1}\boldsymbol{U}^T\boldsymbol{C}_N \tag{63}$$

There is a non-linear part of the geometrical stiffness matrix (derived in [7]) that has been left out. This choice is expected to have a negative impact on convergence rate (it might however improve numerical stability). Unfortunately, it had to be left out due to the given time frame. It is stated below for possible future implementation:

$$\boldsymbol{G}_{u,nl} = -At\boldsymbol{C}_N^T\underline{\boldsymbol{U}}\boldsymbol{H}^{-T}\boldsymbol{\sigma}\boldsymbol{\sigma}_0^T\boldsymbol{H}^{-1}\underline{\boldsymbol{U}}^T\boldsymbol{C}_N + \frac{t}{4A}At\boldsymbol{C}_N^T\underline{\boldsymbol{U}}\boldsymbol{N}\boldsymbol{U}^{*T}\boldsymbol{\lambda}\boldsymbol{S}\boldsymbol{C}_N \tag{64}$$

$\underline{\boldsymbol{U}} = [\boldsymbol{U} \quad \boldsymbol{V} \quad \boldsymbol{W}]^T$ is a block matrix containing node distances for $\boldsymbol{x}, \boldsymbol{y}$ and $\boldsymbol{z}$ together in contrast to earlier use with respect to $\boldsymbol{x}$ only. $\boldsymbol{U}^*$ is a block matrix defined in local coordinates, and $\boldsymbol{S}$ is the stress tensor. $\boldsymbol{\lambda}$ refers to the transformation matrix between local element coordinates and global coordinates which is explained in section 3.4.1.4.

Damping has been added to increase numerical stability. The step in coordinates is defined on the same modified form as was done for minimum surfaces:

$$\Delta \boldsymbol{x} = (\boldsymbol{G}_{x,s} + \delta \boldsymbol{I})^{-\mathbf{1}} \boldsymbol{r} \tag{65}$$

The developed damping approach is inspired by Gerschgorin's theorem (theorem derived in [48]) as a simple way to determine positive definiteness without having to explicitly calculate the eigenvalues. The damping factor is added to the diagonal of the stiffness matrix to solve the problem with inverting ill conditioned matrices. By making the diagonal entries larger than the sum of absolute values in each row, the matrix is guaranteed to be positive definite. As a consequence, the numerical stability drastically improves. The developed approach is efficient enough to solve all tested non-linear problems that previously diverged. In literature, the numerical stability of FDM with constraints on the material stiffness is sometimes mentioned as a rather slow method, less robust than its equivalents, i.e. dynamic relaxation [7]. With the suggested approach, this obstacle can now be overcome for many problems. However, the efficiency of the damping technique is reduced with increasing number of elements, and convergence can still be slow at times.

3.3.3.3 Convergence criteria

The residuals are calculated as the difference between inner and outer forces for all constraints with Equation (46). Error is calculated as

$$e = \|\boldsymbol{g}\| = \sqrt{g_1^2 + g_2^2 \cdots + g_n^2} \tag{66}$$

With convergence criteria that $e \leq \text{tol}$. Tolerance was set to 10^{-3} for material constraints and 10^{-4} for minimum surfaces.

REMARK: With respect to minimum surfaces, the error is sometimes based on surface area instead of difference between inner (function of node positions) and outer forces. After comparison between error based on area and node coordinates, the error in node coordinates were always governing. Therefore, this has been used for all problems.

3.3.4 Sagging (local deformations)

Sagging is a local deformation, normally due to differences in prestressing between membranes and cables. There is often also a considerable difference in material strength between the cable net and chosen fabric which will lead to larger deformations of the fabric. The visual result is a pillow effect or sagging effect that influences esthetics, but also adds to the load from dead-weight which needs to be considered in analysis. There is also a possible second order instability effect from such a geometry that remains outside the scoop of this text.

3.3.4.1 Combined form finding

Sagging can be determined with FDM/NFDM through non-linear form finding with respect to material deformations. In section 3.2.3.2, the residual function for cable form finding is defined as $\boldsymbol{g}^*(\boldsymbol{q})$. To simplify the calculation, it is beneficial to express the residual function for cables and membranes on the same form. Combined form finding with material constraints is therefore given as functions of node coordinates explicitly, since triangular elements are already given on this form. The additional terms for cables are given below.

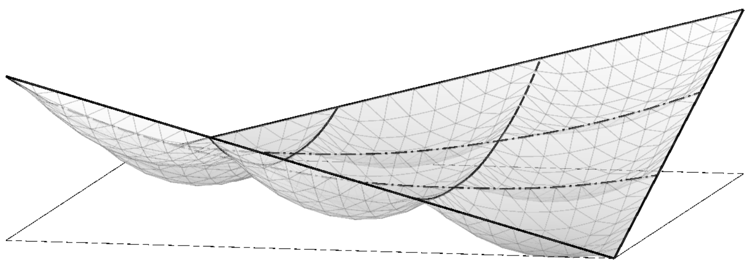

Figure 30. *A hypar with cable and membrane elements, form found with constraints on material stiffness using FDM/NFDM.*

The branch-node matrix is readily formulated on stacked form to easily distinguish between cable and membrane elements [7]:

$$\boldsymbol{C} = \begin{bmatrix} \boldsymbol{C}_{N,b} & \boldsymbol{C}_{F,b} \\ \boldsymbol{C}_{N,t} & \boldsymbol{C}_{F,t} \end{bmatrix} \tag{67}$$

b denotes branches (line elements) and t triangular elements. Force density and element length vectors are arranged in the same order:

$$\boldsymbol{q} = [\boldsymbol{q}_b \ \boldsymbol{q}_t]^T \tag{68}$$
$$\boldsymbol{l} = [\boldsymbol{l}_b \ \boldsymbol{l}_t]^T \tag{69}$$

The combined geometrical stiffness matrix will take the form

$$\boldsymbol{G}_{x,u} = \boldsymbol{C}_N^T \boldsymbol{Q} \boldsymbol{C}_N + \boldsymbol{C}_{N,b}^T \boldsymbol{U} \boldsymbol{L}_{u,b}^{-1} \boldsymbol{L}_b^{-1} EA \boldsymbol{L}_{u,b}^{-1} \boldsymbol{U}^T \boldsymbol{C}_{N,b} + At \boldsymbol{C}_{N,t}^T \boldsymbol{U} \boldsymbol{H}^{-T} \boldsymbol{D} \boldsymbol{H}^{-1} \boldsymbol{U}^T \boldsymbol{C}_{N,t} \tag{70}$$

For simplicity, only the linear part of the stiffness matrix is stated here. The non-linear part concerning triangular elements was already stated in 3.3.3.2. The non-linear part for cable elements reads ([7]) :

$$G_{x,u,b,nl} = \boldsymbol{C}_{N,b}^{T}\boldsymbol{U}\boldsymbol{L}_b^{-1}\boldsymbol{Q}_b\boldsymbol{L}_b^{-1}\boldsymbol{U}^T\boldsymbol{C}_{N,b} \tag{71}$$

This non-linear part of the stiffness matrix has been dropped with the same motivation as in section 3.3.3.2, but is mentioned for completeness.

3.3.5 Flattening and patterning

The concept of patterning is to divide an arbitrary surface into smaller patches. In the context of membranes, the patterning process is often necessary to avoid wrinkles in a prestressed fabric. In addition, the patterning lines will affect the stress distribution to some extent [49]. In the case of minimum surfaces, the only practical way to achieve constant stress distribution is through a patterning procedure. Normally, geodesics are considered as suitable cutting lines, since this reduces the amount of material waste to patch and cover a curved surface [27].

There exists a few methods in the area of surface flattening. The methods could be roughly divided into two categories. The main difference is the restrictions on the mapping. For classic paper folding problems, the surface must be fully developable without distortion, meaning that no deformation is allowed when mapping the flat sheet on the curved discretized surface. The other category allows for some deformations, which is often more practical and less restricting, especially in the context of fabrics [50]. This is a fairly new subject of research, except the traditional problem in cartography, where the problem is reduced to a special case based on the spherical surface [51]. This type of surface is readily described with spherical coordinates and thus easily transformed to a plane. For the general case however, the problem becomes less trivial. Due to time constraints, a simplified method has been developed which is described in steps below.

Proposed flattening procedure:

1) A suitable patch is extracted from the global surface geometry. This can be guided by cable lines for esthetic reasons, or by geodesic lines over the surface to minimize waste of fabric material [27].
2) The topology is reduced to a local problem with only the remaining nodes and elements that are part of the patch.
3) A centerline is identified, preferably along a current cable line in order to reuse established membrane discretization.

4) The centerline is unfolded in longitudinal direction with preserved transversal vector components, placed on the target flattening plane. The patch is then flattened in transversal direction, with preserved longitudinal vector components.
5) Error is estimated by comparing curved and flattened surface area.
6) If the error is above the tolerance, a membrane form finding is performed with constraints on material stiffness (see section 3.3.3.2). The centerline is fixed in space and all free nodes are then pulled away (with a small arbitrary force) in the normal direction from that line, resembling what would happen if the fabric patch was taken from the surface and stretched out as a sheet.
7) Surface area of the doubly curved patch and the flattened patch is compared to evaluate the error. A high error indicates that wrinkling will take place when the patched fabric is mounted, i.e. poor fitting. A smaller patch is then recommended to be extracted, starting again from step 1 in an iterative manner. If this does not help, patches might need to be extracted from geodesics instead of cable lines.

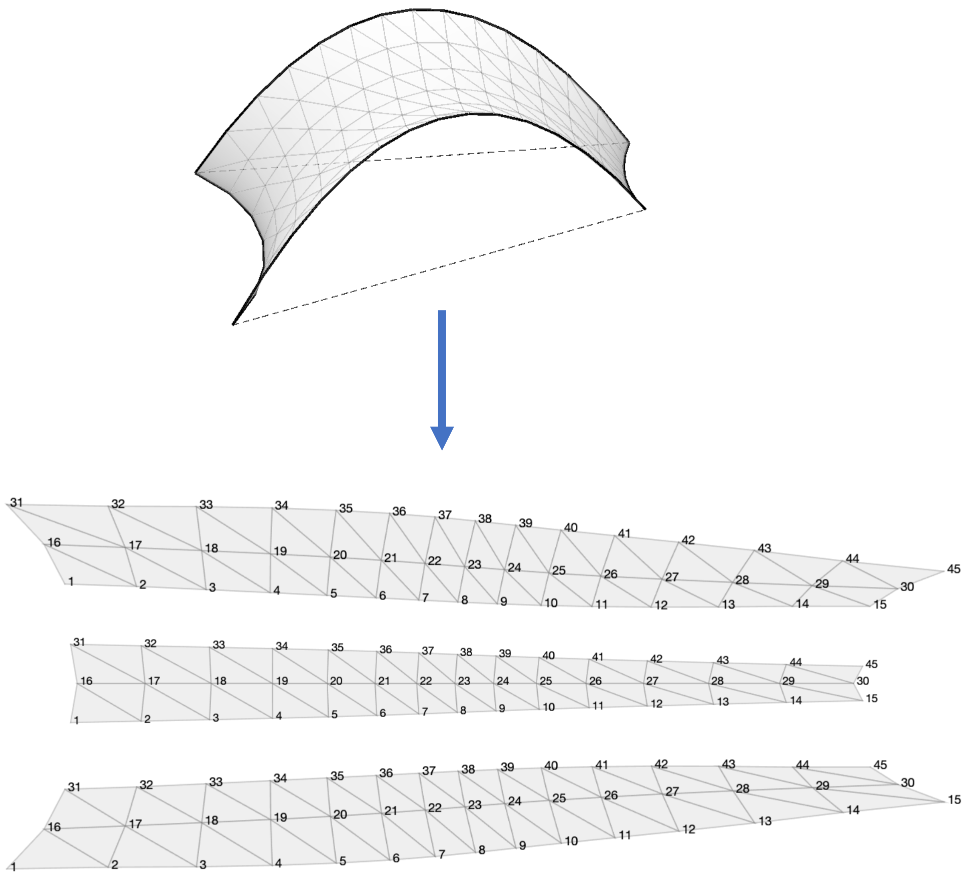

Figure 31. *A doubly curved surface subject to patterning (Patches are not displayed in exactly the same scale).*

3.3.6 Verification

Membrane analysis has been benchmarked through a convergence study based on area (SSDM), as well as form finding a commonly used reference surface. Elastic deformations (NFDM) has been verified through a comparison between a plate subject to unidirectional in-plane loading and an equivalently loaded membrane. The deformed geometry is compared. Flattening is evaluated empirically in the case study (chapter 4).

3.3.6.1 Minimization of surfaces (SSDM)

The implementation of SSDM was evaluated by minimizing a few reference surfaces. The surface in **Figure 32** is known as a pseudo-Scherk's first surface, commonly used for verification purposes in literature about form finding ([40], [7] and [39]). The sum of area was reduced from 12 m^2 after 1 iteration, to 9.89 m^2 in 22 iterations. The change in area was then < 0.001 m^2 between iterations, with norm of residual forces being 2.3583e-4. Side dimensions are 2 x 2 x 2 m with a mesh of 1536 triangular elements. Fixed part of boundary is represented by thick lines. The mean position in z converges towards 1 m (height/2).

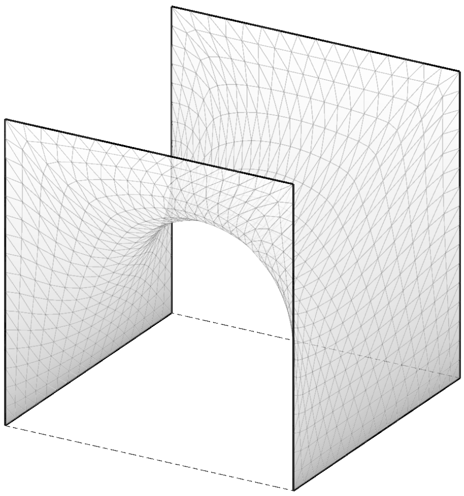

Figure 32. *Form finding of a membrane, using the Surface Stress Density Method.*

In **Figure 33** and **Table 2** two different mesh configurations are compared in the form finding of a minimized hypar surface, using SSDM. Both configurations where iterated 50 times through a fixed point iteration procedure in the early development process (the final version is based on Newton's method).

Results in **Table 2** suggests that the minimization of surface area is independent of mesh orientation while remainder of $\Delta\mathbf{z} = \boldsymbol{K}^{-1}\left(\boldsymbol{P} - \boldsymbol{C}_n^T\boldsymbol{Q}\boldsymbol{C}\boldsymbol{z}\right)$ in the fixed point iteration suggests that Mesh A has a smaller residual between inner and outer forces. For course meshes on a hypar, the geometry is therefore sensitive to element orientation. For finer meshes, both converge towards the same geometry. The reference mesh was added to verify that the number of elements have indeed also an influence on the minimum sum of area, with about 0.65 % lower total surface area after the same amount of iterations.

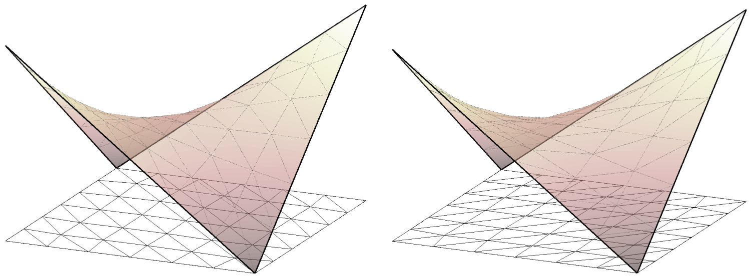

Figure 33. *Two hypars with different mesh orientation.*

Table 2. *Comparison of different mesh performance with respect to minimized surface area and remaining step length using a fixed point iteration.*

	# elements	sum(A)	norm(Δz)
Mesh A (left)	72	10.584229	0.000132
Mesh B (right)	72	10.584212	0.000642
Mesh 1 (reference)	1152	10.515733	0.000894

3.3.6.2 Elastically deformed surfaces (NFDM)

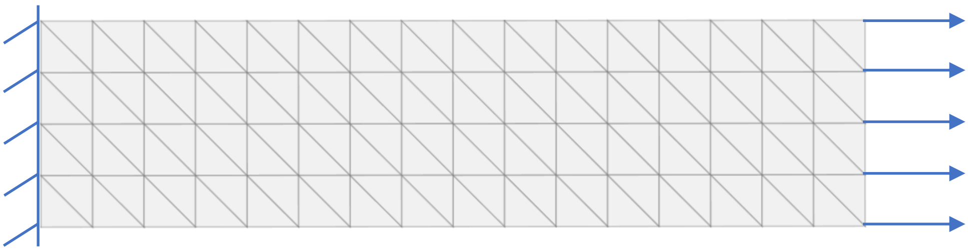

Figure 34. *Boundary conditions and load positions in a unidirectional load test.*

A membrane is subject to unidirectional load in the plane. The mean deflections (in x-direction) of the rightmost nodes are compared between NFDM and FEM solution using CST elements. This should produce rather similar results since the elements are the same. Node load are set to 500 N, E = 50 MPa, $\nu = 0.01$ and $t = 0.004$ m. The test strip was set to 2 x 0.5 m.

Table 3. *Comparison of mean deflection at the rightmost node line for a 2 m long strip in unidirectional loading.*

	NFDM [mm]	FEM (CST element) [mm]
Mean deflection (x-dir)	51.0	50.4

As seen in **Table 3**, the deflections are comparable with good coherence. The tolerance for convergence with NFDM was set to 10^{-4}.

3.3.7 Conclusion

- NFDM is a linear extension for membranes, close to identical with the original FDM formulation. NFDM can be used with various constraints much like FDM, even minimization of surfaces. In this thesis, material stiffness constraints has been successfully implemented, while SSDM was instead used for minimization of surfaces.

- Cholesky decomposition for NFDM with material constraint was found slower than using a sparse matrix formulation. However, the comparison was only done for two different problems and might not hold in general.

- Damping approach inspired by Gerschgorin's Theorem has been developed for NFDM as a way to guarantee positive definiteness. Thus, numerical stability is achieved with the material stiffness constraint for all tested problems.

- The simplified flattening approach (linear unfolding) resulted in poor fitting in the empirical evaluation. This might or might not be due to inaccuracies of the method, which has not been properly confirmed. This needs further study. The proposed form finding approach has shown more promising results in early investigations.

- With SSDM, changing mesh orientation does not seem to affect the sum of area but there is a clear relation between mesh orientation and error in the node position. This error decreases with increased number of elements.

- SSDM can most likely be used in the context of optimizing node connections in a space truss network. This application can use the Schwartz P surface (surface discussed briefly in [42]) as a starting point, and by positioning cutouts (topology) for the connecting branches on individual planes, together forming a polyhedral, the 3D surface geometry can be form found to a minimized surface, thus optimizing the connection with respect to membrane stresses.

3.4 Shell analysis

To properly inform the design process, some feedback on structural behavior of the shell is needed. To make this fully integrated and accessible, a FE solver has been developed based on Kirchhoff's plate theory. Kirchhoff's plate theory is essentially formulated as a decoupled problem for membranes and plates respectively [47], resulting in the differential equations

$$-\widetilde{\nabla}^T \boldsymbol{D}^0 \widetilde{\nabla} \boldsymbol{u}^0 = \boldsymbol{b} \quad \text{on } \Omega \tag{72}$$

$$\acute{\nabla}^T \widetilde{\boldsymbol{D}} \acute{\nabla} w = q \quad \text{on } \Omega \tag{73}$$

Differential operators for two-dimensional elasticity are defined as

$$\widetilde{\nabla} = \begin{bmatrix} \frac{\partial}{\partial x} & 0 & \frac{\partial}{\partial y} \\ 0 & \frac{\partial}{\partial y} & \frac{\partial}{\partial x} \end{bmatrix}^T \tag{74}$$

$$\acute{\nabla} = \begin{bmatrix} \frac{\partial^2}{\partial x^2} & \frac{\partial^2}{\partial y^2} & 2\frac{\partial^2}{\partial x \partial y} \end{bmatrix}^T \tag{75}$$

The main quantities are defined in **Figure 35**, where $\boldsymbol{b}$ denotes in plane body loads with deflections $\boldsymbol{u}$. q denotes out of plane loading with out of plane deflection w. The Finite Element implementation of the Kirchoff's plate theory can be found in any book on the subject. Therefore, derivations in this chapter are kept brief and on general form. For more information, the reader is referred to [47] or [52].

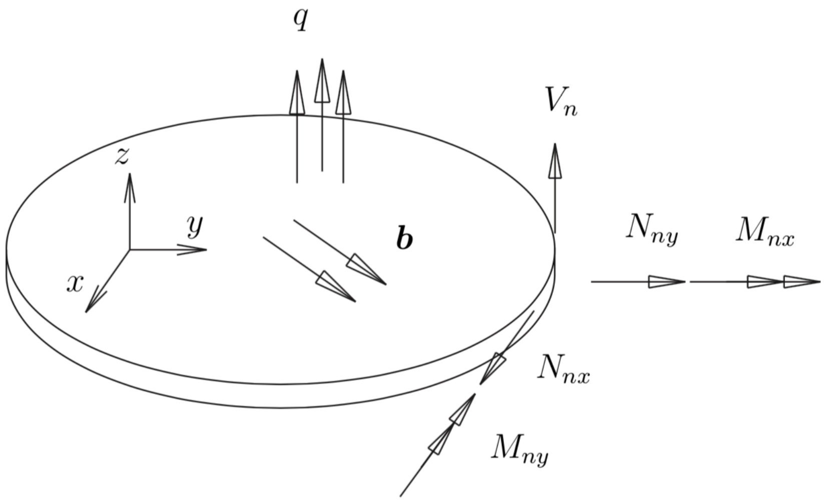

Figure 35. Quantities of the differential equation for shells [36].

3.4.1 FE formulation

The FE formulation for plates are stated on general form through use of Galerkin's method with the displacement vector approximated as $w = \boldsymbol{N}(x,y)\boldsymbol{a}_b$ $(\acute{\nabla} w = \acute{\boldsymbol{B}}(x,y)\boldsymbol{a}_b)$ and arbitrary test function $\delta w = \boldsymbol{N}(x,y)\delta\boldsymbol{a}_b$ $(\acute{\nabla}\delta w = \acute{\boldsymbol{B}}(x,y)\delta\boldsymbol{a}_b)$ [47]:

$$\int_\Omega \acute{\boldsymbol{B}}^T \widetilde{\boldsymbol{D}_b} \acute{\boldsymbol{B}}\, d\Omega\ \mathbf{a} = \int_\Omega \boldsymbol{N}^T q\ d\Omega + \int_{\Gamma_{h,\mathrm{I}}} \boldsymbol{N}^T h_{\mathrm{I}}\ d\Gamma - \int_{\Gamma_{h,\mathrm{II}}} \boldsymbol{B}^T \boldsymbol{n} h_{\mathrm{II}}\ d\Gamma + \\ + \int_{\Gamma_{g,\mathrm{I}}} \boldsymbol{N}^T V_n^K\ d\Gamma - \int_{\Gamma_{g,\mathrm{II}}} \boldsymbol{B}^T \boldsymbol{n} M_{nn}\ d\Gamma \tag{76}$$

Neumann and Dirichlet conditions can be seen in **Figure 36**, stated on Γ_{I} and Γ_{II} for the plate formulation. Note that the reaction force terms on $\Gamma_{g,\mathrm{I}}$ and $\Gamma_{g,\mathrm{II}}$, are belonging to translation and rotations respectively.

For the decoupled problem, the FE formulation for membranes can be written on the following general form with the approximations $\boldsymbol{u} = \boldsymbol{N}(x,y)\boldsymbol{a}_m$ $(\widetilde{\nabla}\boldsymbol{u} = \boldsymbol{B}(x,y)\boldsymbol{a}_m)$ and arbitrary test function $\delta\boldsymbol{u} =\ \boldsymbol{N}(x,y)\delta\boldsymbol{a}_m$ $(\widetilde{\nabla}\delta\boldsymbol{u} = \boldsymbol{B}(x,y)\delta\boldsymbol{a}_m)$:

$$\int_\Omega \boldsymbol{B}^T \boldsymbol{D}_m \boldsymbol{B}\, d\Omega\ \mathbf{a} = \int_\Omega \boldsymbol{B}^T \boldsymbol{D}_m \boldsymbol{\varepsilon}_0\ d\Omega + \int_\Omega \boldsymbol{N}^T \boldsymbol{b}\ d\Omega + \int_{\Gamma_h} \boldsymbol{N}^T h\ d\Gamma + \int_{\Gamma_g} \boldsymbol{N}^T \boldsymbol{t}\ d\Gamma \tag{77}$$

The first term on the RHS is only non-zero if there is any prestressing imposed on the structure. This could arise from prestressed reinforcement, or possibly, if one wants to introduce forces due to drying shrinkage or thermal loading. The term on Γ_g is reaction forces due to prescribed in-plane translations.

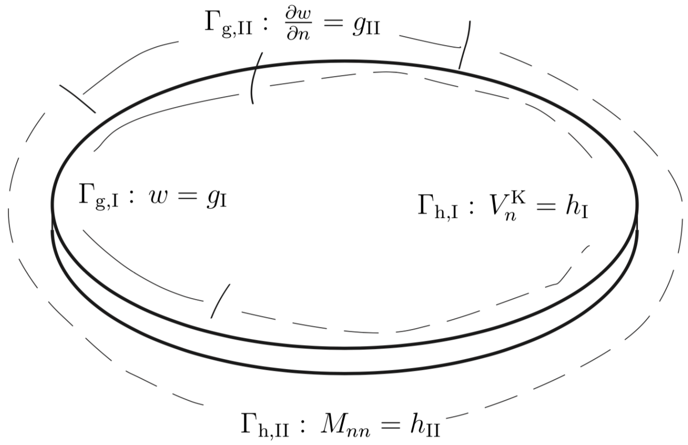

Figure 36. *Boundary conditions for the Kirchhoff plate, shown on separated boundary lines g for Dirichlet and h for Neumann conditions [36].*

For the current implementation, these two FE formulations will be merged together (stacking degrees of freedom by assembling the stiffness matrix and force vector accordingly) to solve the global system

$$\boldsymbol{K}\boldsymbol{a} = \boldsymbol{f} \tag{78}$$

REMARK: Matrices and vectors will be explicitly stated in section 3.4.1.2 - 3.4.1.3 below.

3.4.1.1 Discretization

A literature study has been performed with the purpose of finding an efficient and reliable element for thin shell analysis. The Discrete Kirchhoff Theory (DKT) plate element is concluded as a suitable choice with respect to these demands [53]. The formulation is a three-node plate element, effectively transferring rotations along the element sides to the nodes [54]. The choice of a triangular element is also motivated by preservation of planarity, reduced number of integration points for in-plane stiffness (constant strain), and simplicity in formulation while still being accurate. The DKT element is also implemented in commercial software such as Abaqus [55], further suggesting that it is a competitive choice.

A shell element is derived by using the classical Constant Strain Triangle (CST) element formulation for in plane degrees of freedom (dof), and the DKT plate element for rotational degrees of freedom and out of plane translation [54]. Together, these two elements form a shell element with 15 degrees of freedom in local plane coordinates, or 18 in global coordinates if drilling degrees of freedom are considered [52].

3.4.1.2 DKT element

The DKT concept arrives at a 9 dof bending element by first introducing the Kirchhoff hypothesis along the element edges as a way of connecting the rotations to the transverse displacements. Such an approach makes the elements converge towards the classical plate solution [53]. Under the assumption of small deformations, bending and transverse shear strains are defined as $\boldsymbol{\varepsilon}_b = z\boldsymbol{\kappa}$ and $\boldsymbol{\gamma} = [\begin{smallmatrix} \frac{\partial w}{\partial x} + \beta_x \\ \frac{\partial w}{\partial y} + \beta_y \end{smallmatrix}]$ respectively, with the curvature $\boldsymbol{\kappa} = \left[\frac{\partial \beta_x}{\partial x} \quad \frac{\partial \beta_y}{\partial y} \quad \frac{\partial \beta_x}{\partial y} + \frac{\partial \beta_y}{\partial x}\right]^T$, with β_x being the rotation of the normal to the undeformed middle surface in x-z plane, and β_y corresponding to the y-z plane. For an isotropic plate, the constitutive relations for bending and shear becomes

$$\boldsymbol{D}_b = \frac{Et^3}{12(1-v^2)}\begin{bmatrix}1 & v & 0\\ v & 1 & 0\\ 0 & 0 & \dfrac{1-v}{2}\end{bmatrix} \tag{79}$$

$$\boldsymbol{D}_s = \frac{Etk}{2(1+v)}\begin{bmatrix}1 & 0\\ 0 & 1\end{bmatrix} \tag{80}$$

With E being Young's modulus and v Poission's ratio, and $k = \frac{5}{6}$. Through basic definitions, the expressions for bending and shear forces can thus be stated as

$$\boldsymbol{M} = \begin{bmatrix}M_x\\ M_y\\ M_{xy}\end{bmatrix} = \int_{-\frac{t}{2}}^{\frac{t}{2}} z\boldsymbol{\sigma}\,dz = \boldsymbol{D}_b\boldsymbol{\kappa} \tag{81}$$

$$\boldsymbol{V} = \begin{bmatrix}V_x\\ V_y\end{bmatrix} = \boldsymbol{k}\int_{-\frac{t}{2}}^{\frac{t}{2}} \boldsymbol{\sigma}_s\,dz\boldsymbol{k} = \boldsymbol{D}_s\boldsymbol{\gamma} \tag{82}$$

with $\boldsymbol{k}$ containing shear correction factors. For a thin plate, the transverse shear strains are almost non-existent in comparison to strains from bending, thus the shear stiffness becomes negligible. Therefore, only the bending part will be considered in the continuation of deriving the element stiffness matrix. To arrive at dofs defined at the nodes, a geometrical relation to the rotations along the element edges first needs to be defined, using direction cosines

$$\begin{bmatrix}\beta_x\\ \beta_y\end{bmatrix} = \begin{bmatrix}\cos(x, n_{ij}) & -\sin(x, n_{ij})\\ \sin(x, n_{ij}) & \cos(x, n_{ij})\end{bmatrix}\begin{bmatrix}\beta_n\\ \beta_s\end{bmatrix} \tag{83}$$

β_s and β_n are rotations described parallel and normal to each of the triangle sides. By acknowledging that β_x and β_y have a quadratic variation over the element (w varies cubically along the element sides), the rotations are redefined by introducing them in terms of the shape functions and nodal dofs $\boldsymbol{U}^T = [w_1\ \theta_{x1}\ \theta_{y1}\ w_2\ \theta_{x2}\ \theta_{y2}\ w_3\ \theta_{x3}\ \theta_{y3}]$, using the geometrical relation stated above [53]:

$$\beta_x = \boldsymbol{H}_x^T(\xi, \eta)\boldsymbol{U} \tag{84}$$

$$\beta_y = \boldsymbol{H}_y^T(\xi, \eta)\boldsymbol{U} \tag{85}$$

$\boldsymbol{H}_x$ and $\boldsymbol{H}_y$ are vectors containing the shape functions. Their explicit formulation is left out for brevity since they are not directly used in implementation (for explicit formulations, see [53] or [54]), and will instead be stated implicitly through their derivates ($\boldsymbol{H}_{x\xi}, \boldsymbol{H}_{x\eta}$ and $\boldsymbol{H}_{y\xi}, \boldsymbol{H}_{y\eta}$) which are used to derive the stiffness matrix and element forces. While the shape functions are conveniently described and integrated in the parent domain as functions $N_i(\xi, \eta)$, a transformation is needed for the general formulation of an element in the $x(\xi, \eta)$ - $y(\xi, \eta)$ plane [54]. The Jacobian is used to relate the parent and local plane domain (with similar expression with respect to y):

$$\begin{bmatrix} \boldsymbol{H}_{xx}^T \\ \boldsymbol{H}_{xy}^T \end{bmatrix} = J^{-1} \begin{bmatrix} \boldsymbol{H}_{x\xi}^T \\ \boldsymbol{H}_{x\eta}^T \end{bmatrix} = \frac{1}{2A} \begin{bmatrix} y_{31} & y_{12} \\ -x_{31} & -x_{12} \end{bmatrix} \begin{bmatrix} \boldsymbol{H}_{x\xi}^T \\ \boldsymbol{H}_{x\eta}^T \end{bmatrix} \tag{86}$$

with $2A = x_{31}y_{12} - x_{12}y_{31}$. $\boldsymbol{H}_{x\xi}$ and $\boldsymbol{H}_{x\eta}$ denotes the derivates of shape function vectors with respect to ξ and η, which are given explicitly as [53]

$$\boldsymbol{H}_{x\xi} = \begin{bmatrix} P_6(1-2\xi) + (P_5 - P_6)\eta \\ q_6(1-2\xi) - (q_5 + q_6)\eta \\ -4 + 6(\xi+\eta) + r_6(1-2\xi) - \eta(r_5 + r_6) \\ -P_6(1-2\xi) + \eta(P_4 + P_6) \\ q_6(1-2\xi) - \eta(q_6 - q_4) \\ -2 + 6\xi + r_6(1-2\xi) + \eta(r_4 - r_6) \\ -\eta(P_5 + P_4) \\ \eta(q_4 - q_5) \\ -\eta(r_5 - r_4) \end{bmatrix} \tag{87}$$

$$\boldsymbol{H}_{x\eta} = \begin{bmatrix} -P_5(1-2\eta) - \xi(P_6 - P_5) \\ q_5(1-2\eta) - \xi(q_5 + q_6) \\ -4 + 6(\xi+\eta) + r_5(1-2\eta) - \xi(r_5 + r_6) \\ \xi(P_4 + P_6) \\ \xi(q_4 - q_6) \\ -\xi(r_6 - r_4) \\ P_5(1-2\eta) - \xi(P_4 + P_5) \\ q_5(1-2\eta) + \xi(q_4 - q_5) \\ -2 + 6\eta + r_5(1-2\eta) + \xi(r_4 - r_5) \end{bmatrix} \tag{88}$$

and with $\boldsymbol{H}_y(\xi, \eta)$, the shape function (gathered on vector form) derivatives becomes

$$
\boldsymbol{H}_{y\xi} = \begin{bmatrix} t_6(1-2\xi)+\eta(t_5-t_6) \\ 1+r_6(1-2\xi)-\eta(r_5+r_6) \\ -q_6(1-2\xi)+\eta(q_5+q_6) \\ -t_6(1-2\xi)+\eta(t_4+t_6) \\ -1+r_6(1-2\xi)+\eta(r_4-r_6) \\ -q_6(1-2\xi)-\eta(q_4-q_6) \\ -\eta(t_4+t_5) \\ \eta(r_4-r_5) \\ -\eta(q_4-q_5) \end{bmatrix} \tag{89}
$$

$$
\boldsymbol{H}_{y\eta} = \begin{bmatrix} -t_5(1-2\eta)-\xi(t_6-t_5) \\ 1+r_5(1-2\eta)-\xi(r_5+r_6) \\ -q_5(1-2\eta)+\xi(q_5+q_6) \\ \xi(t_4+t_6) \\ \xi(r_4-r_6) \\ -\xi(q_4-q_6) \\ t_5(1-2\eta)-\xi(t_4+t_5) \\ -1+r_5(1-2\eta)+\xi(r_4-r_5) \\ -q_5(1-2\eta)-\xi(q_4-q_5) \end{bmatrix} \tag{90}
$$

The constants can to a large part be identified as the direction cosines defined as ($k =$ 4,5,6 for $ij =$ 23,31,12 respectively):

$$
P_k = -\tfrac{6x_{ij}}{l_{ij}^2} \qquad q_k = \tfrac{3x_{ij}y_{ij}}{l_{ij}^2} \qquad t_k = -\tfrac{6y_{ij}}{l_{ij}^2} \qquad r_k = \tfrac{3y_{ij}^2}{l_{ij}^2}
$$

The derivatives are then put together in the 'gradient' matrix $\boldsymbol{B}(\xi,\eta)$ which are then used in the final expression of the stiffness matrix for one element:

$$
\boldsymbol{B}(\xi,\eta) = \frac{1}{2A} \begin{bmatrix} y_{31}\boldsymbol{H}_{x\xi}^T + y_{12}\boldsymbol{H}_{x\eta}^T \\ -x_{31}\boldsymbol{H}_{y\xi}^T - x_{12}\boldsymbol{H}_{y\eta}^T \\ -x_{31}\boldsymbol{H}_{x\xi}^T - x_{12}\boldsymbol{H}_{x\eta}^T + y_{31}\boldsymbol{H}_{y\xi}^T + y_{12}\boldsymbol{H}_{y\eta}^T \end{bmatrix} \tag{91}
$$

The stiffness matrix in local coordinates becomes

$$
\boldsymbol{K}_{DKT}(x,y) = 2A \int_0^1 \int_0^{1-\eta} \boldsymbol{B}_b^T(\xi,\eta)\boldsymbol{D}_b\boldsymbol{B}_b(\xi,\eta)\; d\xi\; d\eta \tag{92}
$$

Element forces are then calculated as (with curvature definition $\boldsymbol{\kappa} = \boldsymbol{B}_b(x,y)\boldsymbol{U}$)

$$
\boldsymbol{M}(x,y) = \boldsymbol{D}_b\boldsymbol{B}_b(x,y)\boldsymbol{U} \tag{93}
$$

where $x = x_1 + \xi x_{21} + \eta x_{31}$ and $y = y_1 + \xi y_{21} + \eta y_{31}$ over the element surface. It is here important to realize that $\boldsymbol{M}$ is not unique along the boundary shared by two elements since it depends on all components in $\boldsymbol{U}$ [53].

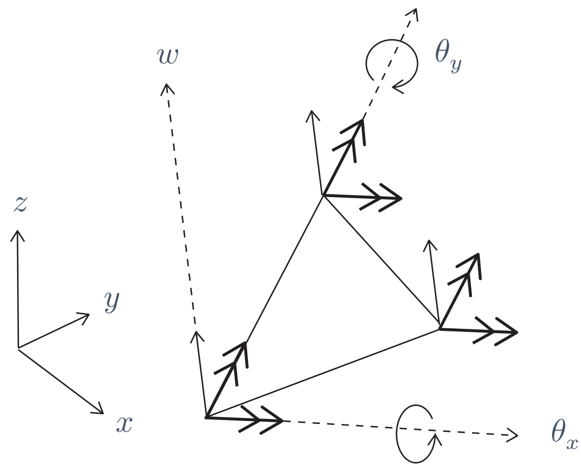

Figure 37. *DKT element displaying rotational degrees of freedom and out of plane translation stated in the triangle nodes.*

3.4.1.3 CST element

The stiffness matrix and element forces belonging to the Constant Strain Element (CST) are somewhat easier to derive due to the linear shape functions. By assuming the well-known approximation of deflections $\boldsymbol{u} = \boldsymbol{N^e a^e}$ [36] where

$$\boldsymbol{u} = \begin{bmatrix} u_x \\ u_y \end{bmatrix} \tag{94}$$

$$\boldsymbol{N}^e = \begin{bmatrix} N_1 & 0 & N_2 & 0 & N_3 & 0 \\ 0 & N_1 & 0 & N_2 & 0 & N_3 \end{bmatrix} \tag{95}$$

$$\boldsymbol{a}^e = \begin{bmatrix} u_{x1} \\ u_{y1} \\ u_{x2} \\ u_{y2} \\ u_{x3} \\ u_{y3} \end{bmatrix} \tag{96}$$

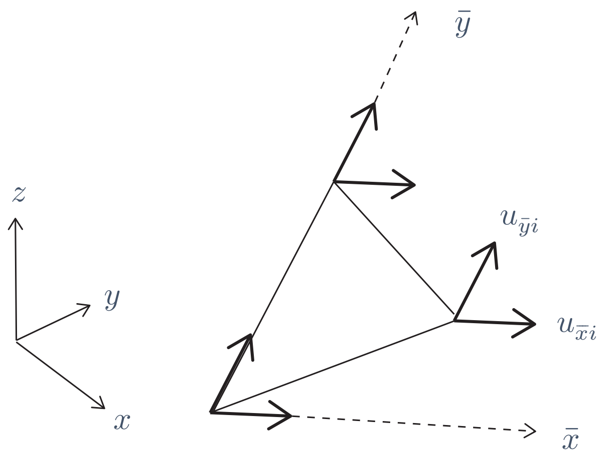

Figure 38. *CST element with in plane translations.*

The linear shape functions can be stated directly as functions of the local coordinates $\bar{x}$ and $\bar{y}$ [47] (the local coordinate notation marks ´$-$´ over coordinates are dropped in further expressions for simplicity):

$$N_1^e = \frac{1}{2A}[x_2y_3 - x_3y_2 + (y_2 - y_3)x + (x_3 - x_2)y] \tag{97}$$

$$N_2^e = \frac{1}{2A}[x_3y_1 - x_1y_3 + (y_3 - y_1)x + (x_1 - x_3)y] \tag{98}$$

$$N_3^e = \frac{1}{2A}[x_1y_2 - x_2y_1 + (y_1 - y_2)x + (x_2 - x_1)y] \tag{99}$$

where the triangle area A has already been defined in derivation of the DKT element. Through the definition $\boldsymbol{B}^e = \widetilde{\nabla}\boldsymbol{N}^e$, the matrix containing the shape function derivatives for one element becomes [52]

$$\boldsymbol{B}^e = \frac{1}{2A}\begin{bmatrix} y_{23} & 0 & y_{31} & 0 & y_{12} & 0 \\ 0 & x_{32} & 0 & x_{13} & 0 & x_{21} \\ x_{32} & y_{23} & x_{13} & y_{31} & x_{21} & y_{12} \end{bmatrix} \tag{100}$$

The constitutive matrix for membrane stresses and strains is [47]

$$\boldsymbol{D}_m = \frac{E}{1-v^2}\begin{bmatrix} 1 & v & 0 \\ v & 1 & 0 \\ 0 & 0 & \dfrac{1-v}{2} \end{bmatrix} \tag{101}$$

The element stiffness matrix is given on the form [25]

$$\boldsymbol{K}_{CST} = \int_A \boldsymbol{B}^e(x,y)\boldsymbol{D}_m\boldsymbol{B}^e(x,y)t\ dA \tag{102}$$

And with the element body load directly from the general FE expression [47]:

$$\boldsymbol{f}_{CST} = \int_A \boldsymbol{N}^{e,T}(x,y)\boldsymbol{b}t\ dA \tag{103}$$

Constant strain elements avoid shear locking and neglects transverse shear deformation. Therefore, it is suitable for describing thin shells [27]. With linear shape functions, the element is also integrated exactly since the Jacobian becomes constant, as mentioned in 3.4.1.5 (no dependence on ξ or η).

3.4.1.4 Transformations

Sometimes, it is convenient to perform calculations on a different set of base vectors. The commonly used transformations in this thesis is between parent and local domain, and from local domain to global domain, as illustrated in

Figure *39*. Transformations between parent and local domain are implemented already in the derivation of stiffness matrices and element forces. The transformation from local to global coordinates is done through the formulation of matrices containing direction cosines for each element side. The transformation can be written on the form [52]

$$\boldsymbol{K}^e(x,y) = \boldsymbol{\lambda}^T\boldsymbol{K}^e(\bar{x},\bar{y})\boldsymbol{\lambda} \tag{104}$$

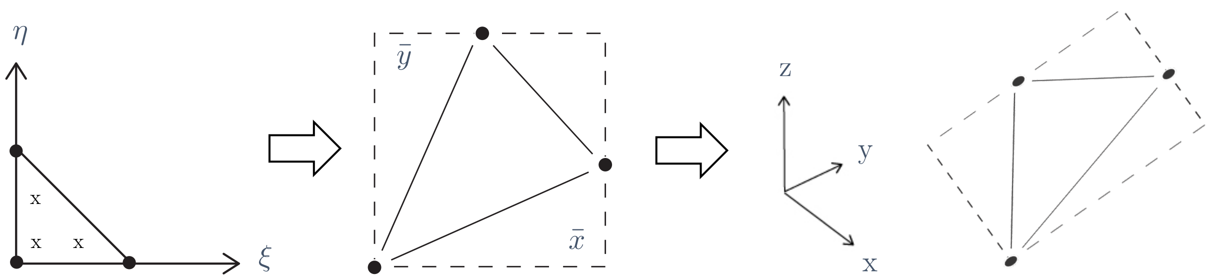

Figure 39. *Transformations between parent, local and global domains.*

With the transformation matrix $\boldsymbol{\lambda}$ (18x18) for all shell degrees of freedom expressed as a block matrix:

$$\boldsymbol{\lambda} = \begin{bmatrix} \bar{\boldsymbol{\lambda}} & \bar{\mathbf{0}} & \bar{\mathbf{0}} & \bar{\mathbf{0}} & \bar{\mathbf{0}} & \bar{\mathbf{0}} \\ \bar{\mathbf{0}} & \bar{\boldsymbol{\lambda}} & \bar{\mathbf{0}} & \bar{\mathbf{0}} & \bar{\mathbf{0}} & \bar{\mathbf{0}} \\ \bar{\mathbf{0}} & \bar{\mathbf{0}} & \bar{\boldsymbol{\lambda}} & \bar{\mathbf{0}} & \bar{\mathbf{0}} & \bar{\mathbf{0}} \\ \bar{\mathbf{0}} & \bar{\mathbf{0}} & \bar{\mathbf{0}} & \bar{\boldsymbol{\lambda}} & \bar{\mathbf{0}} & \bar{\mathbf{0}} \\ \bar{\mathbf{0}} & \bar{\mathbf{0}} & \bar{\mathbf{0}} & \bar{\mathbf{0}} & \bar{\boldsymbol{\lambda}} & \bar{\mathbf{0}} \\ \bar{\mathbf{0}} & \bar{\mathbf{0}} & \bar{\mathbf{0}} & \bar{\mathbf{0}} & \bar{\mathbf{0}} & \bar{\boldsymbol{\lambda}} \end{bmatrix} \tag{105}$$

with

$$\bar{\boldsymbol{\lambda}} = \begin{bmatrix} l_{ox} & m_{ox} & n_{ox} \\ l_{oy} & m_{oy} & n_{oy} \\ l_{oz} & m_{oz} & n_{oz} \end{bmatrix} \tag{106}$$

and

$$\bar{\mathbf{0}} = \begin{bmatrix} 0 & 0 & 0 \\ 0 & 0 & 0 \\ 0 & 0 & 0 \end{bmatrix} \tag{107}$$

Here, (l_{ox}, m_{ox}, n_{ox}), (l_{oy}, m_{oy}, n_{oy}) and (l_{oz}, m_{oz}, n_{oz}) are direction cosines, essentially projections of the local axis on the global axis where the squared sum of projected lengths should always be 1. $l_{ox} = \frac{x_j - x_i}{d_{ij}}$ is an explicit example of the direction cosine formulations, with d_{ij} being the element side length between nodes i and j.

The expanded shell element stiffness matrix in local coordinates consists of the contribution from CST dofs (6x6):

$$K_m^e = \begin{bmatrix} \underset{2\text{ x }2}{\boldsymbol{k}_{11,m}} & \underset{2\text{ x }2}{\boldsymbol{k}_{12,m}} & \underset{2\text{ x }2}{\boldsymbol{k}_{13,m}} \\ \underset{2\text{ x }2}{\boldsymbol{k}_{21,m}} & \underset{2\text{ x }2}{\boldsymbol{k}_{22,m}} & \underset{2\text{ x }2}{\boldsymbol{k}_{23,m}} \\ \underset{2\text{ x }2}{\boldsymbol{k}_{31,m}} & \underset{2\text{ x }2}{\boldsymbol{k}_{32,m}} & \underset{2\text{ x }2}{\boldsymbol{k}_{33,m}} \end{bmatrix} \tag{108}$$

And contributions from DKT dofs (9x9):

$$K_b^e = \begin{bmatrix} \underset{3\text{ x }3}{\boldsymbol{k}_{11,b}} & \underset{3\text{ x }3}{\boldsymbol{k}_{12,b}} & \underset{3\text{ x }3}{\boldsymbol{k}_{13,b}} \\ \underset{3\text{ x }3}{\boldsymbol{k}_{21,b}} & \underset{3\text{ x }3}{\boldsymbol{k}_{22,b}} & \underset{3\text{ x }3}{\boldsymbol{k}_{23,b}} \\ \underset{3\text{ x }3}{\boldsymbol{k}_{31,b}} & \underset{3\text{ x }3}{\boldsymbol{k}_{32,b}} & \underset{3\text{ x }3}{\boldsymbol{k}_{33,b}} \end{bmatrix} \tag{109}$$

The shell element stiffness matrix on expanded form has 18x18 dof if the drilling degrees (θ_{zi}) are included in all nodes. If all elements are still defined in the same plane in space, the stiffness matrix will become singular due to the zero rows, as clearly seen in the expanded matrix below. This is either solved by reducing the system to neglect all drilling degrees of freedom (reducing to 15x15, which is needed when everything is defined in the same plane), or if several groups of elements in sub-planes intersect each other, it might be necessary to either assign a fictive stiffness or prescribe key nodes that cause the singularity [56]. For a doubly curved surface however, this is usually not a problem as the transformation itself will make the stiffness matrix linearly independent.

$$\boldsymbol{K}^e = \begin{bmatrix}
\underset{2\text{ x }2}{\boldsymbol{k}_{11,m}} & \underset{2\text{ x }3}{\mathbf{0}} & \underset{2\text{ x }1}{\mathbf{0}} & \underset{2\text{ x }2}{\boldsymbol{k}_{12,m}} & \underset{2\text{ x }3}{\mathbf{0}} & \underset{2\text{ x }1}{\mathbf{0}} & \underset{2\text{ x }2}{\boldsymbol{k}_{13,m}} & \underset{2\text{ x }3}{\mathbf{0}} & \underset{2\text{ x }1}{\mathbf{0}} \\
\underset{3\text{ x }2}{\mathbf{0}} & \underset{3\text{ x }3}{\boldsymbol{k}_{11,b}} & \underset{3\text{ x }1}{\mathbf{0}} & \underset{3\text{ x }2}{\mathbf{0}} & \underset{3\text{ x }3}{\boldsymbol{k}_{12,b}} & \underset{3\text{ x }1}{\mathbf{0}} & \underset{3\text{ x }2}{\mathbf{0}} & \underset{3\text{ x }3}{\boldsymbol{k}_{13,b}} & \underset{3\text{ x }1}{\mathbf{0}} \\
\underset{1\text{ x }2}{\mathbf{0}} & \underset{1\text{ x }3}{\mathbf{0}} & \underset{1\text{ x }1}{\mathbf{0}} & \underset{1\text{ x }2}{\mathbf{0}} & \underset{1\text{ x }3}{\mathbf{0}} & \underset{1\text{ x }1}{\mathbf{0}} & \underset{1\text{ x }2}{\mathbf{0}} & \underset{1\text{ x }3}{\mathbf{0}} & \underset{1\text{ x }1}{\mathbf{0}} \\
\underset{2\text{ x }2}{\boldsymbol{k}_{21,m}} & \underset{2\text{ x }3}{\mathbf{0}} & \underset{2\text{ x }1}{\mathbf{0}} & \underset{2\text{ x }2}{\boldsymbol{k}_{22,m}} & \underset{2\text{ x }3}{\mathbf{0}} & \underset{2\text{ x }1}{\mathbf{0}} & \underset{2\text{ x }2}{\boldsymbol{k}_{23,m}} & \underset{2\text{ x }3}{\mathbf{0}} & \underset{2\text{ x }1}{\mathbf{0}} \\
\underset{3\text{ x }2}{\mathbf{0}} & \underset{3\text{ x }3}{\boldsymbol{k}_{21,b}} & \underset{3\text{ x }1}{\mathbf{0}} & \underset{3\text{ x }2}{\mathbf{0}} & \underset{3\text{ x }3}{\boldsymbol{k}_{22,b}} & \underset{3\text{ x }1}{\mathbf{0}} & \underset{3\text{ x }2}{\mathbf{0}} & \underset{3\text{ x }3}{\boldsymbol{k}_{23,b}} & \underset{3\text{ x }1}{\mathbf{0}} \\
\underset{1\text{ x }2}{\mathbf{0}} & \underset{1\text{ x }3}{\mathbf{0}} & \underset{1\text{ x }1}{\mathbf{0}} & \underset{1\text{ x }2}{\mathbf{0}} & \underset{1\text{ x }3}{\mathbf{0}} & \underset{1\text{ x }1}{\mathbf{0}} & \underset{1\text{ x }2}{\mathbf{0}} & \underset{1\text{ x }3}{\mathbf{0}} & \underset{1\text{ x }1}{\mathbf{0}} \\
\underset{2\text{ x }2}{\boldsymbol{k}_{31,m}} & \underset{2\text{ x }3}{\mathbf{0}} & \underset{2\text{ x }1}{\mathbf{0}} & \underset{2\text{ x }2}{\boldsymbol{k}_{32,m}} & \underset{2\text{ x }3}{\mathbf{0}} & \underset{2\text{ x }1}{\mathbf{0}} & \underset{2\text{ x }2}{\boldsymbol{k}_{33,m}} & \underset{2\text{ x }3}{\mathbf{0}} & \underset{2\text{ x }1}{\mathbf{0}} \\
\underset{3\text{ x }2}{\mathbf{0}} & \underset{3\text{ x }3}{\boldsymbol{k}_{31,b}} & \underset{3\text{ x }1}{\mathbf{0}} & \underset{3\text{ x }2}{\mathbf{0}} & \underset{3\text{ x }3}{\boldsymbol{k}_{32,b}} & \underset{3\text{ x }1}{\mathbf{0}} & \underset{3\text{ x }2}{\mathbf{0}} & \underset{3\text{ x }3}{\boldsymbol{k}_{33,b}} & \underset{3\text{ x }1}{\mathbf{0}} \\
\underset{1\text{ x }2}{\mathbf{0}} & \underset{1\text{ x }3}{\mathbf{0}} & \underset{1\text{ x }1}{\mathbf{0}} & \underset{1\text{ x }2}{\mathbf{0}} & \underset{1\text{ x }3}{\mathbf{0}} & \underset{1\text{ x }1}{\mathbf{0}} & \underset{1\text{ x }2}{\mathbf{0}} & \underset{1\text{ x }3}{\mathbf{0}} & \underset{1\text{ x }1}{\mathbf{0}}
\end{bmatrix} \tag{110}$$

3.4.1.5 Numerical integration

The number of integration points for the DKT element has been evaluated, where points beyond 3 did not contribute anything to the result as it becomes exact integration with 3 points due to the quadratic nature of the shape functions (2n-1 points is exact as discussed in [36]). Reducing to one integration point decreased accuracy quite notably, as expected.

Table 4. *Integration scheme for the DKT element with the weights W. Three points corresponds to exact integration.*

Integration point	ξ	η	W
1	1/6	1/6	1/3
2	1/6	2/3	1/3
3	2/3	1/6	1/3

The shape functions are linear for the CST element. Therefore, the Jacobian becomes constant for that case.

3.4.1.6 Element forces

Local forces, or element forces, can be derived by projecting global entities, using the unit vectors $\boldsymbol{n}$ and $\boldsymbol{m}$, thus identifying the local stress components [47]

$$\sigma_{nn} = n_x^2\sigma_{xx} + n_y^2\sigma_{yy} + 2n_xn_y\sigma_{xy} \tag{111}$$
$$\sigma_{nm} = n_xm_x\sigma_{xx} + n_ym_y\sigma_{yy} + (n_ym_x + n_xm_y)\sigma_{xy} \tag{112}$$
$$\sigma_{nz} = n_x\sigma_{xz} + n_y\sigma_{yz} \tag{113}$$

The bending and twisting moments are defined as bending and twisting per unit length. In addition, there is also vertical shear force per unit length. The fundamental definitions of bending and shear with unit vectors are

$$M_{nn} = \int_{-\frac{t}{2}}^{\frac{t}{2}} z\sigma_{nn}\,dz \tag{114}$$
$$M_{nm} = \int_{-\frac{t}{2}}^{\frac{t}{2}} z\sigma_{nm}\,dz \tag{115}$$
$$V_{nz} = \int_{-\frac{t}{2}}^{\frac{t}{2}} \sigma_{nz}\,dz \tag{116}$$

Starting from global moments and shear, the local components can be derived as

$$M_{nn} = n_x^2M_{xx} + n_y^2M_{yy} + 2n_xn_yM_{xy} \tag{117}$$
$$M_{nm} = n_xm_xM_{xx} + n_ym_yM_{yy} + (n_ym_x + n_xm_y)M_{xy} \tag{118}$$
$$V_{nz} = n_xV_{xz} + n_yV_{yz} \tag{119}$$

One may observe that the expressions for local stress, bending and shear components are on identical form. From this, it can be understood that principle moments can be determined in the same way as principle stresses [52]. This is a quite useful quantity for doubly curved surfaces, and is also implemented in the computational function DKT3s (see section 3.1). The principle stresses and moments are obtained by solving the eigenvalues from the stress ($\boldsymbol{S}$) and bending ($\boldsymbol{M}$) tensor

$$(\boldsymbol{S} - \lambda_\sigma\boldsymbol{I})\boldsymbol{n} = 0 \tag{120}$$

$$(\boldsymbol{M} - \lambda_M\boldsymbol{I})\boldsymbol{n} = 0 \tag{121}$$

3.4.1.7 Linear buckling theory

The mechanism behind buckling is induced by sufficiently high compressive membrane forces to cause instability. Normal forces are affecting the moment equilibrium equation. This can be understood by considering the moment equilibrium equation

$$\widetilde{\nabla}^T \boldsymbol{M} - \boldsymbol{V} + \widetilde{\boldsymbol{N}} \nabla w = 0 \tag{122}$$

with its corresponding weak form including the second order contribution:

$$\begin{aligned} &\int_\Omega [\nabla \delta w]^T \widetilde{\nabla}^T \boldsymbol{M} \, d\Omega + \int_\Omega [\nabla \delta w]^T \widetilde{\boldsymbol{N}} \nabla \delta w \, d\Omega \\ = &\int_\Omega \delta w \; q \; d\Omega + \int_\Gamma \delta w \; V_n^K \; d\Gamma - \int_\Gamma \frac{\partial \delta w}{\partial n} \; M_{nn} \; d\Gamma \end{aligned} \tag{123}$$

and $\widetilde{\boldsymbol{N}} = [N_{xx} \; N_{yy} \; N_{xy}]^T$. The membrane forces $\widetilde{\boldsymbol{N}}$ are calculated according to 1st order theory described in 3.4.1.2. Then the membrane loading is parametrized such that

$$\widetilde{\boldsymbol{N}} = \lambda \widetilde{\boldsymbol{N}}^{(R)} \tag{124}$$

(R) denotes the reference value of which λ is one and instability occurs [36]. For the FE formulation, a specific linear buckling approach has been derived for the DKT element. The corresponding geometric stiffness matrix is formulated to solve the eigenvalue problem

$$(\boldsymbol{K} - \lambda \boldsymbol{K_G})\boldsymbol{D} = 0 \tag{125}$$

In this expression, $\boldsymbol{K}$ is the standard element stiffness matrix, $\boldsymbol{K}_G$ is the geometric stiffness matrix that should be derived, λ is the load parameter which is essentially an allowed factor on the applied load, and $\boldsymbol{D}$ contains the corresponding buckling mode. These could be used for second order analysis or simply to visualize the linear buckling mode [57].

Through the potential energy formulation, the geometric stiffness matrix can be derived on the form

$$\boldsymbol{K}_G = 2A \boldsymbol{\alpha}_g^T \boldsymbol{G} \boldsymbol{\alpha}_g \tag{126}$$

with $\boldsymbol{\alpha}_g$ being a matrix (12x9) containing the constants p, q, r, t defined in section 3.4.1.2, which thereby is stated independently of ξ and η in local coordinates:

$$
\boldsymbol{\alpha}_g = \begin{bmatrix}
0 & 0 & 1 & 0 & 0 & 0 & 0 & 0 & 0 \\
-p_6 & -q_6 & 3-r_6 & p_6 & -q_6 & 3-r_6 & 0 & 0 & 0 \\
p_5 & -q_5 & 3-r_5 & 0 & 0 & 0 & -p_5 & -q_5 & 3-r_5 \\
p_5-p_6 & -q_5-q_6 & 6-r_5-r_6 & p_4+p_6 & q_4-q_6 & r_4-r_6 & -p_4-p_5 & q_4-q_5 & r_4-r_5 \\
p_6 & q_6 & r_6-4 & -p_6 & q_6 & r_6-2 & 0 & 0 & 0 \\
-p_5 & q_5 & r_5-4 & 0 & 0 & 0 & p_5 & q_5 & r_5-2 \\
0 & -1 & 0 & 0 & 0 & 0 & 0 & 0 & 0 \\
-t_6 & -r_6 & q_6 & t_6 & -r_6 & q_6 & 0 & 0 & 0 \\
t_5 & -r_5 & q_5 & 0 & 0 & 0 & -t_5 & -r_5 & q_5 \\
t_5-t_6 & -r_5-r_6 & q_5+q_6 & t_4+t_6 & r_4-r_6 & q_6-q_4 & -t_4-t_5 & r_4-r_5 & q_5-q_4 \\
t_6 & 1+r_6 & -q_6 & -t_6 & r_6-1 & -q_6 & 0 & 0 & 0 \\
-t_5 & 1+r_5 & -q_5 & 0 & 0 & 0 & t_5 & r_5-1 & -q_5
\end{bmatrix} \tag{127}
$$

The matrix **G** is defined in parent domain as

$$
\boldsymbol{G} = \int_0^1 \int_0^{1-\xi} \boldsymbol{J}^T \boldsymbol{N} \boldsymbol{J} \, d\eta \, d\xi \tag{128}
$$

If the normal forces $\boldsymbol{N}$ are constant over the element (CST element), the matrix $\boldsymbol{G}$ can instead be written

$$
\boldsymbol{G} = \begin{bmatrix} N_x \boldsymbol{C} & N_{xy} \boldsymbol{C} \\ N_{xy} \boldsymbol{C} & N_y \boldsymbol{C} \end{bmatrix} \tag{129}
$$

and the matrix $\boldsymbol{C}$ is just containing constants:

$$
\boldsymbol{C} = \frac{1}{360} \begin{bmatrix}
180 & 30 & 30 & 15 & 60 & 60 \\
30 & 12 & 2 & 3 & 18 & 6 \\
30 & 2 & 12 & 3 & 6 & 18 \\
15 & 3 & 3 & 2 & 6 & 6 \\
60 & 18 & 6 & 6 & 30 & 15 \\
60 & 6 & 18 & 6 & 15 & 30
\end{bmatrix} \tag{130}
$$

Now, the geometric stiffness matrix has been formulated on closed form directly in local coordinates [57].

3.4.2 Offset surfaces

The shell geometry is assigned as an offset surface to the form found cable net shape under concrete loading. This is based on deriving a mean normal vector in each node from the adjoining line element normals (**Figure 40**). Each node of the cable net is then translated half the shell thickness in the mean normal direction to approximate the position of the neutral plane of the shell [12]. MATLAB has great built-in functionality for this, which is used in the implementation.

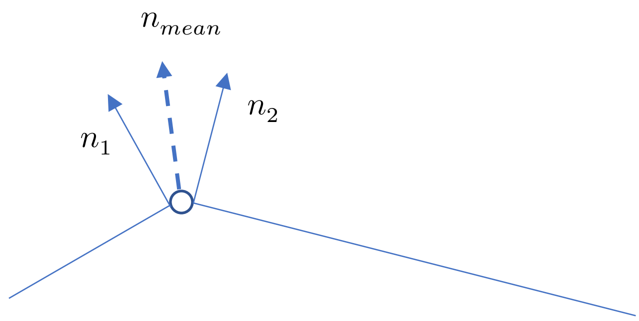

Figure 40. *Mean normal is derived to find the offset path (2D example).*

Since the shell is assumed thin however, this step can be skipped for many geometries.

3.4.3 Form and thickness optimization

Geometry has great influence on the stress distribution of any arbitrary structure, and therefore also the total load that any given structure can carry. If the constraints given by the architectural program allows for changes in general geometry, there exists a structural incentive to refine it. Identifying parts of the structure that attracts undesired load and then refining the geometry can be a way to optimize and improve structural performance on both local and global level. In the context of flexible formwork, changes in shell geometry to improve structural performance can be performed using the node position constraint when form finding the cable network, or directly adjusting the boundary.

Thickness was intended to be automatically set in early planning of the project. However, since this is a rather complex assignment due to many aspects such as the desired stiffness of the structure, load combinations, type of reinforcement, construction aspects and so forth, thickness was ultimately assigned manually for all verification problems as well as the case study. If this parameter should be optimized, it most likely needs to be a multi objective optimization where it is considered along other parameters.

3.4.4 Verification

Three tests are performed to check how accurate the element seems to reflect stress and moment distribution. The accuracy is also checked for both coarse and finer discretization. The linear buckling analysis is compared with two reference methods.

3.4.4.1 Rotated clamped plate

The DKT-based shell element is compared with a quadrilateral reference element [25]. The verification problem is used compare distribution of stresses and bending moments, but also confirming that the range of forces are indeed the same, along with a consistent minimum and maximum value. The problem is simultaneously used to verify the transformations between local and global domain. The studied plate is therefore rotated 90° such that the local x, y and z-axis does not align with the reference problem.

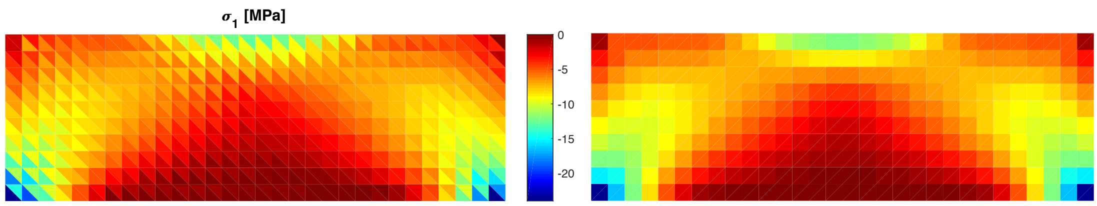

Figure 41. *First principal stress in the plate. DKT discretization to the left, quadrilateral reference element to the right. Color normalized between plots.*

The plate is clamped. The transverse displacement (w) is prevented around the entire plate. In addition, u_x and u_y translations are locked on the left and right side. An equally distributed traction ($t_y = -5$ MPa) load acts on the upper edge, and an equally distributed transverse load ($q = -1$ kPa). The thickness of the plate is 0.008 m with Young's modulus $E = 210$ GPa and Poisson's ratio $v = 0.3$.

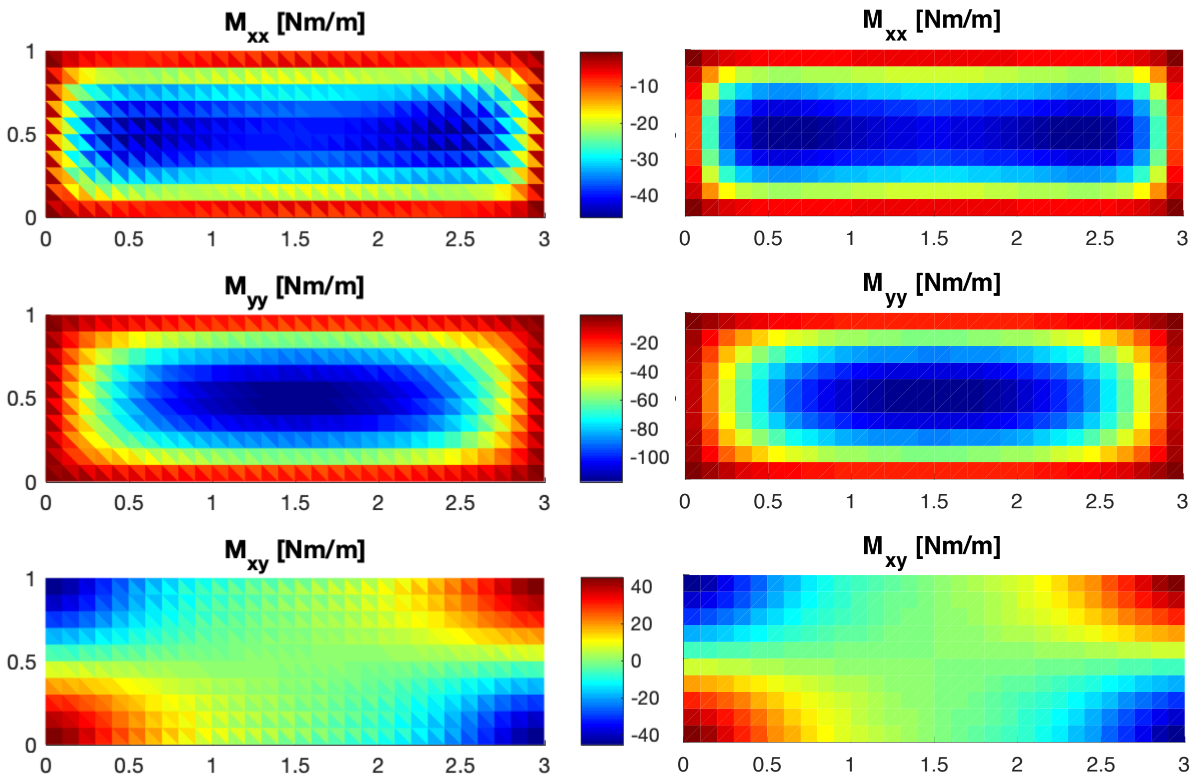

Figure 42. *Moment distribution with DKT element (left) and quadrilateral reference element (right).*

3.4.4.2 Simply supported beam

A plate strip is tested in unidirectional bending, comparable with the solution of a simply supported beam. The analytical solution from Euler-Bernoulli beam theory is used for verifying the equivalent plate strip. The test is performed for two different ratios between length and width of the plate, with various resolution of discretization, to see how the solution varies with increased number of elements. The result is presented in **Table 5** below. The distributed load was set to 1 N/m^2 and the strip width was constant at 1 m. The increase in elements was made in x-direction while discretization in y-direction was kept constant.

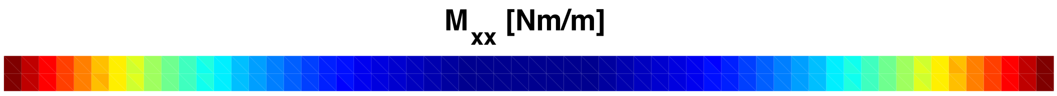

Figure 43. *Simply supported plate strip that was compared with an analytical solution based on Euler-Bernoulli beam theory.*

Table 5. *Error estimation between numerical solution using DKT elements, and analytical solution for a beam.*

L [m]	# elements	$M_{numerical}$ [Nm/m]	$M_{analytical}$ [Nm]	Error [%]
3	12	-1.066	-1.125	5.53
3	60	-1.123	-1.125	0.18
3	120	-1.124	-1.125	0.09
30	12	-106.362	-112.500	5.77
30	60	-112.267	-112.500	0.21
30	120	-112.447	-112.500	0.05
30	1200	-112.500	-112.500	0

Already at approximately 20 elements, the deviation fell below <2 % compared to the analytical solution.

3.4.4.3 Buckling analysis

A linear buckling analysis is performed on a clamped plate, loaded with a traction along the upper plate edge, as described in verification problem 3.4.4.1. Reference method 1 is referring to a general formulation for triangular elements by Doyle, 2011 [53]. Reference method 2 [25] is performed with quadrilateral elements. The first six load factors are compared.

Table 6. *Comparison of three different linear buckling analysis methods. As seen in the table, the DKT based analysis is providing results consistently between reference method 1 and 2.*

λ	DKT analysis [-]	Reference method 1 [-]	Reference method 2 [-]
1	5.17	5.22	5.13
2	7.53	7.60	7.37
3	9.84	9.99	9.50
4	11.58	11.88	11.10
5	13.44	13.89	12.82
6	15.84	16.44	15.02

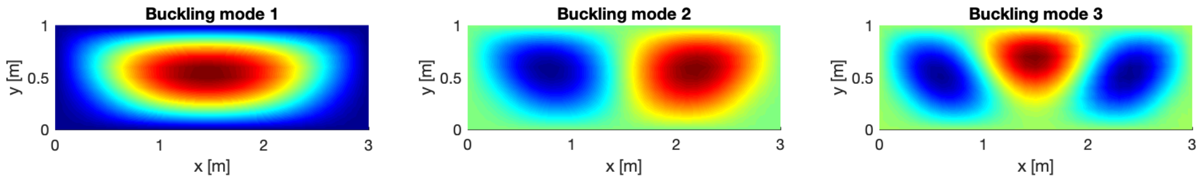

Figure 44. *The first three buckling modes in the comparison.*

3.4.5 Conclusion

- The DKT element results corresponds well to analytical solutions in verification. It has a clearly convergent behavior.

- $\boldsymbol{M}$ is not unique along the boundary shared by two elements. As a consequence, this is sometimes visually evident as the plot does not always appear fully continuous over the surface.

- The implemented buckling formulation is found to correspond well with the reference methods, always providing results between the two reference methods.

- Drilling degrees of freedom needs to be added to properly describe rotations for curved plates and shells in global coordinates. For plates, at least one node usually needs to be prescribed, but the linear dependence of the stiffness matrix disappears as soon as one or several elements are defined in different planes in global coordinates. This is seldom a problem for practical applications concerning shell structures.

- The DKT element sometimes induces errors in vicinity of the prescribed boundary but give reliable results otherwise.

- Principal stresses and principal moments has been found to give practical information about the force distribution on a doubly curved surface in general.

- Integration schemes of more than 2n-1 Gauss points (n is the order of approximation) does not improve accuracy.

3.5 Perimeter system analysis

The analysis of the external frame is performed using an existent computational framework called CALFEM, developed at Lund Institute of Technology. CALFEM is an abbreviation of "Computer Aided Learning of the Finite Element Method" [58]. It is originally developed as a teaching tool for use with MATLAB, but has recently been transposed for use with Python as well. The library comes with a user manual which makes it rather easy to implement [25]. CALFEM functions are used for to establish stiffness matrices and forces for beam and bar elements in the FE analysis of the perimeter system. This is complemented with some overbridging lines of code to integrate the already developed mesh functions and being able to import geometry and connectivity information as well as reaction forces from form finding analysis of the cable network.

Since it already exists a user manual for most of the functions in CALFEM, the interested reader is referred to the framework website https://sourceforge.net/projects/calfem/ for more information.

3.5.1 Reaction forces transferred from the cable network

The vector representation shown in **Figure 45** introduces an intuitive overview on how the perimeter system is loaded, and informs the designer with probable deformations. This information is used to set up a perimeter system geometry for the first iteration. The perimeter system deformations is calculated and sent back to the cable net solver in an iterative procedure, updating the position of the fixed boundary nodes of the cable network.

The reaction forces can be derived directly from expressions in section 3.2.2.4 and becomes [7]

$$\begin{aligned} \boldsymbol{R}_x &= \boldsymbol{C}_f^T \boldsymbol{Q} \boldsymbol{C} \boldsymbol{x} \\ \boldsymbol{R}_y &= \boldsymbol{C}_f^T \boldsymbol{Q} \boldsymbol{C} \boldsymbol{y} \\ \boldsymbol{R}_z &= \boldsymbol{C}_f^T \boldsymbol{Q} \boldsymbol{C} \boldsymbol{z} \end{aligned} \tag{131}$$

Reaction forces along the boundary of the net are calculated and sent to the perimeter system model to analyze perimeter deflections. The deformed positions of the perimeter beams are sent back to the cable net analysis model to update the fixed nodal coordinates in an iterative process. This step can often be neglected given that deformations are sufficiently small.

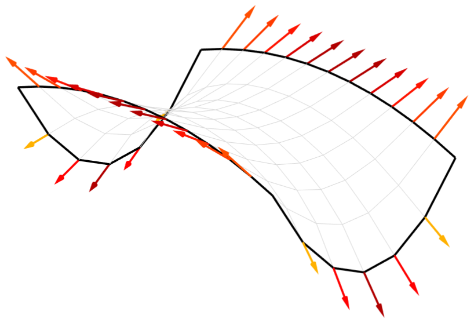

Figure 45. *Reaction forces along the boundary of the cable net.*

3.5.2 Verification

Perimeter system functions will not be verified since it makes use of existing functions, assumed to be accurate within acceptable tolerances.

3.5.3 Conclusion

- Automatic transfer of reaction forces from the cable net has been found convenient in design of the perimeter system.

- CALFEM functions were easily utilized. Syntax of the developed framework has been designed with this in mind, and functions integrate well. The developed functions for shell elements in section 3.4 can be used in combination with the beam and bar elements from the CALFEM library.

4 Case study

A case study is performed to verify the developed computational framework and overall performance of the formwork concept. The first part of this chapter consists of design and analysis aspects. The second part concerns the planning and process. Evaluation and comparison between predictions and the built structure are then presented.

4.1 Brief

A concrete pavilion will be designed and constructed in a residential garden with the intention to serve as a permanent structure. It should be large enough to hold two chairs under cover but still small enough to minimize the use of material, required building time and total cost. The structure should have a doubly curved anticlastic geometry to fully verify the flexible formwork concept.

4.1.1 Location

Southwest of Sweden. Snow loads are intermediate while wind loads are significant. The location has partly exposed bedrock, moraine and a mixed top soil layer of sand, clay and organic material. Due to the slope from a pine forest down towards an exposed line of bedrock, the location has high levels of groundwater at times. Works on drainage and stability is necessary prior to construction to avoid freeze-thaw damages and partial settlements. Location is close (within 1 km) to the sea, with significant amounts of salt in the air.

4.1.2 Choice of concept

A few different concepts are developed and evaluated with regard to architectural program, structural integrity, buildability and ease of verification.

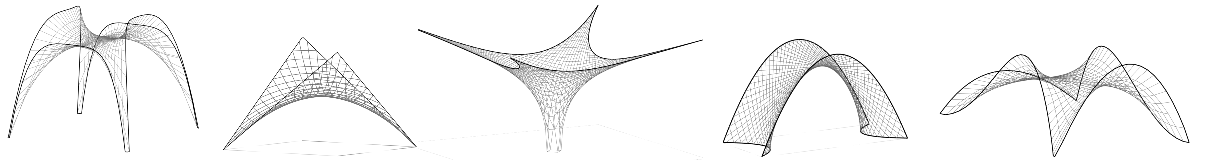

Figure 46. *Conceptual designs for the case study prior to the selection of one concept that will be used for construction and validation.*

An arch-like structure is chosen since this geometry is thought to be relatively easy to erect while still providing enough covered area with room for two chairs and a coffee table. To make the design more interesting, the structure will have a linearly varied width as shown in **Figure 47**. The longitudinal boundary curve is designed with the surface equation

$$f(\boldsymbol{x}, \boldsymbol{y}) = -0.72(\boldsymbol{x} - x_{max})^2 \tag{132}$$

Starting from a rectangular mesh, the boundary lines in y-direction are linearly narrowed over the length. As a final touch, the left and right transversal boundary are adjusted with the hyperbolic function

$$\boldsymbol{x}(\boldsymbol{y}) = k \cosh\left(\frac{\boldsymbol{y} - y_{max}}{k}\right) \tag{133}$$

With k being a constant of -0.75 and 0.35 for left and right transversal boundary respectively. Both curves are then translated such that the outer coordinates maintain their position shared with the upper and lower boundaries, as demonstrated in **Figure 47**.

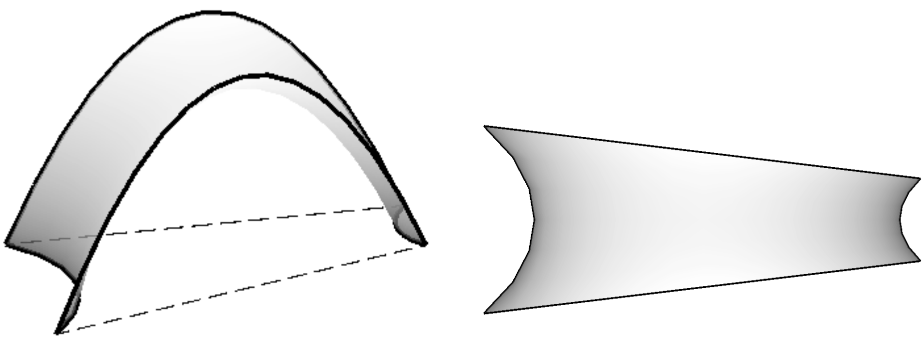

Figure 47. *Overview of the chosen concept geometry.*

4.2 Design and analysis

4.2.1 Cable network analysis

Two equilibrium shapes has been analyzed. The two shapes that need to be form found is the prestressed but externally unloaded state, and the final shape from concrete loading. The prestressed state is the built geometry, and the second one gives the shell geometry used in FE analysis. Obviously, the cable network capacity needs to be checked for both cases. The cables are assumed fully fixed along the boundary line and the net is oriented to roughly follow principal curvature.

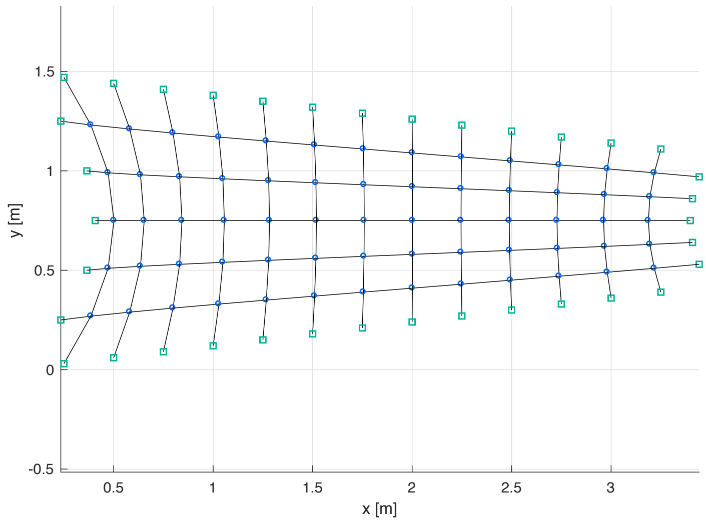

Figure 48. *Projection of the cable network layout. The projected distance between nodes is approximately 0.25 m.*

The prestressed shape is form found based on constant force densities. This means that the solution is linear with FDM, without any need for iterations. A shape based on constant cable force was also explored (described in section 3.2.3.3), but it resulted in quite uneven element lengths (given that the net is oriented to follow principal curvature), making such a solution less practical to build. Another aspect is the change of force distribution in the net when adding the concrete load. Constant force constraints gave a rather big difference in cable forces between load states, while constant force densities gave a consistent and practical distribution.

The shape under concrete load was form found starting from the prestressed geometry with a material stiffness constraint as described in section 3.2.3.2. As seen in **Figure 49**, the force interval is kept within the same range, while at the same time avoiding cable slacking from concrete loading. The force range was decided in compromise between stability of the formwork and practical aspects of achieving the intended prestressing forces in practice.

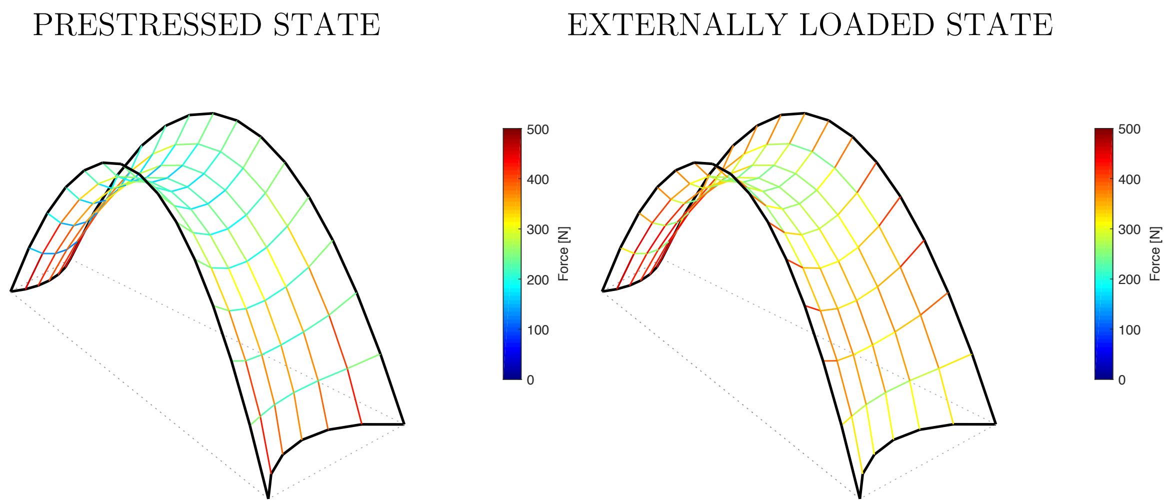

Figure 49. *Force distribution in the two different load states. The prestressed state has forces ranging between 109-501 N. With the concrete added, the distribution and range changes to 208-438 N.*

The thinnest commercially available and suitable cable in the local area is a galvanized, PVC-coated steel wire (2-3mm) with tensile strength of 375 kg. This gives a utilization ratio of only 13.6 %. It is of course extremely on the safe side, although governed by price and availability.

4.2.2 Membrane analysis

Based on the empirical investigation in Appendix A.2 , a standard geotextile is chosen due to its partly frictional and semi-elastic properties.

4.2.2.1 Sagging

It was not possible to determine exact properties of the chosen fabric. Therefore, the expected sagging is estimated with an empirical test (**Figure 50**). The sagging effect will naturally vary with the slope, so estimation is based on a setup with the fabric taking fully vertical load. This is expected to cause the largest deformation of the fabric (with respect to out of plane deflection), and is used to apply designated loads from self-weight in the form finding analysis. The result from this study gave approximately 10 mm deflection in the center of a 200 x 200 mm piece of fabric clamped in one direction, without prestressing of the fabric. In the analysis of the capacity, this extra local thickness is ignored to be on the safe side, but it is considered in the total load effect.

Figure 50. *The picture to the left shows the setup to verify sagging effect. The fabric is clamped around a quadrilateral, which is representing the cables carrying the fabric. Picture to the right is showing the chosen fabric, a standard geotextile from the local building store.*

4.2.2.2 Patterning and flattening

The patterning is made symmetric, such that the side patches are identical, with a centered patch joining them together. This is intended to simply the manufacturing process. The seam lines are placed to follow the cable lines. Doing so, it is also possible to partly clamp the fabric around cable lines to keep the fabric in place while adding concrete. Even if the concrete is applied in a symmetrical and systemized manner, the fabric is expected to be locally stretched temporarily, before each quadrilateral is fully covered.

In total, the membrane is subdivided into three patches to cover the entire surface. Each patch are then flattened as described in section 3.3.5. The flattened patches are presented in **Figure 51**.

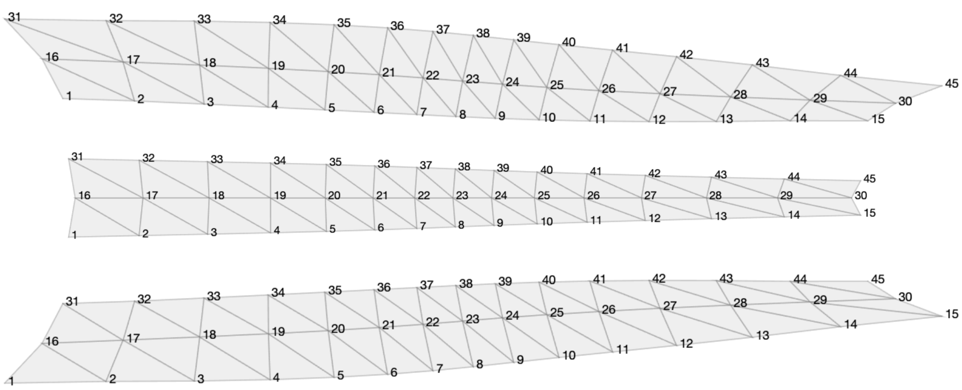

Figure 51. *The patches are divided symmetrically. These are sewn together to achieve one continuous fabric to place on the cable net. The outer sides are connected to the timber side beams with staples.*

4.2.3 Shell analysis

The shell is constructed with fiber reinforced concrete that rests on a steel reinforced foundation slab. Stirrups are used between the slab and shell to provide proper anchorage against tilting, but also to act as shear connectors in the construction joint.

4.2.3.1 Discretization

The number of nodes used in the cable net analysis is usually not sufficient to create a fine enough FE mesh with an acceptable result. Therefore, the discretization is refined by calculating a surface fit from the cable network coordinates as shown in **Figure 52**. The surface is then used to extract new node coordinates for the FE mesh, using shell elements.

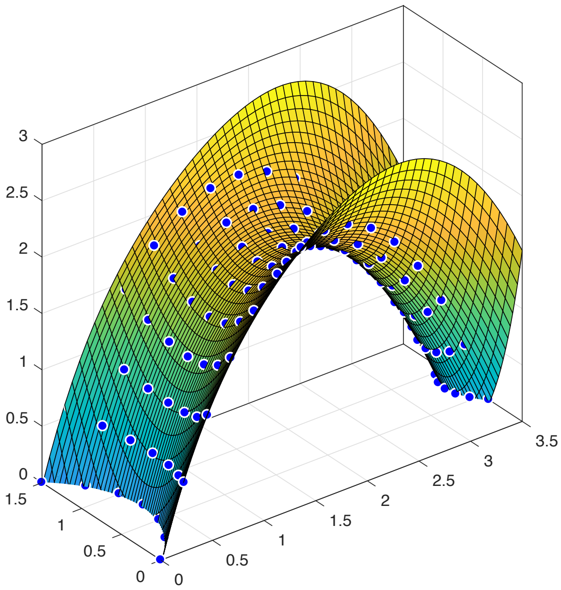

Figure 52. *Surface fit based on the cable network coordinates (5th order approximation).*

4.2.3.2 Boundary conditions

To handle horizontal thrust, the concrete shell is designed to have steel reinforcement connecting the shell and slab although such forces are estimated fairly small due to the high inclination. As a consequence of the intended connection, the boundary is chosen as fixed in all translational degrees of freedom (dof) where the coordinate in z is zero. Due to the fairly thin shell, rotational dof's are estimated to be unconstrained. Considering structural behavior on a global scale however, this connection will most likely induce some bending resistance due to the curved boundary.

4.2.3.3 Loads

Load combinations are specified according to Eurocode and the loads considered are self-weight, environmental loads, live loads (i.e people climbing on it), and loads due to settlements. The latter one is considered by imposing a deflection instead of setting prescribed boundary to zero. Thermal loads are neglected since the shell is uninsulated, meaning the stress gradient from temperature is neglectable at all times. The arising normal stresses from temperature variations in general is assumed neglectable. On a final note, there will be restraint forces due to shrinkage and creep deformations. The analysis has been simplified to treat such effects through a higher safety factor.

Table 7. *Magnitudes of all considered loads, used for ULS combination*

Load	$[\mathbf{N/m^2}]$	γ (unfavorable)	ψ_0
Self-weight	840	1.35	-
Snow	1500	1.5	0.6
Wind	1500	1.5	0.6
Live load	2.0 kN*	1.5	(0.7)**

* Concentrated load, distributed approximately over nodes within 0.1 x 0.1 m area.
** Live load is the main variable load for the governing case.

The self-weight was calculated by using a generalized specific weight of 24 kN/m^3, with an average thickness of 35mm due to sagging (actual thickness for capacity check is set to 25 mm).

Environmental loads are based on Eurocode. However, shape and pressure coefficients can heavily effect the applied loads, and the available ones are not believed to properly represent a shell with this geometry. In summary, there is some uncertainties with respect to these loads, and conservative assumptions has therefore been adopted in design.

There is a risk for accidental loads, such as trees falling down on the shell. However, this is considered highly unlikely. In such a scenario, there is a small risk of injury and therefore the shell should not be occupied. Surrounding trees will be inspected on a regular basis.

ULS combination (governing load effects in the Ultimate Limit State)

$$\gamma_g g_{sw} + \gamma_q q_{liveload} + \gamma_q \psi_o q_{snow} + \gamma_q \psi_o q_{wind} \tag{134}$$

SLS combination (deflections in Serviceability Limit State)
Deflections are small even under ULS load, so this combination is skipped and replaced by ULS combination.

4.2.3.4 Error estimation

The mesh shows convergent behavior (<2 %) using the current mesh with 2688 elements. This has been determined by gradually approaching a finer discretization and comparing mid deflection in z-direction.

4.2.3.5 Stresses and deflections

Load combinations with varying main loads are tested in FE analysis. The worst case stems from the live load being the main load since this induces the highest bending moment in the structure. All equally distributed loads could be increased with rather extreme safety factors (4-5) before they had any significant impact on the summed stresses.

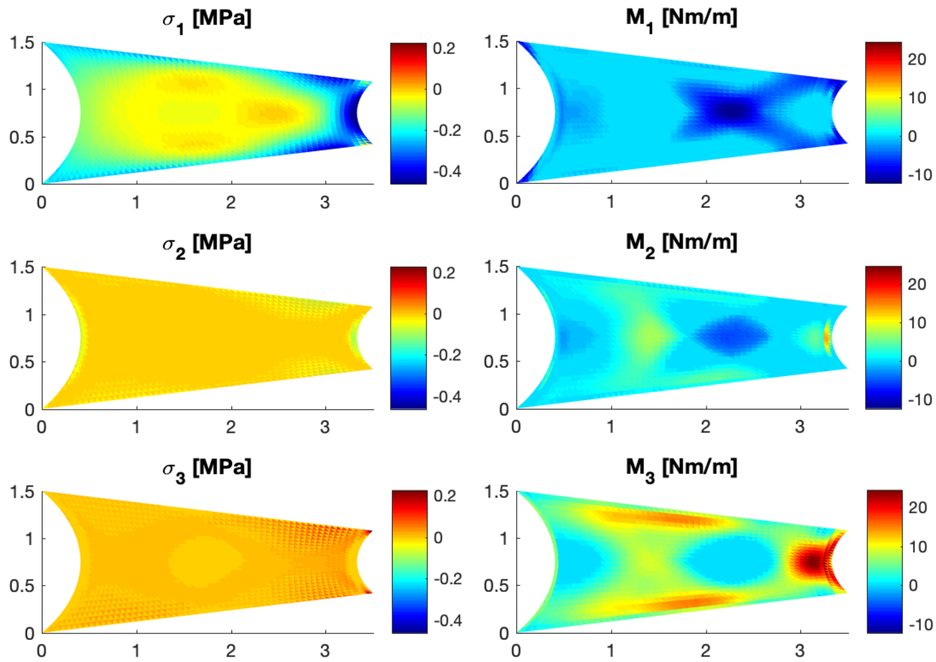

Figure 53. *Principal stresses and moments from self-weight only. As seen in the figure, the bending from an equally distributed load is neglectable.*

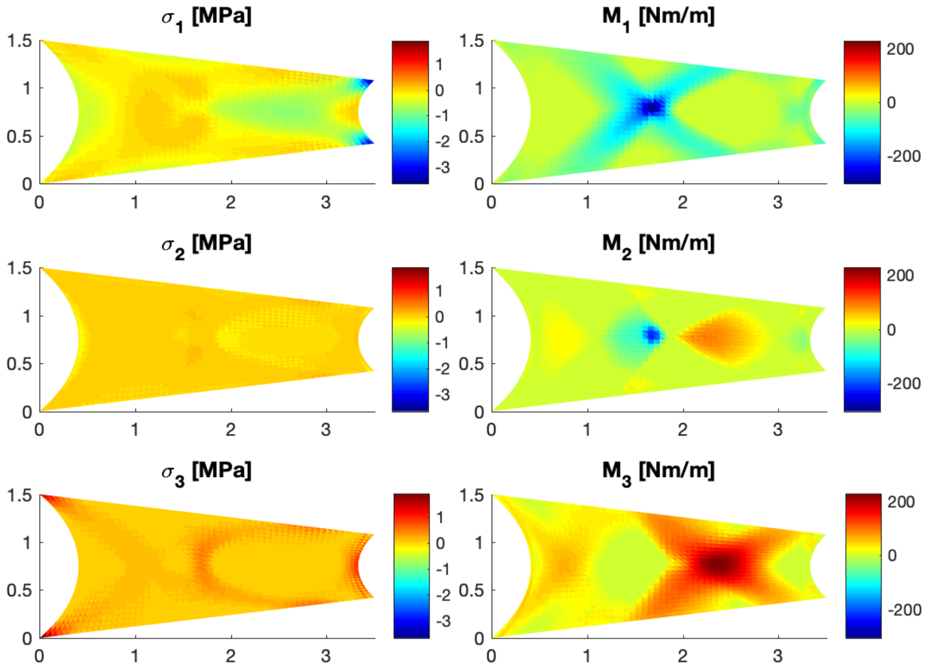

Figure 54. *Principal stresses and moments from the governing load combination. This is a rather extreme and conservative case with storm winds, fully loaded with snow, and a live load corresponding to two humans still being able to stand on top of it on 0.1 x 0.1 m concentrated area.*

Maximum bending moment for the governing load combination in ULS reaches -302 Nm/m, positioned under the live load. Maximum tensile stress was found to be approximately 1.8 MPa.

Table 8. *Deflections in the concrete shell for the governing load.*

	Min deflection [mm]	(x, y)	Max deflection [mm]	(x, y)
a_x	-0.01	$(0.42, 0.69)$	0.48	$(2.48, 0.75)$
a_y	-0.32	$(2.56, 0.31)$	0.36	$(2.50, 1.20)$
a_z	-0.27	$(1.46, 0.75)$	0.26	$(2.48, 0.75)$

Somewhat surprisingly, the deflections for the governing load case are extremely small (<1mm). However, the designed geometry is assumed to be very stiff with its high curvature in both directions, so the result is still plausible.

4.2.3.6 Buckling analysis

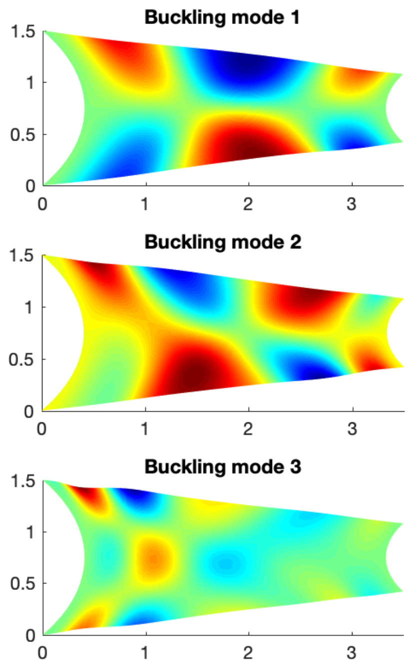

Figure 55. *The first three buckling modes corresponding to the governing load combination, with load parameters presented in* **Table 9**.

As seen in **Table 9**, the shell is insensitive to buckling. Even with a conservatively chosen knock down factor as proposed in [24], the risk of buckling is nonexistent. The calculation was based on the ULS load combination and the resulting normal stresses as basis for the reference load.

Table 9. *Buckling load parameters for the three first buckling modes. ULS load combination is used as reference load.*

Buckling mode	λ [−]
1	171
2	188
3	217

4.2.4 Perimeter analysis

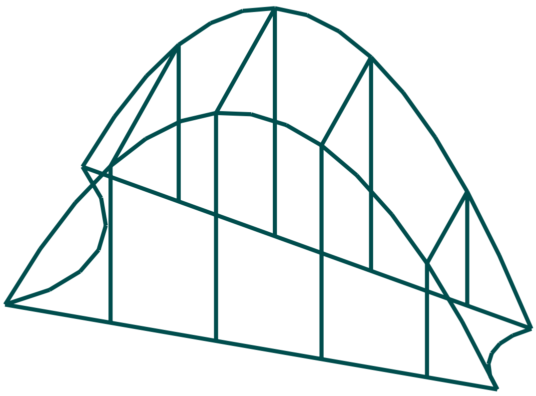

Figure 56. *Timber frame geometry.*

The perimeter system is constructed as a timber frame. The structure consists of main side beams along the perimeter and transversal compressive struts connecting them. The structure also have horizontal bracings, although not visible in **Figure 56**.

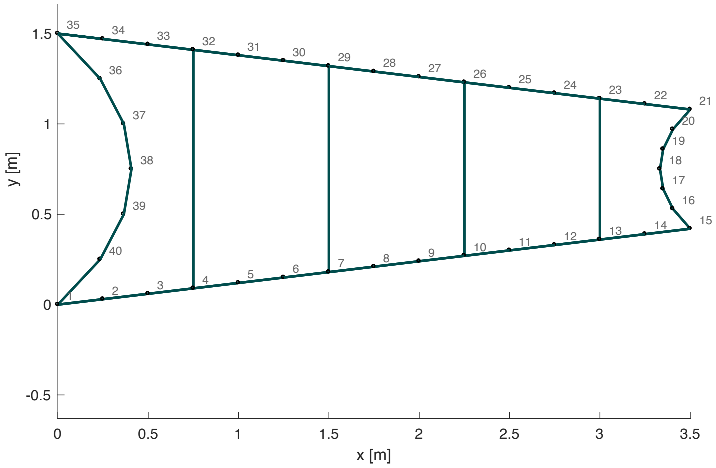

Figure 57. *Left: Projection of the external frame. Nodes coordinates are corresponding to boundary nodes in the cable network analysis. Right: Overview of the structural system.*

4.2.4.1 Boundary conditions

Translational degrees of freedom is locked in all 4 bottom corners along with the center node on the transversal beams where longitudinal cables are connected (node numbers 1,15,18,21,35 and 38 in **Figure 57**), assuming the transversal beam can be temporarily anchored in the concrete slab. This temporary anchorage was ultimately replaced with an additional beam attached to the side beams to reduce deflections, thus avoiding to drill in the slab.

4.2.4.2 Loads

Loads are retrieved directly from the cable network analysis, with direction cosines and magnitude (see **Figure 58**). Capacity is checked for both the prestressed and externally loaded state (concrete self-weight is governing vertical load). A simplified horizontal stability check is also performed. A point load (1 kN) is added in random nodes and directions in the horizontal plane to see how sensitive the perimeter system is to disturbances during the cast process. A safety factor of 1.5 is used.

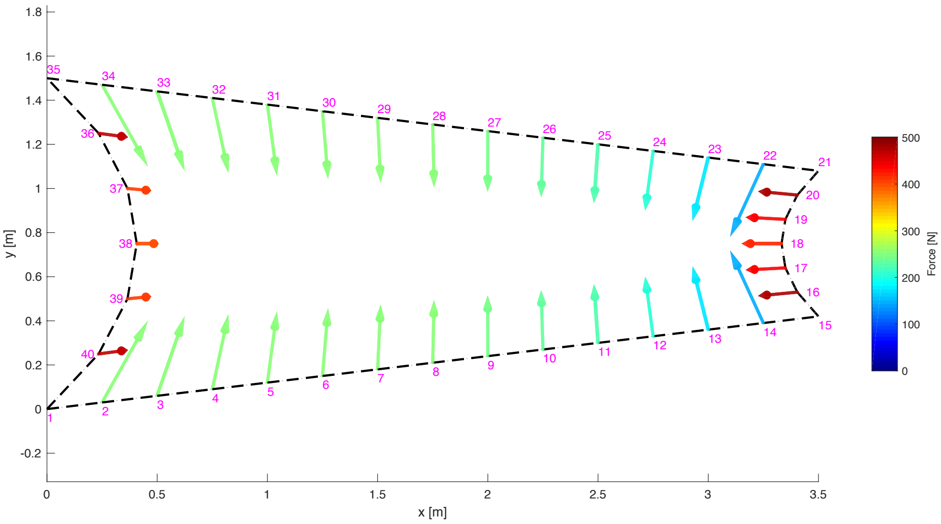

Figure 58. *Projection of the loads acting on the timber frame from prestressed cables, before concrete load is added. After the cast of concrete, the magnitudes of reaction forces are basically "reversed", with the transversal cables taking the highest force and decreasing forces at the left and right boundary.*

4.2.4.3 Stresses and deflections

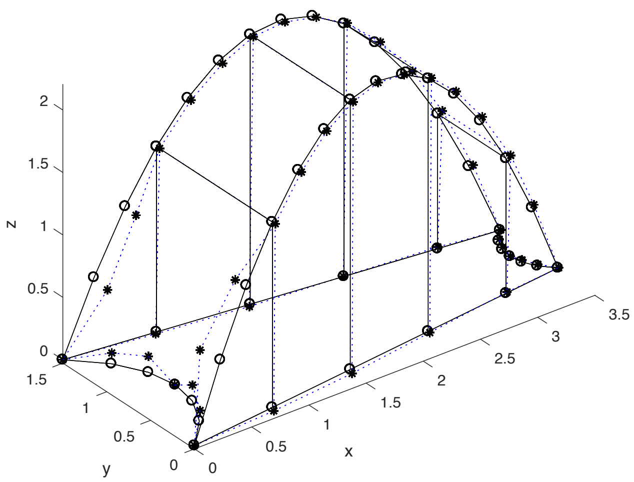

Figure 59. *Predicted deflections in the structure from vertical loads. The dotted line is showing the deformed geometry with a scale factor.*

The structural system is designed in an iterative procedure where the element dimensions and compatibility is adjusted gradually until a small enough deflection with reasonable sizes can be achieved. The starting guess was 45x120 mm side beams and 45x45 mm struts. The analysis showed that the structure can easily carry the loads with these dimensions, but the struts were ultimately assigned 45x90 mm for increased stability, but also to simplify connections with 6x80 mm screws.

Table 10. *The most significant deflections in the timber frame based on dimensions 45x120 and 45x90 for side beams and struts respectively.*

	Min deflection [mm]	Node	Max deflection [mm]	Node
$\boldsymbol{a_x}$	-0.4	2	0.4	23
$\boldsymbol{a_y}$	-2.7	34	2.7	2
$\boldsymbol{a_z}$	-0.3	30	1.3	39

As seen in **Table 10**, the deflections are small enough to neglect deformations of the perimeter system in the cable network analysis. No iterative refinement of the network boundary coordinates is therefore necessary.

4.2.5 Preliminary design of capacity

The concrete shell thickness is assumed as 25 mm. However, close to the connection with foundation, the shell thickness will be made thicker, approx. 50 mm, to ensure covering of the rebars there, as well as extra capacity since these areas receive the highest stresses in general.

4.2.5.1 Capacity checks

Bending capacity can be estimated through the fundamental definition by summing stresses over the cross sectional area with their respective level arm. With a linear variation of stresses from the neutral axis and reaching maximum at the shell edges, a relation based on allowed stress $f_{c,t}$ is made (tensile capacity of concrete). The design is intended to remain uncracked for the majority of loads.

$$M_{capacity} = \int_{-\frac{t}{2}}^{\frac{t}{2}} z\sigma(z)dz = \frac{2f_{c,t}}{t}\int_{-\frac{t}{2}}^{\frac{t}{2}} z^2 dz \tag{135}$$

$$M_{capacity} = \frac{f_{c,t}}{6}t^2 \quad \left[\frac{\text{Nm}}{\text{m}}\right] \tag{136}$$

This approach gives an approximate bending moment capacity of 625 Nm/m for 25 mm thick shell with a chosen concrete tensile capacity of 6 MPa (Maximum bending load effect in the shell has been calculated to approximately 300Nm/m). This of course needs to be considered in combination with occurring membrane stresses, of which the sum of stresses must not exceed the tensile capacity. Fortunately, as seen in **Figure 54**, the highest bending moment and tensile membrane stresses does not occur in the same areas. Even if they would, the capacity would still be sufficient.

An alternative capacity check with regard to both bending and normal stresses is to simplify the arch like a one-dimensional structural member and check the bending stresses as a beam cross section, and applying Navier's formula [59]:

$$\sigma = \sigma_m + \frac{M}{I_y} z \tag{137}$$

The second moment of inertia is calculated based on a conservatively chosen U-section, with width 0.5 m and vertical side heights conservatively assumed as 0.1 m (shell thickness constant at t=0.025 m, $z_{tp} = 0.0232\ m$).

$$I_y = \frac{0.5t^3}{12} + 0.5t\left(z_{tp} - \frac{t}{2}\right)^2 + 2\left(\frac{t0.1^3}{12} + 0.1t(0.05 - z_{tp})^2\right) = 9.84e - 6\ \mathrm{m}^4 \tag{138}$$

$$\sigma = (\sigma_m) + \frac{M}{I_y} z = \frac{300}{9.84e - 6} 0.025 = 0.76\ \mathrm{MPa} \tag{139}$$

The highest stress from bending is thus 0.76 MPa. This can be super positioned to the highest occurring membrane stress (1.8 MPa), of which the sum is far from the tensile capacity ($f_{ctk0.05}$ based on C50). The bending moment was assumed 300 Nm (peak value in Nm/m), which is rather conservative by observing results in **Figure 54**. For this type of 'strip calculation' approach, the calculated load effect in [Nm/m] needed to be converted to [Nm]. This is often done by adopting a transversal mean bending moment, following a few assumptions. There exists a few more or less suitable approaches, where one conservative approach (for reinforced concrete slabs) can be found in [60]. One must be careful in this application since there is no plastic redistribution of capacity, which is assumed in a steel reinforced slab. Therefore, a strict mean value is perhaps not as suitable for a fiber reinforced concrete, but a more conservative value should be chosen. The peak value has been chosen in this thesis, on the safe side.

The vertical shear components (V_{xz}, V_{yz}) are expected to be rather small due to the geometry, which induces mainly membrane forces. However, punching shear capacity is checked with a simplified approach to ensure capacity for concentrated live loads on the thin shell. The live load is checked while acting on a surface of 0.1 m in diameter. The area that should be checked with respect to shear stresses is therefore

$$A_{shear} = td\pi = 0.025 * 0.1 * \pi = 0.0079\ m^2 \tag{140}$$

The sum of shear force acting on this surface is $F_{liveload} = 2.0$ kN according to **Table 7**. The shear force thus becomes

$$\tau_{xz} = \frac{F_{liveload}}{A_{shear}} = 0.25\ \text{MPa} \tag{141}$$

Based on $f_{ctk0.05}$ of a C50 concrete with an added safety factor of 1.5, the shear strength is calculated as 0.48 MPa [61]. Thus, there should be sufficient capacity with regard to punching shear.

Influence of creep and shrinkage has been neglected. The water-cement ratio is low which is reducing drying shrinkage, and there is no stated design life such that creep deformations becomes relevant.

4.2.5.2 Concrete mixture

Considering the load effects, it is found suitable and sufficient with a fiber reinforced concrete. The mixture is based on workability demands determined through empirical tests in section A.3 , but also on guidelines given by Dr. Ingemar Löfgren (who should not be blamed for any possible misunderstandings), Adj. Professor at Chalmers University of Technology, and Head of Research and Development at Thomas Concrete Group, who kindly sponsored the ingredients except for the premixed product. The final mixture (approx. 250-275 liters of concrete) consists of:

Table 11. *Concrete mixture. The mixture varied slightly depending on the slope. Therefore, the total amount is accounted for in the table.*

Qty. [kg]	**Description**
625	C50/60 premixed product with mixed aggregates 0 - 6 mm
63.0	Water
5.0	Limestone filler (<0.125 mm)
0.1	Superplasticizer MasterGlenium SKY 615
2.0	PVA Kuralon RF4000 30 mm, diameter 660 µm
0.9	Super-Cracknon ASC 13H-530X (Nippon Electric Glass, Alkali resistant)

Filler content was gradually reduced during the cast process since it was quickly realized that the concrete got to easily disturbed in high slopes. It was necessary to work in a pace where the previously added concrete was hydrated enough to carry added masses above. The fiber content was gradually increased to lock the paste even further.

4.3 Construction

This section explains the adopted methodology in the construction process and provides documentation of used materials and specification of the total cost.

4.3.1 Construction methodology

To organize and rationalize the construction work, a methodology is developed. The aim is to minimize both construction time as well as avoid possible problems during the formwork erection. This will also help evaluate the investigated formwork compared to traditional formwork. Pictures from the actual process is added to clarify the execution of each step.

1) **Ground preparation**
   The quality of the soil is inspected. Settlements are critical for any shell structure and should thus be minimized already in design considerations. Compacted friction material should be used with capacity and sufficient depth to handle repeated ground freezing. This will be done according to SS-EN-1997-1 (EKS 10) but is left out for brevity.

Figure 60. *ground preparation with soil improvement and drainage.*

2) **Foundation work including cast-work of a reinforced concrete slab**
   A separate analysis on the foundation has been performed. This is a steel reinforced concrete slab, designed with tension anchorage between supports to handle horizontal reaction forces from the shell. This is constructed according to SS-EN-

1992-1-1 (EKS 10) but is left out for brevity since it is not part of the studied concept.

Figure 61. *Steel reinforced concrete slab. Formwork and reinforcement layout to the left, finished slab to the right.*

3) **Construction of perimeter system**
The curved side beams are manufactured on the ground and raised in pre-fabricated sections, joined together with transversal struts and horizontal bracing. Horizontal bracing is verified empirically. Boundary node positions are measured and drilled in place by checking height and measuring the absolute distance from a reference point.

Figure 62. *Erection of the timber frame.*

4) **Mounting and prestressing of cable network**
   Cable forces are verified with a spring system. The spring constant and prestressing force is determined empirically to account for deviations between individual springs as well as properly determining the force in each cable (for documentation, see appendix). Cables are then mounted starting with transversal direction. Intersections are clamped with zip ties. This needs to be a systematic process in at least two steps, verifying forces and element lengths gradually. The springs are locked prior to concrete loading such that spring elongations will not affect the loaded shape.

Figure 63. *Prestressed cable net with zip ties used as cross clamps.*

Correct prestressing forces are determined by adjusting the turnbuckles and measuring spring elongations. Final node positions are verified with help of a level laser (accuracy $\pm$ 0.4 mm/m).

Figure 64. *Turnbuckle and spring setup for prestressing (left). Verification of node positions by laser (right).*

5) **Patterning and sewing of the membrane**
Three patches are cut and sewed together on location. Patches are cut following a list of coordinates from analysis. Node positions are marked on the fabric to connect the patches consistently.

Figure 65. *Measuring and cutting process (left) and the finished patched fabric (right).*

6) **Membrane mounting and connection to perimeter system**
Node positions are marked out on the fabric to position it properly. It is connected to the side beam by staples, following drawn boundary lines.

Figure 66. *Membrane stapled to the side beams and attached to the cables beneath.*

7) Preparing the concrete mixture

For this rather small case study, the concrete is mixed by hand. Some test mixtures are done to verify workability. Final concrete mixture documented in 4.2.5.2.

8) Concreting

Concrete is added continuously from both ends to avoid uneven loading during the cast process. Concrete ingredients are also weighed for possible retroactive verification.

Figure 67. *Cast process.*

9) Drying time

Control of formwork and possible watering of the concrete, depending on relative humidity and temperature. The concrete is covered at all possible times to prevent early evaporation causing insufficient water for the hydration process.

Figure 68. *Removal of formwork. The cable imprint is distinct, which was expected with respect to given amount of fabric prestressing.*

10) Removal of the formwork

Formwork are removed by first releasing tension in the cable net, starting with longitudinal cables. Transversal cables are then released gradually. The membrane is removed, followed by horizontal struts, and finally side beams.

Figure 69. *Finalized shell.*

4.3.2 Material specification and cost

Table 12. *Cost and quantity of the used concrete (sponsored products not included).*

Article	Qty.	Description	Cost SEK
Concrete, found.	10 x 25 kg	Premixed aggregates 0-6mm	524
Concrete, shell	28 x 25 kg	Premixed aggregates 0-6mm	1466

SUM: 1990 kr

In addition, a few products was sponsored by Thomas Concrete Group (section 4.2.5.2).

Table 13. *Cost of materials related to the formwork.*

Article	Qty.	Description	Cost SEK
Gravel	1 [m^3]	Filling material	350
Timber	16.2 [m]	45x120	372
Timber	31.8 [m]	45x95	507
Timber	19.2 [m]	21x70	158
Reinforcement	- [m]	8mm bars + net 1200x800	250
Screws	200 pcs	FZB 6x80 mm	160
Screws	200 pcs	3.4x45 mm?	150
Steel plate	18 pcs	40 x 160 x 2 mm	107
Cable/steel wire	100 [m]	Galv. PVC coated 2-3 mm	398
Wirelock	20 pcs	Duplex elzink M3	200
Turnbuckle	18 pcs	Size M6	540
Zip ties	- pcs	200 mm	60
Screw eyelet	18 pcs	FZB 20x50	137
Geotextile	25 [m]	Class N1 1,4 x 25 m	399

SUM: 3788 kr

Materials in **Table 13** that could be reused are highlighted in blue (for this comparison, the timber has been excluded although some of it are in good condition after first use). Their cost is 1382 kr of the total 3438 kr, gravel for foundation excluded. This results in waste material for 2056 kr, or 312 kr/m^2 of finalized shell (total surface area of 6.58 m^2). Of this value, foundation timber cost constitutes 24 kr/m^2, which could in all fairness be excluded.

Equivalent cost of labor is harder to estimate since the case study was performed with unskilled labor (enthusiastic academics). Total man-hours for the formwork is with some uncertainties estimated to 42 hours. If 400kr/hour is assumed, this results in 2553 kr/m^2. This is considered an upper limit since it is based on first time experience and realization. Furthermore, improvement in construction methodology can dramatically improve total time which will have large impact on total cost. In total, a flexible formwork in this study is thus estimated to cost 2865 kr/m^2 as an upper limit.

Previous studies on the cost of traditional formwork indicate that in summary, today's cost of a standard timber formwork would range between 400-800 Euros [7], or with an exchange rate of 10.6 (29 may, 2019) in SEK, 4240-8480 kr. This range is reported to be excluding the foundation.

4.4 Verification and evaluation

Table 14. *Comparison between predicted node height and actual. Mean deviation is 0.5 %.*

Node	z [cm]	z ref [cm]	Δz [cm]	deviation [%]
3	39.7	42.2	-	-
11	130.6	130.0	-0.6	-0.5
13	115.1	115.9	0.8	0.7
15	130.1	129.9	-0.2	-0.2
17	147.4	147.6	0.2	0.1
19	147.1	147.6	0.5	0.3
21	181.2	180.9	-0.3	-0.2
23	165.5	164.1	-1.4	-0.9
25	182.0	180.9	-1.1	-0.6
27	180.8	180.8	0.0	0.0
29	181.8	180.8	-1.0	-0.6
31	198.4	198.2	-0.2	-0.1
33	182.0	180.6	-1.4	-0.8
35	199.4	198.2	-1.2	-0.6
37	180.9	180.8	-0.1	-0.1
39	182.1	180.8	-1.3	-0.7
41	180.5	180.9	0.4	0.2
43	163.5	164.0	0.5	0.3
45	182.0	180.9	-1.1	-0.6
47	146.5	147.6	1.1	0.7
49	147.1	147.6	0.5	0.3
51	129.5	129.9	0.4	0.3
53	115.7	115.9	0.2	0.2
55	128.8	129.9	1.1	0.8
63	43.1	42.3	-0.8	-1.9

Comment: Node 3 was deliberately adjusted more than 1 cm for esthetic reasons, to get possible imprints more continuous to the eye. Therefore, this deviation is not considered when calculating mean values. Mean deviation from prediction is 0.5 %.

The formwork is verified by comparing predicted node positions with the actual. Prestressing of the cables, element lengths and the boundary node positions is assumed to have the greatest influence on the comparison. All spring elongations where measured with an accuracy within 2 mm, which corresponds to approximately 10-30 N depending on the spring constant, which in turn was confirmed to vary. The cables are passing through either drilled holes or hooks, both inducing some amount of unaccounted friction that will influence the result. All element lengths where measured and adjusted according to the analysis. However, some node positions where adjusted by eye for esthetic reasons since accuracy of measuring element lengths with a ruler most likely deviated up to 3 mm per element. It is uncertain whether the ocular adjustment affected the result in a positive or negative way, but it certainly looked more accurate after adjustment. A laser was used to measure the actual node height. The instrument has an accuracy of 0.5 mm/m, so given the mean distance between instrument and nodes, this is believed to add ±1.5-2.0 mm error. On a final note, the boundary nodes where tuned in by using two different measurements, both space distance from a reference point, and by measuring height from the ground beam that pass through the reference point. A tape measure was used for this. The accuracy was hard to determine, but at least within 5 mm for all directions. It was also observed that some of the hooks at the longitudinal base bent due to the high prestressing force which wasn't accounted for.

Table 15. *Comparison between planning and execution with respect to time. Executed time is displayed as total man-hours.*

	Planned time [h]	Executed time [h]
Ground work	-	7.5
Foundation	-	7
Timber frame	8	14
Cable net	8	16
Membrane	4	12
Cast process	4	14+6

The work has been performed by unskilled labor (enthusiastic academics) for all parts. The group consisted of 5 workers the first day, and four the second day. 1 ½ days was added to this, with three workers on average. However, not all workers were engaged in all parts. As seen in **Table 15**, some of the parts were underestimated in comparison to the executed time. This is explained by a number of reasons. Regarding the timber frame, a lot of extra time was spent on locating and drilling node holes in the side beams. This could have been prevented by pre drilling the beams on the ground, prior to erecting the frame. Another aspect was that the erecting procedure wasn't planned in detail. Horizontal bracing was improvised empirically. This could have been avoided by including it already in analysis. However, for such a small project, this was not an overwhelming part at all, and the empirical verification still felt sufficient and convincing.

Furthermore, there was complications with the membrane. Although carefully planned, something went wrong, and the sewed fabric didn't fit the frame as intended. Extra time was spent on both manufacturing and mounting. The reason has not been determined, but it is believed that both flattening procedure and practical realization went wrong to some extent.

The final issue was during the cast process, where initial stress led to a high working pace, ultimately making parts of the applied concrete in high slopes collapse due to weight from layers added above. This was soon found to be a process where earlier applied layers needed to settle enough to carry the load from added concrete above due. There was also early issues with the mixture, in which to much filler is believed to have been added, that led to a unsuitable concrete workability for the current slope.

In summary, the execution time is believed to be heavily reduced with experience, and the planned time is still considered to be reasonable goals for each part.

4.5 Conclusion

Several observations were made during the construction process. Reflections and conclusions are made based on these observations, with some suggestions on how to improve the methodology.

4.5.1 Observations

Element lengths has to be accurately determined in the right order, and tight clamping of the nodes in an early stage aggravated adjustment of the network. If the clamps where loosely tightened they tended to slip around instead.

Longitudinal cables wants to slip towards the saddle point (reduced tension and thus minimizing energy).

The node clamp twists the connected cables somewhat, possibly affecting the forces.

It was a tedious task to readjust the element lengths with the cable locks. During prestressing, many turnbuckles hit the bottom and it was necessary to unmount and reconnect the cable with better adjusted lengths to achieve the target cable force.

The side beams should have been pre drilled while they were prefabricated on the ground. It was difficult to pin point node positions once they were in place and this might have affected the accuracy of the measurements. However, by using a reference point and both checking node distance to that point in combination with measuring height, the determined positions still felt convincing. The main loss was time.

Using continuous cables to cover several transversal lines was a bad choice. The pure friction from holes and surface of the fixed end was not sufficient. This induced a “connected” behavior for all cable pairs, making it difficult to find the target lengths, but also correct prestressing of all transversal cables. As work progressed, this approach was changed, and all ends were properly clamped to achieve individual behavior of each transversal line.

Unfortunately, the fabric had large area deviations compared to the target area. In several places, it had to be cut in place and patched to continuously cover the entire surface area. The source of error has yet to be examined, whether it was just wrongly measured and cut, or if the flattening algorithm does not work as intended. The width of the patch was not sufficient to cover the entire strip at the wide transversal side. This indicates that something happened during manufacturing, but this is not conclusive.

In the higher slopes (>45-60°), shear planes in fresh concrete were developed during the cast process. This happened over transversal cable lines, with slope changes. It is likely that the concrete was added in a too high pace, such that earlier applied concrete was not mature enough to carry load from applied layers above. This also complicated proper vibration, since the earlier layers became easily disturbed. At some places, such shear cracks are still visible in the hardened concrete surface. As a result, the final strength is expected to be lower than the calculated. The shell capacity itself is of course not part of the study, but the possible impact of the discretized slope due to the chosen cable mesh cannot be ruled out to have an effect with this concept.

Sagging influence the continuity in geometry which gives rise to possible second order load effects from bending. It was also found to increase risk of shear cracking whilst the concrete was still fresh. Parts of the applied concrete layer collapsed during the cast process on two separate occasions. The crack appeared over transversal cable crossings on both occasions. These issues is in need of further study and is a potential problem with the formwork concept. However, with increased membrane prestressing, the risk is reduced.

4.5.2 Suggested improvements

The prestressing strategy needs to be well defined. This was not sufficiently planned prior to the mounting of cables. As a result, it was necessary to go over the element lengths several times from different directions. A more practical method is retroactively proposed in steps:

1. Mount the continuous cable lengths in transversal direction, roughly measured.

2. Mount the longitudinal cables roughly measured.
3. Work from one end of the net to the other by clamping the nodes while simultaneously measuring the node distances. In transversal direction, it was usually enough to use the eye and make sure all nodes on the line could be placed within the same plane in space. This should be performed in a rather systematic manner, working with one strip of quadrilaterals at the time. With the net roughly tuned, fine tuning of element lengths can then be performed from the center strip and working systematically toward the net edges in both directions.
4. Prestress the transversal to about half the target force (in this case, those forces where about half of the longitudinal ones).
5. Prestress longitudinal cables. Geometry is a good indication early on, before it is even necessary to check forces. Continuously follow up the transversal cable forces. In longitudinal direction, tension cables pairwise to have balance and symmetry in the net geometry. It worked rather well to start with centered cable and move outwards in both directions pair wise.
6. Double check node positions and element lengths.
7. Compare and verify the geometry with the predictions from analysis. Identify deviations and possible improvements.

Some parts of the frame can be laser cut for both higher accuracy and reduced construction time. Especially the anchor beam for the longitudinal cables was tedious to cut out, with its hyperbolic curvature. With laser, it is also possible to make imprints where the node positions should be, or even precut them.

5 Discussion

This chapter concerns the formwork concept as a whole. Economic and environmental aspects are discussed, and there's also some effort to evaluate the design flow and performance of the formwork in general.

The research task has been performed with the following questions in mind:

1) Can the use of prestressed flexible formwork provide a rational building process compared to current standard methods?
2) How well can the final geometry and forces in the formwork and shell be predicted with help of the developed computational functions? How large deviations can be accepted?
3) How does the formwork influence the cost of concrete shell construction?
4) Is the formwork beneficial from an environmental perspective?
5) What are the limitations with this type of formwork method?

5.1 General performance and accuracy

The formwork concept has been shown to realize geometries that corresponds well to the predictions. With a mean deviation of just 0.5% from the predicted prestressed cable net geometry in the case study, it is natural to conclude that the computational framework is reliable in design, at least with respect to cable net design and final shell geometry. Considering the implemented flattening procedure, there is still future work left to be done since the prediction was a hit and miss. Regardless of the actual cause for failure, there is room for improvement in this area.

On a different note, the actual construction is more complex and requires a few more tools in comparison with more traditional formwork. There is also a bigger undertaking considering that the entire process consists of many smaller parts that need to be properly synchronized and managed to be a success. On the positive side, all parts of construction has been found manageable, even for labor with little training.

5.2 Cost of formwork

In total, a flexible formwork has been evaluated in section 4.3.2 to cost 2865 kr/m^2 (surface area), as an upper limit. Previous studies on the cost of traditional formwork indicate that in summary, today's cost of a traditional timber formwork would range between 400-800 Euros [7], or with an exchange rate of 10.6 (29 may, 2019) in SEK, 4240-8480 kr/m^2. This range is reported to be excluding the foundation. Given that the estimations hold, the cost reduction of using a flexible formwork will thus be 32% - 66%.

With increasingly skilled labor, the cost is expected to go down even further, and with growing project sizes, the ratio between waste and reusable material is expected to decrease. There is also a lot of money to be saved in refining the methodology such that construction time can be reduced.

5.3 Environmental aspects

It was pointed out in the introduction that concrete as a building material stands for 3% (2008) of total CO_2 emissions worldwide. For this material to remain popular and used in the future, ways to reduce environmental impact is needed. Three cornerstones are hereby identified.

1) Use of material for the same architectural program needs to be reduced somehow. One way to do this is to optimize geometry. Form that follows force are key to this, and herein lies the relevance of shell structures.
2) Waste during the construction process should be reduced. A flexible and reusable formwork fits this requirement both due to reduced amount of material needed for the formwork, but also since a larger part of the formwork can be reused. There are life cycle aspects to this that would be interesting to explore further.
3) Recycling of the material must increase. This aspect has not been covered in this thesis, but there is a belief that reused concrete could be applied also in the context of shell structures, at least for some geometries, since a well adopted geometry reduces the load effects and thus the need for high strength concrete.

The concept can also be viewed in comparison to other emerging and promising construction methods. A cable can be reused in new geometries. Laser cut polystyrene and other alternative methods are less flexible and possible to reuse in this sense, and might lead to more waste. However, a proper comparison of such methods would be in place.

5.4 The concept from a holistic perspective

A general observation that has been more or less known from the start is the complexity of this concept. The analysis can be challenging and it is imperative that the designer has good understanding and experience in the field. This goes for both the temporary formwork and the concrete shell, the permanent structure.

The construction process itself will most likely be less of an obstacle. Although there are several steps in the erection procedure that requires attention, it is still believed that construction is easily performed with little training of the workforce, given that it exists clear instructions and experienced project management. The case study was performed with untrained and inexperienced labor for all parts of the process. Nevertheless, the project outcome was satisfying and learning was quick.

The question remains if this could develop into a rational construction methodology with potential for commercial success. As for most new concepts and ideas, the short answer is that this flexible formwork concept needs time to grow and mature. There is great potential overall but more knowledge, experience and a well-established construction methodology will be a key for this to grow into common application. For some geometries in design however, this concept has little competition, and no matter how the market will look like in the future, some concrete structures will most likely be built with this, or at least similar methods.

5.5 Limitations of the concept

While the proposed formwork can realize geometries that follows the predictions well, for this concept to remain practical, anticlastic geometries are believed to be the only surface that fulfils all requirements for a properly prestressed formwork. This is of course crucial for it to be a stable shape to pour concrete on. While other shapes are possible, it would require an extension of the concept, in need of further study.

6 Conclusion

A flexible formwork concept has been explored. A computational framework has been developed for analysis of such formwork, and a case study was conducted with the intention of verifying and evaluating the concept from a holistic perspective.

It has been shown that the developed computational framework used in the analysis provides accurate predictions. There are also clear indications that this type of concept will significantly reduce cost of shell construction while at the same time reducing material waste, having positive effects on environmental impact and building economy. On the downside, the concept is complex with respect to analysis and also needs carefully planned work activities to become an attractive method compared to more traditional methods. In summary, the concept shows great potential and further studies are hereby recommended.

6.1 Future work

Over the course of this thesis work, a package with similar functionality has been developed by Dr. Tom Van Mele at Block Research Group, for their own open source framework, called COMPAS (https://compas-dev.github.io). Unfortunately, this was not known nor available during the thesis work which would perhaps otherwise have changed the chosen methodology. However, while similar, there are several functions that do not intersect. Therefore, a Python package for COMPAS with functions developed in this thesis can be created in the future, resulting in access to a larger library and possibly further improving and simplifying the analysis.

Repeated studies are necessary to verify cost of the formwork. It is also relevant to perform more tests for statistical significance in general.

7 Bibliography

[1] P. Jodidio, Shigeru Ban Complete Works 1985 - 2015, Köln: Tachen GmbH, 2015.

[2] R. Barthel, C. Brensing, E. Bubner and W. Nerdinger, Frei Otto - Lightweight Construction, Natural Design, Berlin: Birkhäuser Verlag AG, 2009.

[3] S. Samuelsson, Ingenjörens konst, Stockholm: Balkong Förlag, 2015.

[4] B. Ingels, Yes Is More, Köln: Taschen GmbH, 2009.

[5] W. Hawkins, M. Herrmann, B. Kromoser and T. Ibell, "Flexible formwork technologies: A state of the art review," *Structural Concrete,* vol. 17, no. 6, 2016.

[6] J. Orr, A. Darby, T. Ibell, M. Evernden and M. Otlet, "Concrete structures using fabric formwork," *The Structural Engineer,* vol. 89, no. 8, pp. 20-26, 2011.

[7] D. Veenendaal, "Design and form finding of flexibly formed concrete shell structures," Block Research Group, Zurich, 2017.

[8] M. Lyrenmann, "Block Research Group," 2017. [Online]. Available: http://block.arch.ethz.ch/brg/project/full-scale-construction-prototype-nest-hilo-shell-roof. [Accessed 11 May 2019].

[9] T. Van Mele, T. Mendéz Echenagucia, D. Pigram, A. Liew and P. Block, "Ultralight, flexible formwork system for thin, textile-reinforced concrete shells," *Structure,* vol. 01, no. 18, pp. 50-53, 2018.

[10] M. Bechthold, Innovative Surface Structures - Technologies and Applications, New York: Taylor & Francis, 2008.

[11] S. Adriaenssens, P. Block, D. Veenendaal and Chris Williams, Shell Structures for Architecture - Form Finding and Optimization, New York: Routledge, 2014.

[12] H. Pottmann, A. Asperl, M. Hofer and A. Kilian, Architectural Geometry, Exton: Bentley Institute Press, 2007.

[13] A. Tomas and P. Marti-Montrull, "Optimality of Candela's concrete shells: A study of his posthumous design," *Journal of the International Association for Shell and Spatial Structures,* vol. 51, no. 163, pp. 67-77, 2010.

[14] B. Hightower, "Reconsidering the hyperbolic paraboloid," 14 April 2018. [Online]. Available: https://hi.works/blog/2018/4/23/reconsidering-the-hyperbolic-paraboloid. [Accessed 7 June 2019].

[15] Y. Isono, "Structurae - International Database and Gallery of Structures," 15 June 1999. [Online]. Available: https://structurae.net/structures/norwich-sports-village-hotel/photos. [Accessed 3 June 2019].

[16] J. Chilton, "Heinz Isler's Infinite Spectrum: Form-Finding in Design," *Architectural Design,* vol. 80, no. 4, pp. 64-71, 2010.

[17] M. Rippmann, "Funicular Shell Design - Diss. ETH No. 23307," ETH Zurich, Block Research Group, Zurich, 2016.

[18] M. Popescu, M. Rippmann, T. Van Mele and P. Block, "Complex concrete casting: Knitting stay-in-place fabric formwork," in *Spatial Structures in the 21st Century*, Tokyo, 2016.

[19] D. Veenendaal, M. West and P. Block, "History and overview of fabric formwork: using fabrics for conrete casting," *Structural Concrete,* no. 12, pp. 164-177, 2011.

[20] G. Lilienthal, "Fireproof ceiling". United States of America Patent 619769, 21 February 1899.

[21] M. West, The Fabric Formwork Book, New York: Routledge, 2017.

[22] D. Veenendaal, J. Bakker and P. Block, "Structural design of the flexibly formed, mesh-reinforced concrete sandwich shell roof of NEST Hilo," *Journal of the International Association for Shell and Spatial Structures,* vol. 58, no. 16, pp. 23-38, 2017.

[23] T. Méndez Echenagucia, Interviewee, *Tour and discussion at Block Research Group.* [Interview]. 29 April 2019.

[24] Å. Samuelson, Skalhandboken - Dimensionering mot buckling, Stockholm: Mekanförbundets Förlag, 1990.

[25] P.-E. Austrell, O. Dahlblom, J. Lindemann, A. Olsson, K.-G. Olsson, K. Persson, H. Petersson, M. Ristinmaa, G. Sandberg and P.-A. Wernberg, CALFEM, A finite element toolbox, Version 3.4, Lund: KFS i Lund AB, 2004.

[26] A. Pressley, Elementary Differential Geometry, London: Springer-Verlag London Limited, 2012.

[27] D. Veenendaal and P. Block, "Design process for prototype concrete shells using a hybrid cable-net and fabric formwork," *Engineering Structures,* vol. 75, pp. 39-50, 2014.

[28] V. Kulbach, Cable structures, Design and Static Analysis, Tallinn: Estonian Academy Publishers, 2007.

[29] C. Cercadillo-Garcia and J. Fernández-Cabo, "Analytical and Numerical funicular analysis by means of the Parametric Force Density Method," *Journal of Applied Research and Technology,* vol. 14, pp. 108-124, 2016.

[30] H. Scheck, "The force density method for form finding and computation of general networks," *Computer methods in applied mechanics and engineering,* no. 3, pp. 115-134, 1974.

[31] D. Veenendaal, "An overview and comparison of structural form finding methods for general networks," *International Journal of Solids and Structures,* no. 49, pp. 3741-3753, 2012.

[32] J. Zhang and M. Ohsaki, "Adaptive force density method for form-finding problem of tensegrity structures," *International Journal of Solids and Structures,* no. 43, pp. 5658-5673, 2006.

[33] P. G. Malerba, M. Patelli and M. Quagliaroli, "An Extended Force Density Method for the form finding of cable systems with new forms," *Structural Engineering & Mechanics,* vol. 42, no. 2, pp. 191-210, 2012.

[34] P. Block, "Thrust Network Analysis, Exploring Three-dimensional Equilibrium," Massachusetts Institute of Technology, Cambridge, 2009.

[35] T. Van Mele and P. Block, "A novel form finding method for fabric formwork for concrete shells," *Journal of the International Association for Shell and Spatial Structures,* vol. 52, no. 170, 2011.

[36] F. Larsson, *Non-linear finite element analysis, a short introduction,* Gothenburg: Department of Applied Mechanics, Chalmers University of Technology, 2010.

[37] M. Géradin and D. J. Rixen, Mechanical Vibrations, Chichester: John Wiley & Sons, Ltd, 2015.

[38] R. M. Pauletti and P. M. Pimenta, "The natural force density method for the shape finding of taut structures," *Computer methods in applied mechanics and engineering,* vol. 197, pp. 4419-4428, 2008.

[39] K.-U. Bletzinger, *Form Finding and Optimization of Membranes and Minimal Surfaces,* Lyngby: Technical University of Denmark, 1998.

[40] P. Singer, *Die Berechnung von Minimalflächen, Seifenblasen, Membrane und Pneus aus geodätischer Sicht,* Stuttgart: Universität Stuttgart, 1995.

[41] B. Maurin and R. Motro, "The surface stress density method as a form-finding tool for tensile membranes," *Engineering Structures,* vol. 20, no. 8, pp. 712-719, 1998.

[42] K. Koohestani, "Nonlinear force density method for the form-finding of minimal surface membrane structures," *Communications in Nonlinear Science and Numerical Simulation,* vol. 19, pp. 2071-2087, 2014.

[43] S. Wan, "Thesis 2015-16, The Frozen Dome," 30 September 2015. [Online]. Available: http://thesis.arch.hku.hk/2015/2015/09/30/the-frozen-landmark/. [Accessed 10 June 2019].

[44] K. Linkwitz and H.-J. Schek, "Einige Bemerkungen zur Berechnung von vorgespannten Seilnetzkonstruktionen," *Ingenieur-Archiv,* vol. 40, pp. 145-158, 1971.

[45] L. Gründig, E. Moncrieff, P. Singer and D. Ströbel, "A history of the principal developments and applications of the force density method in Germany 1970-1999," in *Fourth International Colloquium on Computation of Shell & Spatial Structures*, Chania-Crete, 2000.

[46] R. M. Pauletti, "Finding Minimal and Non-Minimal Surfaces through the Natural Force Density Method," in *International Conference on Textile Composites and Inflatable Structures*, Barcelona, 2011.

[47] N. Saabye Ottosen and H. Petersson, Introduction to the finite element method, Edinburgh: Pearson Education Limited, 1992.

[48] T. Abrahamsson, "Linear System Theory in Vibration Engineering," Digital Publication, U72, ISSN 0349-8123, Gothenburg, 2000.

[49] K.-M. Koch and K. J. Habermann, Membrane Structures, London: Prestel Publishing Ltd., 2004.

[50] I. Mariolis and S. Malassiotis, "Matching Folded Garments to Unfolded Templates Using Robust Shape Analysis Techniques," in *International Conference on Computer Analysis of Images and Patterns*, Thessaloniki, 2013.

[51] S. Kolmanic and N. Guid, *The Flattening of Arbitrary Surfaces by Approximation with Developable Stripes,* Maribor: Springer, 2000.

[52] S. S. Rao, The Finite Element Method in Engineering (Fourth Edition), Miami: Elsevier Science & Technology Books, 2004.

[53] J.-L. Batoz, K.-J. Bathe and L.-W. Ho, "A study of three-node triangular plate bending elements," *International Journal for Numerical Methods in Engineering,* vol. 15, pp. 1771-1812, 1980.

[54] O. Gupta, *Note and Explanation of Formulation for DKT Shell Element and its Implementation through Open Source Finite Element Software, Elmer,* Kharagpur: Researchgate, https://www.researchgate.net/publication/276355469_Note_and_Explanation_of_Formulation_for_DKT_Shell_Element_and_its_Implementation_through_Open_Source_Finite_Element_Software_Elmer, 2015.

[55] Simulia, "Abaqus Theory Manual - 3.6.4 Triangular facet shell elements," https://classes.engineering.wustl.edu/2009/spring/mase5513/abaqus/docs/v6.6/books/stm/default.htm?startat=ch03s06ath82.html, 2019.

[56] T. Erhart, "Drilling Rotation Constraint for Shell Elements in Implicit and Explicit Analyses," Dynamore,

https://www.dynamore.de/de/download/papers/2013-ls-dyna-forum/documents/drilling-rotation-constraint-for-shell-elements-in-implicit-and-explicit-analyses, Stuttgart-Filderstadt, 2013.

[57] E. L. Neto, M. A. Ferreira Araripe, F. A. Correia Monteiro and J. A. Hernandes, "An Explicit Consistent Geometric Stiffness Matrix for the DKT Element," *Latin American Journal of Solids and Structures,* vol. 14, pp. 613-628, 2017.

[58] J. Lindemann, "Sourceforge," 05 July 2015. [Online]. Available: https://sourceforge.net/projects/calfem/. [Accessed 13 May 2019].

[59] H. Lundh, Grundläggande hållfasthetslära, Stockholm: Instant Book AB, 2013.

[60] B. Engström, "Design and analysis of slabs and flat slabs, Report 2011-5, Edition 2014," Department of Civil and Environmental Engineering, Gothenburg, 2014.

[61] Y. Xu and J. N. Karadelis, "Shear failure in plain concrete as applied to concrete pavement overlays," Department of Civil Engineering, Architecture and Building, Coventry University, Conventry, 2010.

[62] N. Williams Portal, M. Flansbjer, P. Johannesson, K. Malaga and K. Lundgren, "Tensile Behaviour of Textile Reinforcement under Accelerated Ageing Conditions," *Journal of Building Engineering,* vol. 5, pp. 57-66, 2016.

Appendix A - Empirical studies

This chapter explores practical aspects of a flexible formwork concept, with focus given to the choice of textile, determination of forces and geometry in the formwork, and a small comparison of different concrete mixtures, as preparation for the case study. An ice shell experiment has also been conducted as a first exploration of the concept of flexible formwork, which is presented and discussed below.

A.1 Fabric formwork for an ice shell

An early investigation of the concept was made by stretching a piece of cloth to adapt the well-known hypar shape. The purpose was to identify stress distribution empirically by feeling the tension in the fabric, but also to gain some practical experience in how such a setup could work when scaled up. A stay in place formwork approach was used, meaning that the cloth was sprayed with water and left in low temperature (< 0°C) to freeze, becoming an ice shell. The ice shell was then detached from the frame and subject to a snow load. The experiment has been documented with the pictures below:

A.1.1 Creating the formwork

Figure 70. *A piece of cloth is stretch to a hypar geometry by attaching it to square frame. Edges are clamped with pieces of plywood and tensioned with threads to the frame corners.*

A.1.2 Stresses and deflections

Figure 71. *The fabric is inspected by hand, adding load in different positions. There was a clear lack of stiffness in the saddle point due to an excess of fabric. Thus, the prestressing was small.*

A.1.3 Testing of ice shell capacity

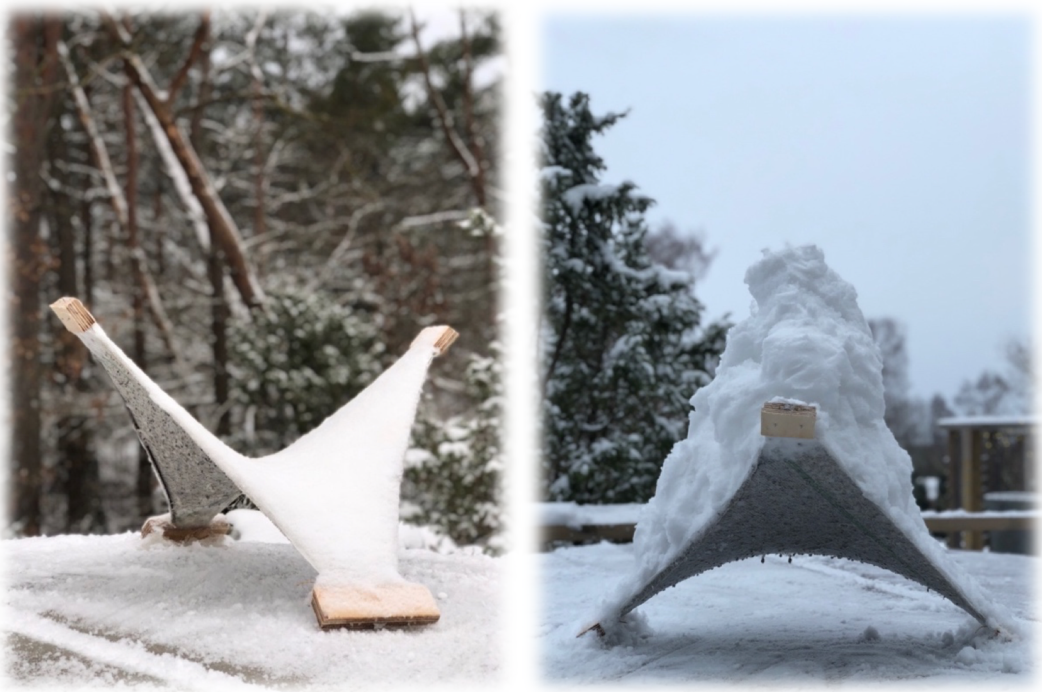

Figure 72. *When the cloth froze, the ice shell was detached from the frame and loaded with snow. Unfortunately, it was not possible to weigh the total load on this 2-4 mm thick shell of ice, but capacity was substantial.*

A.2 Evaluation of fabrics

Three different fabrics are evaluated, as shown in **Figure 73**. These three are picked out based on price, availability and recommendations in a book about fabric formwork [21]. The selection is thought to provide a variety of material characteristics such that a suitable fabric can be found through comparison of their performance in general. Two main properties are strived for, being workability in the preparation (i.e. sewing, cutting), and reaction behavior with the concrete. The sought properties are listed below:

1) Workability. Should fold easily, but not sensitive to wrinkles. It should also be flexible enough to simplify the mounting process.
2) It should be possible to sew or stitch together to achieve a continuous surface cover.
3) It should have low permeability to prevent evaporation/suction from fresh concrete, such that desired concrete quality can be guaranteed.
4) High resistance to ripping and scratching.
5) Elastic properties that balance the desired amount of sagging and possibility to stretch over the curved surface without wrinkles.

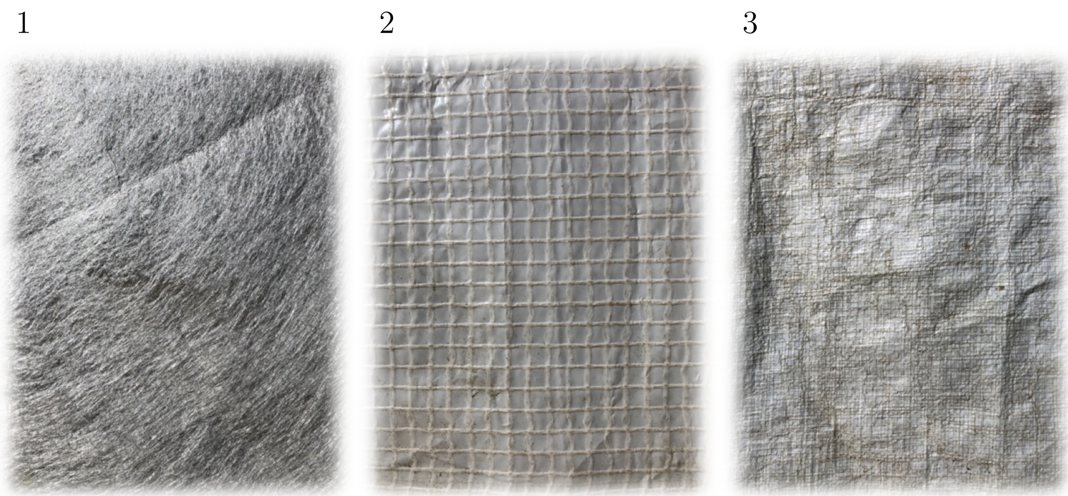

Figure 73. *The three compared fabrics have different properties and designs. Textile 1 is a standard geotextile. Textile 2 and 3 are different kinds of tarps.*

Table 16. *Comparison of material properties in three different fabrics.*

	Textile 1	**Textile 2**	**Textile 3**
Structure	Random structure of threads	More course in the structure. Has a structured 'textile reinforced' mesh, combined with a plastic ply.	Dense organized structure with thick (relative to other tested) threads.
Friction properties	Noticable	None in practice	None in practice, concrete slipped easily.
Permeability	Noticable	Water resistant, at least during the test period.	Water resistant
Absorption	Noticable water print on the fabric. Some seepage was noted.	Resistant	Resistant
Workability	Easy to stretch, easy to cut	Semi-difficult to stretch, easy to cut.	Difficult to stretch. Wrinkles easily.
Sensitivity	Does not rip easily	Insensitive	Rips easily when cut
Esthetics	Smooth surface	Coarse organized mesh pattern	Fine organized pattern

Textile 1 (standard geotextile) was evaluated with a 0-4 mm Concrete. Textile 2 and 3 was evaluated with 0-6mm aggregates for more interlocking effect.

A.3 Concreting

A test of different concrete mixtures has been performed with the purpose of finding an acceptable balance between wet concrete stability in high slopes and its workability. It should be stiff while still being able to compact properly. It was found to be quite the craftmanship to apply concrete in high slopes. Here follows some photo documentation of the process. Final mixture for the case study is presented in section 4.2.5.2. However, this empirical test was performed without fiber reinforcement, whereas the final mixture has reinforcement that ultimately changed workability favorably for high slopes.

Figure 74. *Left and right pictures show extreme mixtures; overly dry and wet, where the final mixture ended up closer to the dry example. The overly wet example have problems with separation clearly visible.*

Figure 75. *A set of pictures showing the experimental setup. This was a simultaneous test of concrete and fabric properties for a flexible formwork concept.*

Appendix B - Building documentation

To organize work in the case study, a building documentation was created as guide to the building process. The idea was to have an overview of technical data available on the building site to simplify construction.

BUILDING DOCUMENTATION

Case study 16-17 may, 2019

Flexible formwork for concrete shells

JOHAN ÖRNBORG

PRESTRESSING

NODE	FORCE [N]
1	0
2	263.0467
3	259.1235
4	262.8417
5	265.3554
6	265.2160
7	262.6385
8	257.9486
9	251.1607
10	241.8134
11	228.8178
12	210.2785
13	183.5789
14	148.2142
15	0
16	500.8158
17	451.2148
18	436.1002
19	451.2148
20	500.8158
21	0
22	148.2142
23	183.5789
24	210.2785
25	228.8178
26	241.8134
27	251.1607
28	257.9486
29	262.6385
30	265.2160
31	265.3554
32	262.8417
33	259.1235
34	263.0467
35	0
36	481.6150
37	425.7530
38	409.1338
39	425.7530
40	481.6150

PRESTRESSING MAP

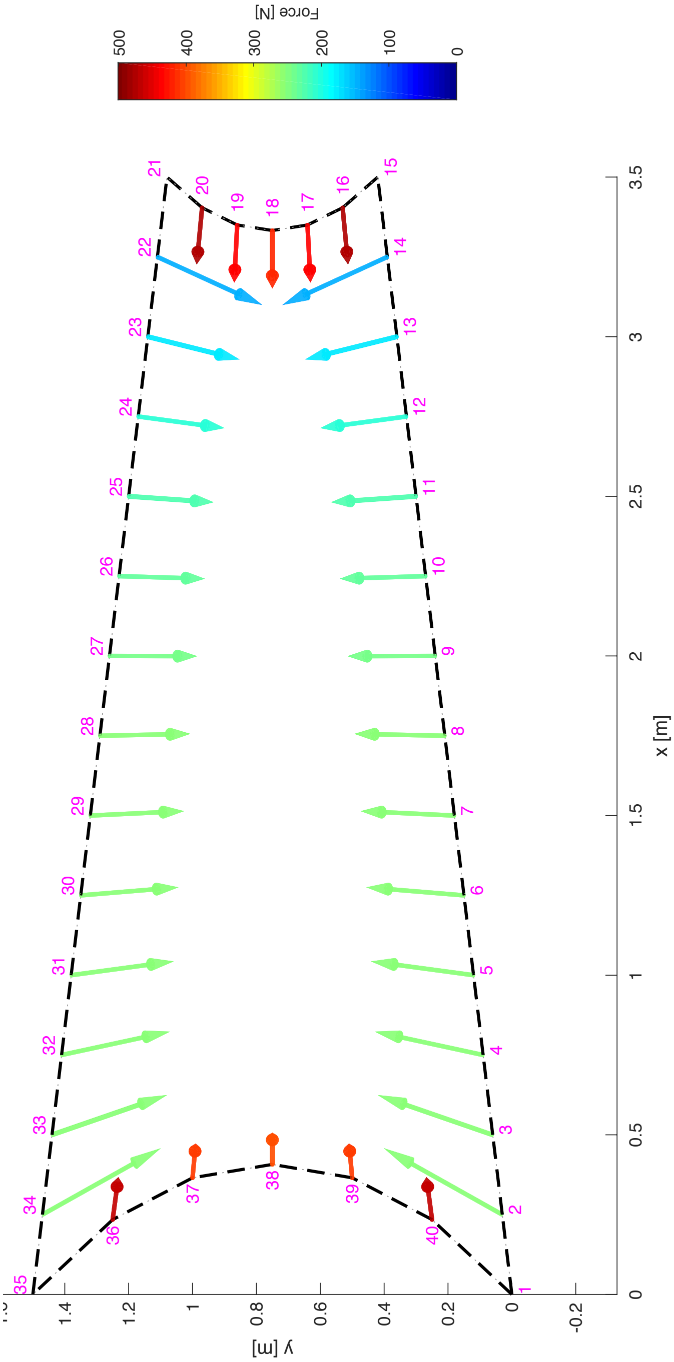

Empirical determination of spring stiffness

Spring	2 kg [mm]	12 kg [mm]	delta [mm]	k [N/mm]	Target node force [N]	Target delta [mm]	Total length [mm]
A	90,3	98,8	8,5	11,55	258	22	113
B	92,1	105,7	13,6	7,22	229	32	124
C	90	101,6	11,6	8,47			
D	91,3	100,1	8,8	11,16	500	45	136
E	90,3	98,8	8,5	11,55	262	23	113
F	91,2	103,4	12,2	8,05	451	56	147
G	91,7	100,9	9,2	10,67			
H	90,4	97,2	6,8	14,44	265	18	109
I	90	102,7	12,7	7,73	259	33	123
J	91,1	98,6	7,5	13,09	500	38	129
K	90,7	100,4	9,7	10,12	263	26	117
L	90,8	102,4	11,6	8,47	451	53	144
M	91,2	104,3	13,1	7,50	251	33	125
N	90	101,3	11,3	8,69	148	17	107
O	90,1	102,8	12,7	7,73	436	56	146
P	92,5	106,8	14,3	6,87			
Q	90,7	102,1	11,4	8,61	184	21	112
R	91,1	101,1	10	9,82	210	21	112
S	90,5	99,6	9,1	10,79	262	24	115
T	91,2	100,7	9,5	10,34	265	26	117
U	103,4	118,2	14,8	6,64	241	36	140
V	116,9	121,8	4,9	20,04			
W	90,5	99,1	8,6	11,42			
X	93,5	108,1	14,6	6,73			
Y	90,2	101,4	11,2	8,77			
Z	95	107,5	12,5	7,86			
MEAN	92,4	103,1	10,4	9,44			

PRESTRESSED FORCE DISTRIBUTION OVERVIEW

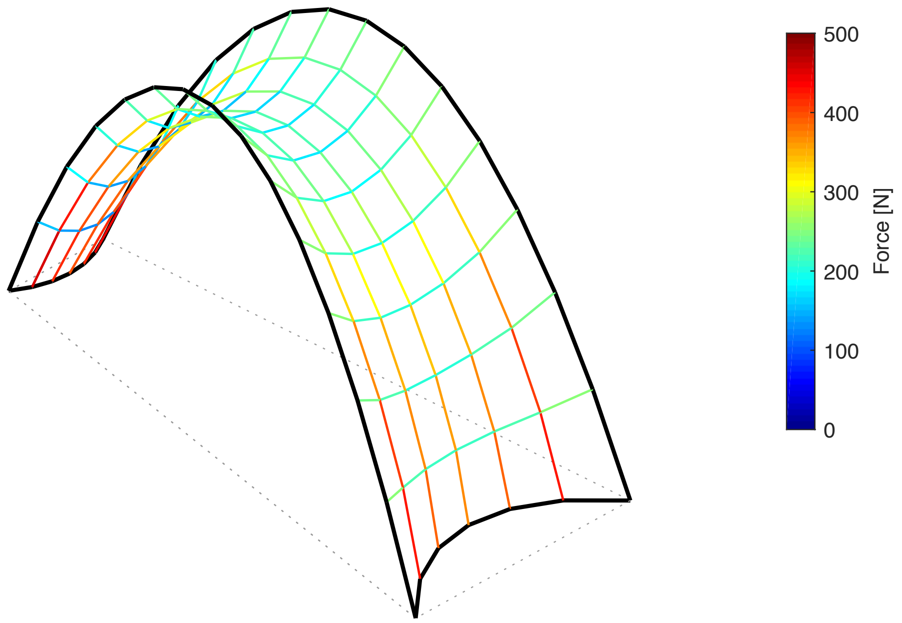

LOADED NET FORCE DISTRIBUTION OVERVIEW

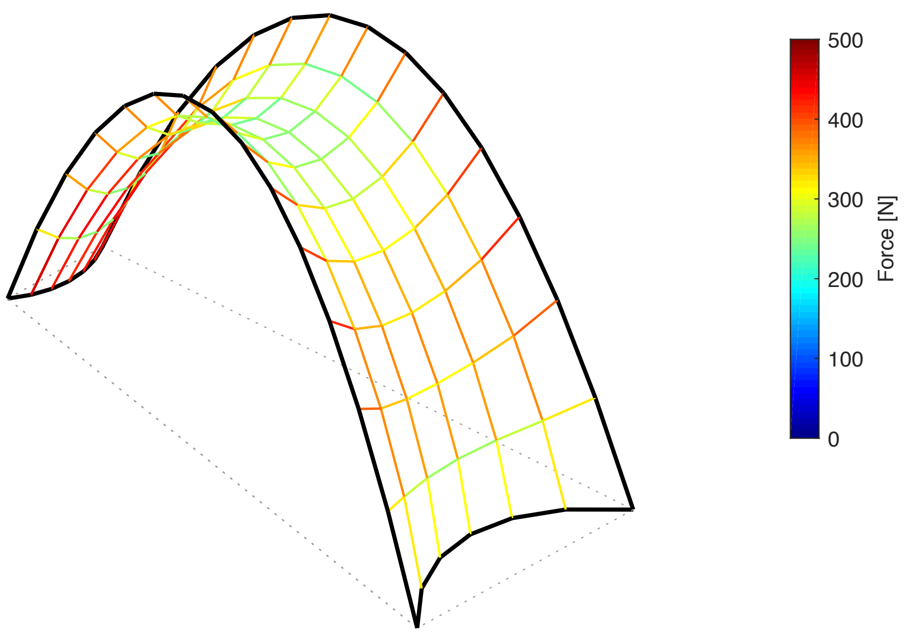

NODE COORDINATE MAP

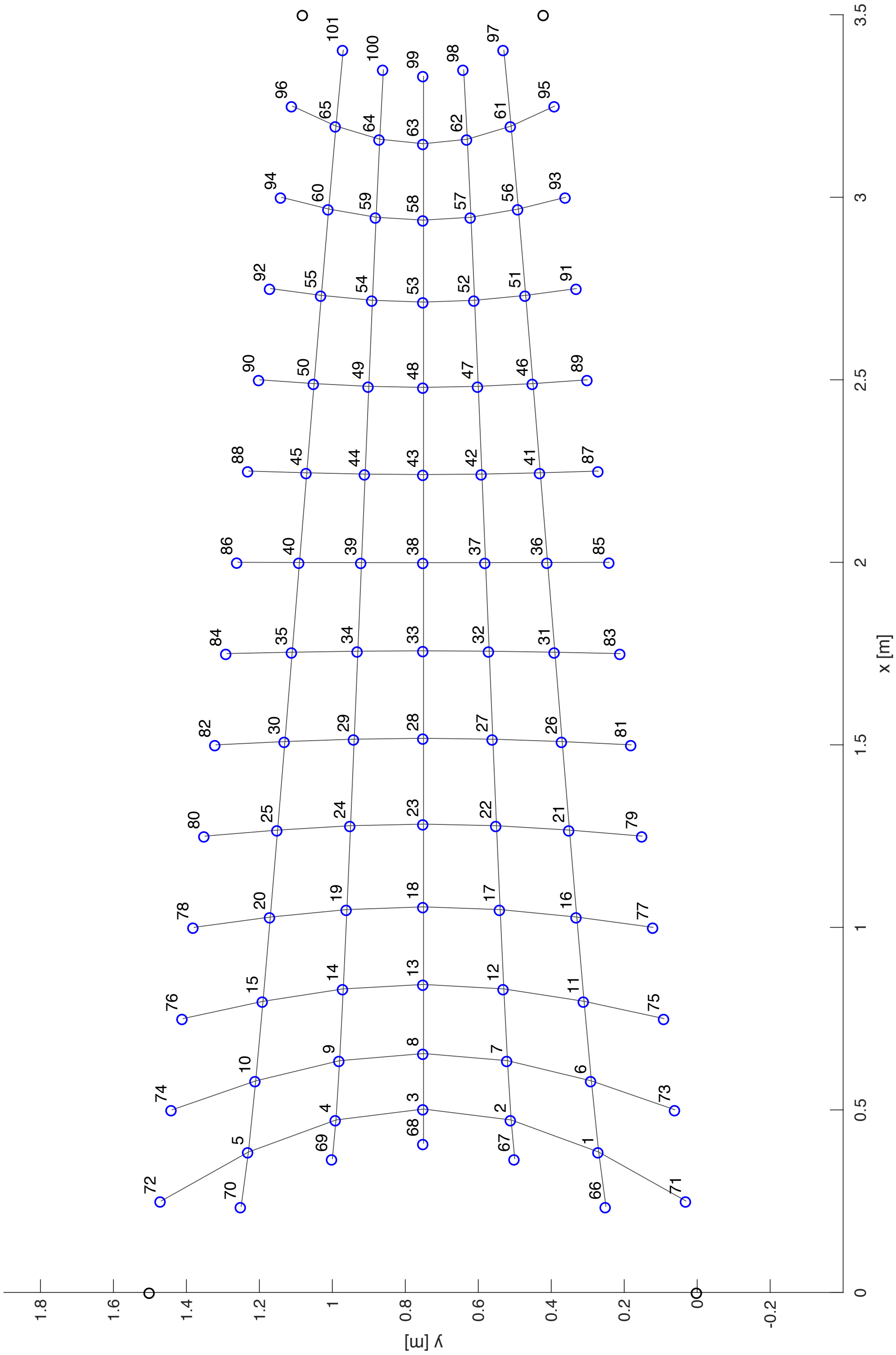

NODE COORDINATE LIST - PRESTRESSED STATE

Node	x [m]	y [m]	z [m]
1	0.3847	0.2700	0.4866
2	0.4725	0.5100	0.4375
3	0.5024	0.7500	0.4224
4	0.4725	0.9900	0.4375
5	0.3847	1.2300	0.4866
6	0.5796	0.2900	0.9262
7	0.6349	0.5200	0.8425
8	0.6545	0.7500	0.8160
9	0.6349	0.9800	0.8425
10	0.5796	1.2100	0.9262
11	0.7975	0.3100	1.2989
12	0.8315	0.5300	1.1933
13	0.8437	0.7500	1.1591
14	0.8315	0.9700	1.1933
15	0.7975	1.1900	1.2989
16	1.0283	0.3300	1.5950
17	1.0488	0.5400	1.4759
18	1.0562	0.7500	1.4370
19	1.0488	0.9600	1.4759
20	1.0283	1.1700	1.5950
21	1.2665	0.3500	1.8092
22	1.2785	0.5500	1.6824
23	1.2829	0.7500	1.6406
24	1.2785	0.9500	1.6824
25	1.2665	1.1500	1.8092
26	1.5090	0.3700	1.9387
27	1.5156	0.5600	1.8079
28	1.5180	0.7500	1.7646
29	1.5156	0.9400	1.8079
30	1.5090	1.1300	1.9387
31	1.7538	0.3900	1.9820
32	1.7565	0.5700	1.8499
33	1.7576	0.7500	1.8062
34	1.7565	0.9300	1.8499
35	1.7538	1.1100	1.9820
36	1.9995	0.4100	1.9387
37	1.9992	0.5800	1.8079
38	1.9991	0.7500	1.7646
39	1.9992	0.9200	1.8079
40	1.9995	1.0900	1.9387
41	2.2452	0.4300	1.8092
42	2.2417	0.5900	1.6824
43	2.2404	0.7500	1.6406
44	2.2417	0.9100	1.6824
45	2.2452	1.0700	1.8092
46	2.4896	0.4500	1.5950
47	2.4820	0.6000	1.4759
48	2.4792	0.7500	1.4370
49	2.4820	0.9000	1.4759
50	2.4896	1.0500	1.5950
51	2.7312	0.4700	1.2989
52	2.7177	0.6100	1.1933
53	2.7129	0.7500	1.1591
54	2.7177	0.8900	1.1933
55	2.7312	1.0300	1.2989
56	2.9677	0.4900	0.9262
57	2.9452	0.6200	0.8425
58	2.9373	0.7500	0.8160
59	2.9452	0.8800	0.8425
60	2.9677	1.0100	0.9262
61	3.1949	0.5100	0.4866
62	3.1589	0.6300	0.4375
63	3.1466	0.7500	0.4224
64	3.1589	0.8700	0.4375
65	3.1949	0.9900	0.4866
66	0.2344	0.2500	0
67	0.3653	0.5000	0
68	0.4073	0.7500	0
69	0.3653	1.0000	0
70	0.2344	1.2500	0
71	0.2500	0.0300	0.5850
72	0.2500	1.4700	0.5850
73	0.5000	0.0600	1.0800
74	0.5000	1.4400	1.0800
75	0.7500	0.0900	1.4850
76	0.7500	1.4100	1.4850
77	1.0000	0.1200	1.8000
78	1.0000	1.3800	1.8000
79	1.2500	0.1500	2.0250
80	1.2500	1.3500	2.0250
81	1.5000	0.1800	2.1600
82	1.5000	1.3200	2.1600
83	1.7500	0.2100	2.2050
84	1.7500	1.2900	2.2050
85	2.0000	0.2400	2.1600
86	2.0000	1.2600	2.1600
87	2.2500	0.2700	2.0250
88	2.2500	1.2300	2.0250
89	2.5000	0.3000	1.8000
90	2.5000	1.2000	1.8000
91	2.7500	0.3300	1.4850
92	2.7500	1.1700	1.4850
93	3.0000	0.3600	1.0800
94	3.0000	1.1400	1.0800
95	3.2500	0.3900	0.5850
96	3.2500	1.1100	0.5850
97	3.4040	0.5300	0
98	3.3500	0.6400	0
99	3.3326	0.7500	0
100	3.3500	0.8600	0
101	3.4040	0.9700	0

CABLE LENGTHS – ELEMENT INDEX

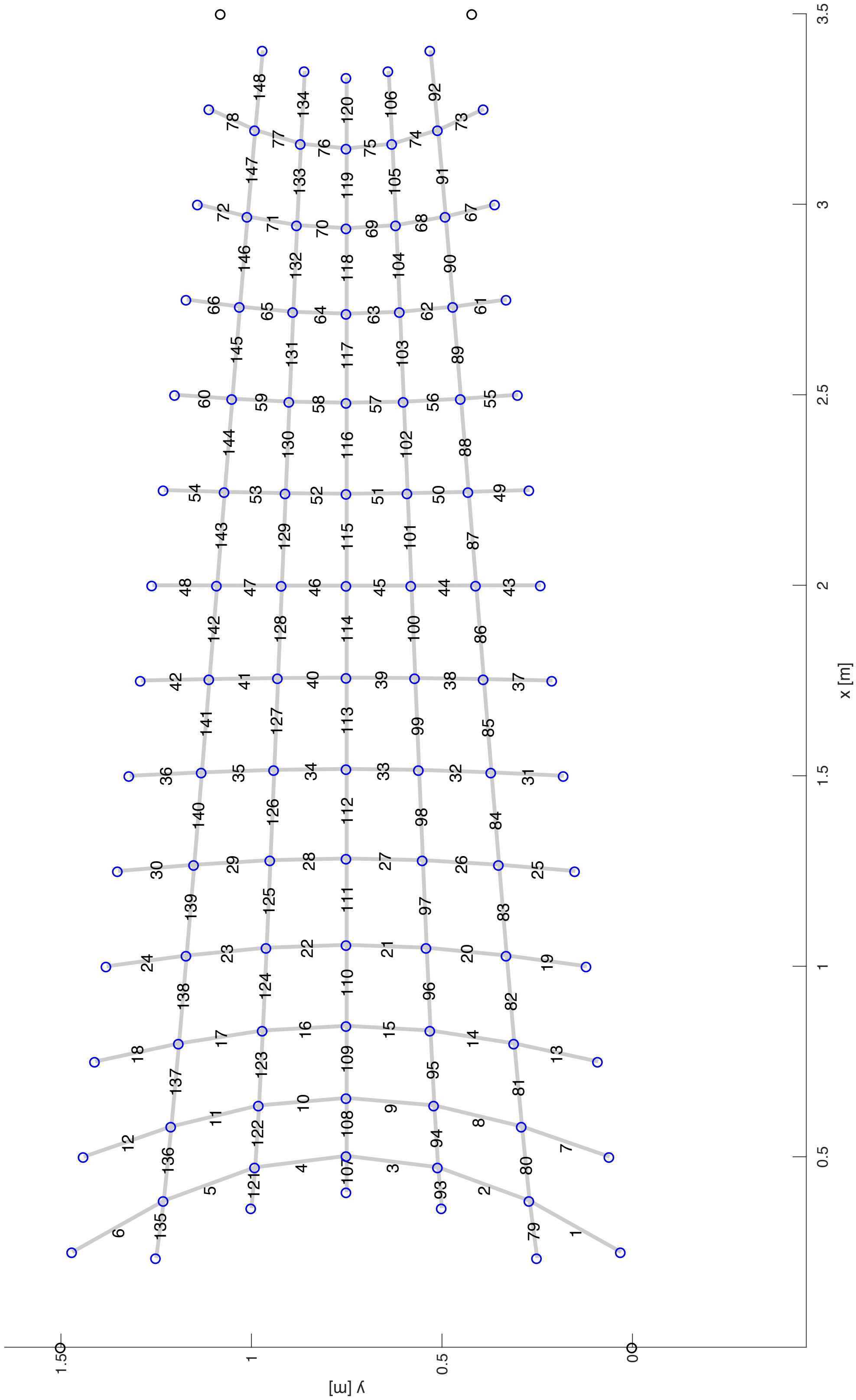

ELEMENT LENGTHS [m]

Node	l
1	0.2923
2	0.2602
3	0.2423
4	0.2423
5	0.2602
6	0.2923
7	0.2879
8	0.2509
9	0.2323
10	0.2323
11	0.2509
12	0.2879
13	0.2920
14	0.2464
15	0.2230
16	0.2230
17	0.2464
18	0.2920
19	0.2948
20	0.2423
21	0.2137
22	0.2137
23	0.2423
24	0.2948
25	0.2947
26	0.2371
27	0.2044
28	0.2044
29	0.2371
30	0.2947
31	0.2918
32	0.2308
33	0.1949
34	0.1949
35	0.2308
36	0.2918
37	0.2866
38	0.2233
39	0.1852
40	0.1852
41	0.2233
42	0.2866
43	0.2791
44	0.2145
45	0.1754
46	0.1754
47	0.2145
48	0.2791
49	0.2687
50	0.2042
51	0.1654
52	0.1654
53	0.2042
54	0.2687
55	0.2542
56	0.1916
57	0.1550
58	0.1550
59	0.1916
60	0.2542
61	0.2336
62	0.1759
63	0.1442
64	0.1442
65	0.1759
66	0.2336
67	0.2040
68	0.1562
69	0.1329
70	0.1329
71	0.1562
72	0.2040
73	0.1647
74	0.1346
75	0.1216
76	0.1216
77	0.1346
78	0.1647
79	0.5096
80	0.4813
81	0.4322
82	0.3759
83	0.3210
84	0.2756
85	0.2494
86	0.2503
87	0.2784
88	0.3256
89	0.3827
90	0.4419
91	0.4952
92	0.5300
93	0.4505
94	0.4365
95	0.4022
96	0.3567
97	0.3090
98	0.2684
99	0.2448
100	0.2465
101	0.2732
102	0.3170
103	0.3682
104	0.4182
105	0.4581
106	0.4775
107	0.4329
108	0.4220
109	0.3918
110	0.3498
111	0.3047
112	0.2657
113	0.2432
114	0.2451
115	0.2713
116	0.3139
117	0.3631
118	0.4099
119	0.4458
120	0.4615
121	0.4505
122	0.4365
123	0.4022
124	0.3567
125	0.3090
126	0.2684
127	0.2448
128	0.2465
129	0.2732
130	0.3170
131	0.3682
132	0.4182
133	0.4581
134	0.4775
135	0.5096
136	0.4813
137	0.4322
138	0.3759
139	0.3210
140	0.2756
141	0.2494
142	0.2503
143	0.2784
144	0.3256
145	0.3827
146	0.4419
147	0.4952
148	0.5300

CABLE LENGTHS – PRESTRESSED STATE [m]

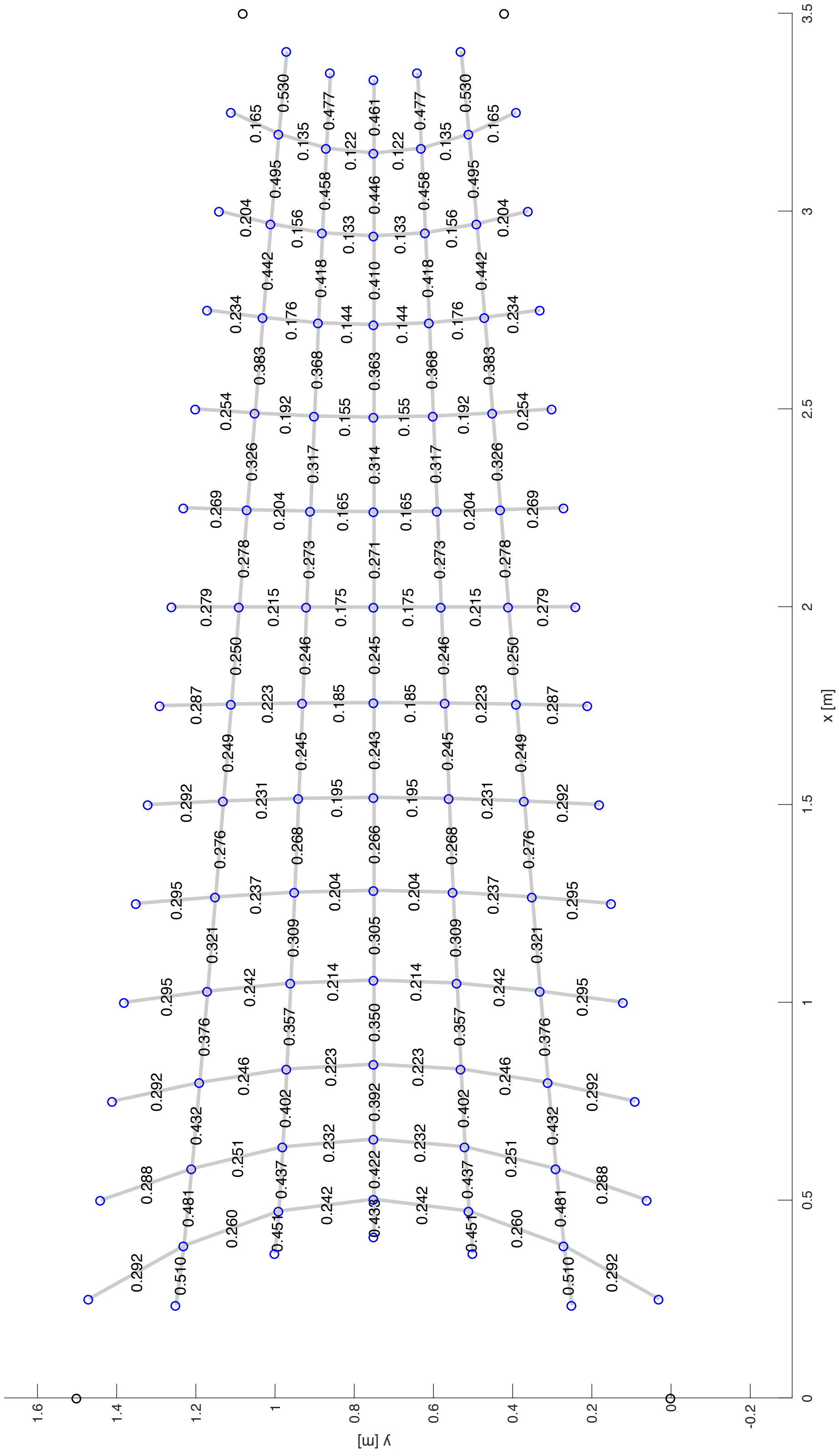

MEMBRANE PATTERNING AND FLATTENING

Patch1

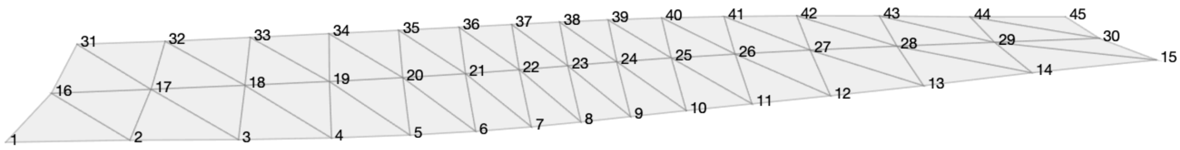

	Patch1	
Node	**x**	**y**
1	0	0
2	0.6362	0.0106
3	1.1907	0.0133
4	1.6667	0.0218
5	2.0688	0.0365
6	2.4052	0.0558
7	2.6893	0.0783
8	2.9433	0.1034
9	3.1973	0.1309
10	3.4814	0.1614
11	3.8178	0.1960
12	4.2199	0.2371
13	4.6959	0.2886
14	5.2504	0.3548
15	5.8866	0.4200
16	0.2344	0.2500
17	0.7436	0.2700
18	1.2245	0.2900
19	1.6563	0.3100
20	2.0317	0.3300
21	2.3520	0.3500
22	2.6269	0.3700
23	2.8755	0.3900
24	3.1251	0.4100
25	3.4027	0.4300
26	3.7277	0.4500
27	4.1099	0.4700
28	4.5513	0.4900
29	5.0462	0.5100
30	5.5758	0.5300
31	0.3653	0.5000
32	0.8157	0.5150
33	1.2521	0.5347
34	1.6541	0.5540
35	2.0107	0.5714
36	2.3196	0.5868
37	2.5878	0.6007
38	2.8324	0.6132
39	3.0787	0.6245
40	3.3517	0.6342
41	3.6685	0.6415
42	4.0366	0.6454
43	4.4546	0.6446
44	4.9126	0.6397
45	5.3900	0.6400

MEMBRANE PATTERNING AND FLATTENING

Patch2

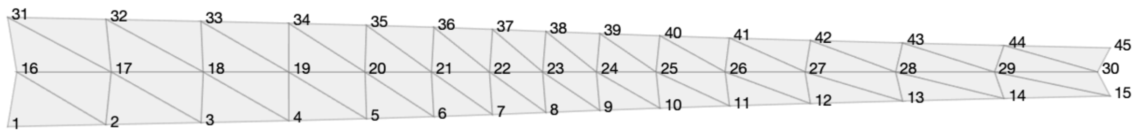

	Patch2	
Node	**x**	**y**
1	0.3653	0
2	0.8157	0.0095
3	1.2521	0.0185
4	1.6541	0.0274
5	2.0107	0.0364
6	2.3196	0.0457
7	2.5878	0.0551
8	2.8324	0.0648
9	3.0787	0.0746
10	3.3517	0.0846
11	3.6685	0.0950
12	4.0366	0.1059
13	4.4546	0.1173
14	4.9126	0.1291
15	5.3900	0.1400
16	0.4073	0.2500
17	0.8403	0.2500
18	1.2622	0.2500
19	1.6540	0.2500
20	2.0039	0.2500
21	2.3086	0.2500
22	2.5743	0.2500
23	2.8175	0.2500
24	3.0626	0.2500
25	3.3339	0.2500
26	3.6478	0.2500
27	4.0109	0.2500
28	4.4208	0.2500
29	4.8666	0.2500
30	5.3281	0.2500
31	0.3653	0.5000
32	0.8157	0.4905
33	1.2521	0.4815
34	1.6541	0.4726
35	2.0107	0.4636
36	2.3196	0.4543
37	2.5878	0.4449
38	2.8324	0.4352
39	3.0787	0.4254
40	3.3517	0.4154
41	3.6685	0.4050
42	4.0366	0.3941
43	4.4546	0.3827
44	4.9126	0.3709
45	5.3900	0.3600

MEMBRANE PATTERNING AND FLATTENING

Patch3

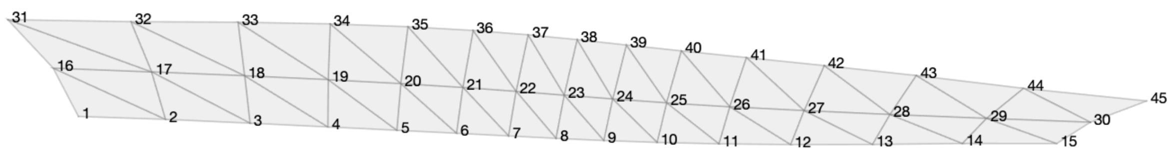

	Patch3	
Node	**x**	**y**
1	0.3653	0.1454
2	0.8157	0.1304
3	1.2521	0.1107
4	1.6541	0.0913
5	2.0107	0.0740
6	2.3196	0.0586
7	2.5878	0.0447
8	2.8324	0.0321
9	3.0787	0.0209
10	3.3517	0.0112
11	3.6685	0.0039
12	4.0366	0
13	4.4546	0.0008
14	4.9126	0.0057
15	5.3900	0.0054
16	0.2344	0.3954
17	0.7436	0.3754
18	1.2245	0.3554
19	1.6563	0.3354
20	2.0317	0.3154
21	2.3520	0.2954
22	2.6269	0.2754
23	2.8755	0.2554
24	3.1251	0.2354
25	3.4027	0.2154
26	3.7277	0.1954
27	4.1099	0.1754
28	4.5513	0.1554
29	5.0462	0.1354
30	5.5758	0.1154
31	0	0.6454
32	0.6362	0.6348
33	1.1907	0.6321
34	1.6667	0.6235
35	2.0688	0.6089
36	2.4052	0.5896
37	2.6893	0.5671
38	2.9433	0.5420
39	3.1973	0.5145
40	3.4814	0.4840
41	3.8178	0.4494
42	4.2199	0.4083
43	4.6959	0.3568
44	5.2504	0.2906
45	5.8866	0.2254

PERIMETER SYSTEM

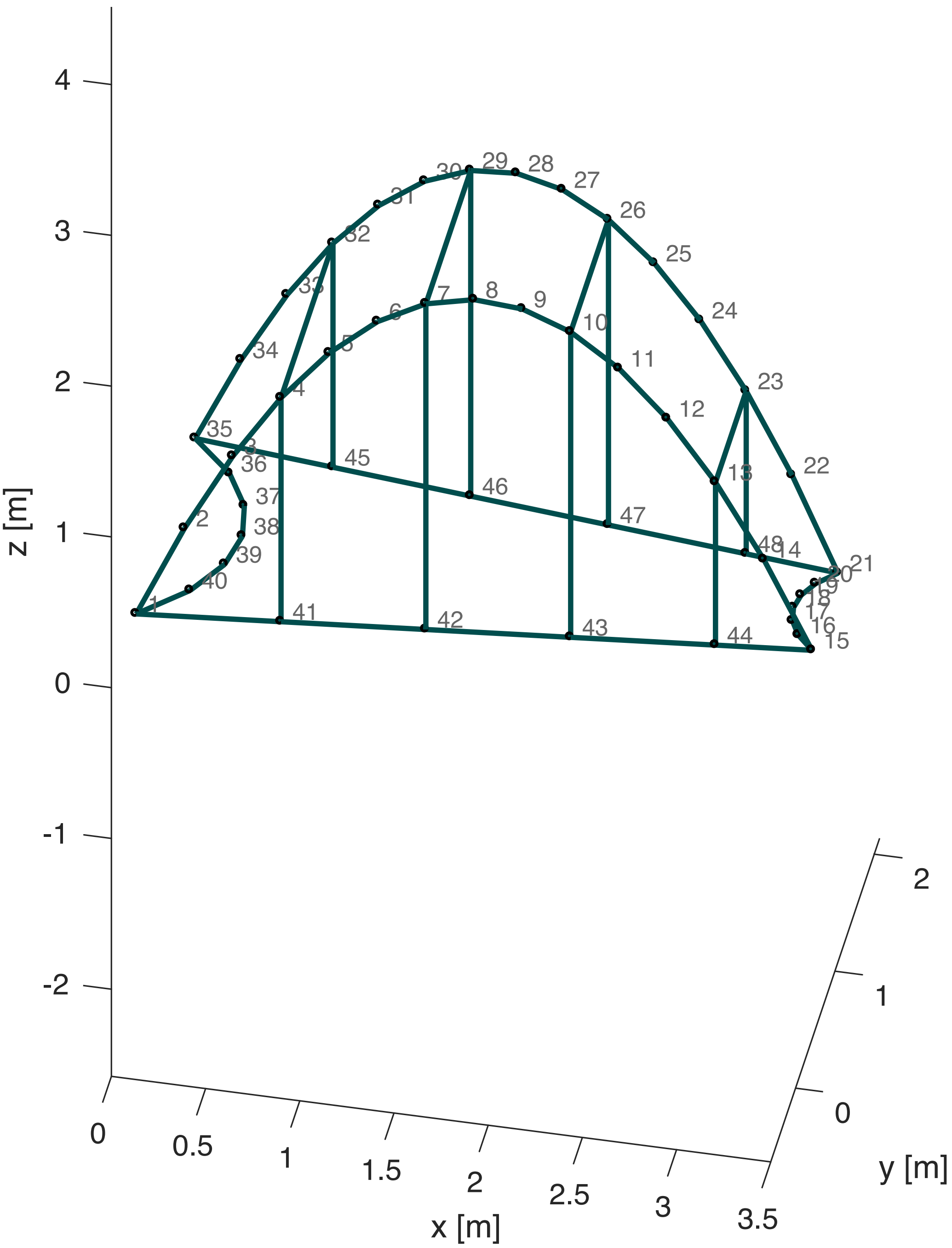

PERIMETER SYSTEM COORDINATES

	Perimeter		
Node	**x**	**y**	**z**
1	0	0	0
2	0.2500	0.0300	0.5850
3	0.5000	0.0600	1.0800
4	0.7500	0.0900	1.4850
5	1.0000	0.1200	1.8000
6	1.2500	0.1500	2.0250
7	1.5000	0.1800	2.1600
8	1.7500	0.2100	2.2050
9	2.0000	0.2400	2.1600
10	2.2500	0.2700	2.0250
11	2.5000	0.3000	1.8000
12	2.7500	0.3300	1.4850
13	3.0000	0.3600	1.0800
14	3.2500	0.3900	0.5850
15	3.5000	0.4200	0
16	3.4040	0.5300	0
17	3.3500	0.6400	0
18	3.3326	0.7500	0
19	3.3500	0.8600	0
20	3.4040	0.9700	0
21	3.5000	1.0800	0
22	3.2500	1.1100	0.5850
23	3.0000	1.1400	1.0800
24	2.7500	1.1700	1.4850
25	2.5000	1.2000	1.8000
26	2.2500	1.2300	2.0250
27	2.0000	1.2600	2.1600
28	1.7500	1.2900	2.2050
29	1.5000	1.3200	2.1600
30	1.2500	1.3500	2.0250
31	1.0000	1.3800	1.8000
32	0.7500	1.4100	1.4850
33	0.5000	1.4400	1.0800
34	0.2500	1.4700	0.5850
35	0	1.5000	0
36	0.2344	1.2500	0
37	0.3653	1.0000	0
38	0.4073	0.7500	0
39	0.3653	0.5000	0
40	0.2344	0.2500	0
41	0.7500	0.0900	0
42	1.5000	0.1800	0
43	2.2500	0.2700	0
44	3.0000	0.3600	0
45	0.7500	1.4100	0
46	1.5000	1.3200	0
47	2.2500	1.2300	0
48	3.0000	1.1400	0

Dimensions

Curved side beam:	45x120 mm
Struts and additional:	45x90 mm